CrossMark

An Embedded X-Ray Source Shines through the Aspherical AT 2018cow: Revealing the Inner Workings of the Most Luminous Fast-evolving Optical Transients

R. Margutti[1], B. D. Metzger[2], R. Chornock[3], I. Vurm[4], N. Roth[5,6], B. W. Grefenstette[7], V. Savchenko[8], R. Cartier[9], J. F. Steiner[10,33], G. Terreran[1], B. Margalit[11], G. Migliori[12,13], D. Milisavljevic[14], K. D. Alexander[1,33], M. Bietenholz[15,16], P. K. Blanchard[17], E. Bozzo[8], D. Brethauer[1], I. V. Chilingarian[17,18], D. L. Coppejans[1], L. Ducci[8,19], C. Ferrigno[8], W. Fong[1], D. Götz[20], C. Guidorzi[21], A. Hajela[1], K. Hurley[22], E. Kuulkers[23], P. Laurent[20], S. Mereghetti[24], M. Nicholl[17,25], D. Patnaude[17], P. Ubertini[26], J. Banovetz[15], N. Bartel[16], E. Berger[17], E. R. Coughlin[2,33], T. Eftekhari[17], D. D. Frederiks[27], A. V. Kozlova[27], T. Laskar[28,29], D. S. Svinkin[29], M. R. Drout[30,31], A. MacFadyen[32], and K. Paterson[1]

[1] Center for Interdisciplinary Exploration and Research in Astrophysics (CIERA) and Department of Physics and Astronomy, Northwestern University, Evanston, IL 60208, USA
[2] Department of Physics and Columbia Astrophysics Laboratory, Columbia University, New York, NY 10027, USA
[3] Astrophysical Institute, Department of Physics and Astronomy, 251B Clippinger Lab, Ohio University, Athens, OH 45701, USA
[4] Tartu Observatory, University of Tartu, Tõravere 61602, Tartumaa, Estonia
[5] Department of Astronomy, University of Maryland, College Park, MD 20742, USA
[6] Joint Space-Science Institute, University of Maryland, College Park, MD 20742, USA
[7] Cahill Center for Astrophysics, 1216 E. California Boulevard, California Institute of Technology, Pasadena, CA 91125, USA
[8] ISDC, Department of Astronomy, University of Geneva, Chemin d'Écogia, 16 CH-1290 Versoix, Switzerland
[9] Cerro Tololo Inter-American Observatory, National Optical Astronomy Observatory, Casilla 603, La Serena, Chile
[10] MIT Kavli Institute for Astrophysics and Space Research, Massachusetts Institute of Technology, 70 Vassar Street, Cambridge, MA 02139, USA
[11] Department of Astronomy, University of California, Berkeley, CA 94720, USA
[12] Dipartimento di Fisica e Astronomia, Alma Mater Studiorum, Università degli Studi di Bologna, Via Gobetti 93/2, I-40129 Bologna, Italy
[13] INAF Istituto di Radioastronomia, via Gobetti 101, I-40129 Bologna, Italy
[14] Department of Physics and Astronomy, Purdue University, 525 Northwester Avenue, West Lafayette, IN 47907, USA
[15] Hartebeesthoek Radio Observatory, P.O. Box 443, Krugersdorp, 1740, South Africa
[16] Department of Physics and Astronomy, York University, Toronto, M3J 1P3, Ontario, Canada
[17] Harvard-Smithsonian Center for Astrophysics, 60 Garden St., Cambridge MA 02138, USA
[18] Sternberg Astronomical Institute, M.V. Lomonosov Moscow State University, Universitetsky prospect 13, Moscow, 119234, Russia
[19] Institut für Astronomie und Astrophysik, Kepler Center for Astro and Particle Physics, Eberhard Karls Universitat, Sand 1, D-72076, Tubingen, Germany
[20] CEA Saclay - Irfu/D'epartement d'Astrophysique, Orme des Merisiers, Bat. 709, F-91191 Gif-sur-Yvette, France
[21] Department of Physics and Earth Science, University of Ferrara, via Saragat 1, I-44122, Ferrara, Italy
[22] University of California at Berkeley, Space Sciences Laboratory, 7 Gauss Way, Berkeley, CA 94720, USA
[23] ESA/ESTEC, Keplerlaan 1, Noordwijk, The Netherlands
[24] INAF - Istituto di Astrofisica Spaziale e Fisica Cosmica Milano, Via E. Bassini 15, I-20133 Milano, Italy
[25] Institute for Astronomy, University of Edinburgh, Royal Observatory, Blackford Hill, Edinburgh EH9 3HJ, UK
[26] Istituto di Astrofisica e Planetologia Spaziali, INAF Via Fosso del Cavaliere 100, I-00133 Rome, Italy
[27] Ioffe Physical-Technical Institute, Politekhnicheskaya 26, St. Petersburg 194021, Russia
[28] National Radio Astronomy Observatory, 520 Edgemont Road, Charlottesville, VA 22903, USA
[29] Department of Astronomy, University of California, 501 Campbell Hall, Berkeley, CA 94720-3411, USA
[30] The Observatories of the Carnegie Institution for Science, 813 Santa Barbara St., Pasadena, CA 91101, USA
[31] Department of Astronomy and Astrophysics, University of Toronto, 50 St. George Street, Toronto, Ontario, M5S 3H4 Canada
[32] Center for Cosmology and Particle Physics, New York University, 726 Broadway, New York, NY 10003, USA

Abstract

We present the first extensive radio to γ-ray observations of a fast-rising blue optical transient, AT 2018cow, over its first $\sim$100 days. AT 2018cow rose over a few days to a peak luminosity $L_{pk} \sim 4 \times 10^{44}$ erg s^{-1}, exceeding that of superluminous supernovae (SNe), before declining as $L \propto t^{-2}$. Initial spectra at $\delta t \lesssim 15$ days were mostly featureless and indicated large expansion velocities $v \sim 0.1c$ and temperatures reaching $T \sim 3 \times 10^4$ K. Later spectra revealed a persistent optically thick photosphere and the emergence of H and He emission features with $v \sim 4000$ km s^{-1} with no evidence for ejecta cooling. Our broadband monitoring revealed a hard X-ray spectral component at $E \geqslant 10$ keV, in addition to luminous and highly variable soft X-rays, with properties unprecedented among astronomical transients. An abrupt change in the X-ray decay rate and variability appears to accompany the change in optical spectral properties. AT 2018cow showed bright radio emission consistent with the interaction of a blast wave with $v_{sh} \sim 0.1c$ with a dense environment ($\dot{M} \sim 10^{-3} - 10^{-4} M_\odot$ yr^{-1} for $v_w = 1000$ km s^{-1}). While these properties exclude ^{56}Ni-powered transients, our multiwavelength analysis instead indicates that AT 2018cow harbored a "central engine," either a compact object (magnetar or black hole) or an embedded internal shock produced by interaction with a compact, dense circumstellar medium. The engine released $\sim 10^{50}$–$10^{51.5}$ erg over $\sim 10^3$–10^5 s and resides within low-mass fast-moving material with equatorial–polar density asymmetry ($M_{ej,fast} \lesssim 0.3 M_\odot$). Successful SNe from low-mass H-rich stars (like electron-capture SNe) or failed explosions from blue supergiants satisfy these constraints. Intermediate-mass black holes are disfavored by the large environmental density probed by the radio observations.

Key words: accretion, accretion disks – stars: black holes – supernovae: individual (AT 2018cow) – X-rays: general

---

[33] Einstein Fellow.

1. Introduction

Recent high-cadence surveys have uncovered a plethora of rapidly evolving transients with diverse observed properties that challenge our current notions of stellar death (e.g., Drout et al. 2014; Arcavi et al. 2016; Tanaka et al. 2016; Pursiainen et al. 2018 for recent sample compilations). Such rapid evolution is generally attributed to a small mass of ejecta $M \lesssim 1 M_{\odot}$. However, the wide range of observed properties (i.e., luminosities, energetics, chemical composition, and environments) reveals them to be an extremely heterogeneous class and likely reflects a diverse range of intrinsic origins.

Fast-evolving transients can be either rich or poor in hydrogen and span a wide range of peak luminosities. Some are less luminous than normal H-stripped core-collapse supernovae (i.e., SNe Ibc; e.g., SN 2005E, Perets et al. 2010; SN 2008 ha, Foley et al. 2009; Valenti et al. 2009) or populate the low end of the luminosity function of SNe Ibc (e.g., SNe 2005ek, 2010X; Kasliwal et al. 2010; Drout et al. 2013). The relatively old stellar environments of some of these transients and their low luminosities have inspired connections with models of He-shell detonations on white dwarf (WD) progenitors (".Ia" SNe; Shen et al. 2010). However, the oxygen-dominated ejecta of SN 2005ek and the young stellar environments of other rapidly evolving transients are instead more readily explained as either explosions of massive stars that have been efficiently stripped of their envelopes by binary interaction (Drout et al. 2013; Tauris et al. 2013, 2015; Kleiser & Kasen 2014; Suwa et al. 2015; Moriya et al. 2017) or as "cooling envelope" emission from the explosion of radially extended red supergiant stars (Tanaka et al. 2016).

Some rapidly evolving transients can compete in luminosity with SNe Ibc (e.g., SN 2002bj ; Poznanski et al. 2010) or even outshine normal core-collapse SNe (Arcavi et al. 2016; Whitesides et al. 2017). The short timescales, high peak luminosities, and lack of UV line blanketing observed in many of these transients are in tension with traditional SN models powered by the radioactive decay of ^{56}Ni (e.g., Poznanski et al. 2010; Drout et al. 2014; Pursiainen et al. 2018; Rest et al. 2018). These objects typically show blue colors and have been referred to in the literature as "fast-evolving luminous transients" (Rest et al. 2018) or "Fast Blue Optical Transients" (FBOTs; Drout et al. 2014). Here we adopt the "FBOT" acronym.

The non-radioactive sources of energy needed to explain FBOTs fall into two broad categories: (i) interaction of the explosion's shock wave with a dense circumstellar environment or extended progenitor atmosphere (Balberg & Loeb 2011; Chevalier & Irwin 2011; Ginzburg & Balberg 2014). This class of models has been applied to a variety of FBOTs with and without direct evidence for interaction in their spectra (e.g., Ofek et al. 2010; Drout et al. 2014; Pastorello et al. 2015; Shivvers et al. 2016; Rest et al. 2018). In this scenario, the high luminosities of FBOTs are the result of efficient conversion of ejecta kinetic energy into radiation, as the explosion shock interacts with a dense external shell, while the rapid timescale is attributed to the relatively compact radius of the shell. (ii) Models involving prolonged energy injection from a central compact object, such as a magnetar with a millisecond rotation period (Yu et al. 2013; Metzger & Piro 2014; Hotokezaka et al. 2017), an accreting neutron star (NS; e.g., following a WD–NS merger; Margalit & Metzger 2016), or an accreting stellar-mass (Kashiyama & Quataert 2015) or supermassive black hole (BH; e.g., Strubbe & Quataert 2009; Cenko et al. 2012a).

Until recently, progress in understanding the intrinsic nature of FBOTs was hampered by their low discovery rate and typically large distances ($d \geqslant 500$ Mpc), which limited opportunities for spectroscopic and multiwavelength follow-up observations. Here we present extensive radio-to-γ-ray observations of the astronomical transient AT 2018cow over its first ~100 days of evolution. AT 2018cow was discovered on 2018 June 16 by the ATLAS survey as a rapidly evolving transient located within a spiral arm of the dwarf star-forming galaxy CGCG 137-068 at 60 Mpc (Prentice et al. 2018; Smartt et al. 2018). Prentice et al. (2018), Perley et al. (2019), Rivera Sandoval et al. (2018), and Kuin et al. (2019) presented the UV/optical/NIR and soft X-ray properties of AT 2018cow (as detected by *Swift*) in the first ~50 days since discovery. We present our UV/optical/NIR photometry and spectroscopy in Sections 2.1 and 2.2. Broadband soft-to-hard X-ray data from coordinated follow-up with *INTEGRAL*, *NuSTAR*, *Swift*-XRT, and *XMM-Newton* are presented and analyzed in Sections 2.3, 2.4, and 2.5, while our radio observations with VLA and VLBA are described in Section 2.6. We present the search for prompt γ-ray emission from AT 2018cow with the Inter-Planetary Network in Section 2.7. In Section 3, we derive multiband inferences of the physical properties of AT 2018cow, and we discuss the intrinsic nature of AT 2018cow in Section 4. We conclude in Section 5.

Uncertainties are provided at the 1σ confidence level (c.l.), and we list 3σ c.l. upper limits unless explicitly stated otherwise. Throughout the paper, we refer times to the time of optical discovery, which is 2018 June 16 10:35:02 UTC, corresponding to MJD 58285.44 (Smartt et al. 2018; Prentice et al. 2018). AT 2018cow is located in the host galaxy CGCG 137-068 ($z = 0.0141$), and we adopt a distance of 60 Mpc as in Smartt et al. (2018), Prentice et al. (2018), and Perley et al. (2019). We assume $h = 0.7$, $\Omega_M = 0.3$, and $\Omega_\Lambda = 0.7$.

2. Observations and Data Analysis

2.1. UV–Optical–NIR Photometry

The UV Optical Telescope (UVOT; Roming et al. 2005) on board the *Neil Gehrels Swift Observatory* (Gehrels et al. 2004) started observing AT 2018cow on 2018 June 19 (~3 days since discovery) with six filters, v, b, u, $w1$, $w2$, and $m2$, in the wavelength range $\lambda_c = 1928$ Å ($w2$ filter)—$\lambda_c = 5468$ Å (v filter, central wavelength). We extracted aperture photometry following standard prescriptions by Brown et al. (2009), with the updated calibration files and revised zero points by Breeveld et al. (2011). Each individual frame has been visually inspected and quality flagged. Observations with insufficient exposure time have been merged to obtain higher signal-to-noise ratio images from which we extracted the final photometry. We used a $3''$ source region of extraction to minimize the effects of the contamination from the underlying host-galaxy flux, and we manually corrected for imperfections of the astrometric solution of the automatic UVOT pipeline realigning the frames. In the absence of template images, we estimated the host-galaxy contribution by measuring the host-galaxy emission at a similar distance from the nucleus. The results from our method are in excellent agreement with Perley et al. (2019). We note that at $\delta t > 50$ days, this method is likely to overestimate the UV flux of the transient, as the images show the presence of a bright knot of UV emission underlying AT 2018cow that can only be properly accounted for with template images obtained in the future.

Ground-based optical photometry has been obtained from ANDICAM, mounted on the 1.3 m telescope[34] at Cerro Tololo Inter-American Observatory (CTIO), the Low Resolution Imaging Spectrometer (LRIS; Oke et al. 1995), and the DEep Imaging Multi-Object Spectrograph (DEIMOS; Faber et al. 2003), mounted on the Keck telescopes. Images from the latter were reduced following standard bias and flat-field corrections. Data from ANDICAM, instead, came already reduced by their custom pipeline.[35] Instrumental magnitudes were extracted using the point-spread-function (PSF) fitting technique, performed using the SNOOPY[36] package. Absolute calibrations were achieved measuring zero points and color terms for each night, estimated using as reference the magnitudes of field stars, retrieved from the Sloan Digital Sky Survey[37] (SDSS; York et al. 2000) catalog (DR9). SDSS magnitudes of the field stars were then converted to Johnson/Cousins, following Chonis & Gaskell (2008). Our *BVRI* PSF photometry agrees well with the host-galaxy-subtracted photometry presented by Perley et al. (2019).

We obtained near-IR imaging observations in the *JHK* bands with the Wide-field Camera (WFCAM; Casali et al. 2007) mounted on the 3.8 m United Kingdom Infrared Telescope (UKIRT) spanning $\delta t \sim 10$–42 days. We obtained preprocessed images from the WFCAM Science Archive (Hamly et al. 2008), which are corrected for bias, flat-field, and dark current by the Cambridge Astronomical Survey Unit.[38] For each epoch and filter, we co-add the images and perform astrometry relative to 2MASS using a combination of tasks in Starlink[39] and IRAF. For the *J*-band, we obtain a template image from the UKIRT Hemispheres Survey DR1 (Dye et al. 2018) and use the HOTPANTS software package (Becker 2015) to perform image subtraction against this template to produce residual images. We perform aperture photometry using standard tasks in IRAF, photometrically calibrated to 2MASS. In the absence of a template image in the *H*- and *K*-bands, we performed aperture photometry of the transient and host-galaxy complex centered on the core of the host galaxy. We used standard procedures in IRAF and 2.5 FWHM apertures. At $\delta t < 15$ days, the host-galaxy contribution is negligible but dominates the *HK* photometry at $\delta t > 30$ days. Single epochs of *JHK*-band photometry were obtained on 2018 June 26 ($\delta t \sim 9.86$ days) using the WIYN High-resolution Infrared Camera (WHIRC; Meixner et al. 2010) mounted on the 3.5 m WIYN telescope, and on 2018 August 31 ($\delta t \sim 75.7$ days) with the MMT and Magellan Infrared Spectrograph (MMIRS; McLeod et al. 2012), mounted on the MMT telescope. These data were processed using similar methods. AT 2018cow is not detected against the host-galaxy NIR background in our final observation. After subtracting the bright sky contribution, we estimated the instrumental NIR magnitudes via PSF fitting. We calibrate our NIR photometry relative to 2MASS[40] (Skrutskie et al. 2006). No color term correction was applied to the NIR data.

UV, optical, and NIR photometry have been corrected for Galactic extinction with $E(B - V) = 0.07$ mag (Schlafly & Finkbeiner 2011) and no extinction in the host galaxy. Our final

photometry is presented in Tables 9–12. The UV/optical/NIR emission from AT 2018cow is shown in Figure 1.

2.2. Optical and NIR Spectroscopy

We obtained five spectra of AT 2018cow using the Goodman spectrograph (Clemens et al. 2004) mounted on the SOAR telescope in the time range $\delta t \sim 4.6$–34.2 days. We used the red camera and the 400 lines mm^{-1} and 600 lines mm^{-1} gratings, providing a resolution of ~ 5 Å and ~ 3 Å at 7000 Å, respectively. We reduced Goodman data following the usual steps, including bias subtraction, flat-fielding, cosmic-ray rejection (see van Dokkum 2001), wavelength calibration, flux calibration, and telluric correction using our own custom IRAF[41] routines.

On 2018 July 9 ($\delta t \sim 21.4$ days), we acquired a spectrum with the Low Dispersion Survey Spectrograph (LDSS3) mounted on the 6.5 m Magellan Clay telescope using the VPH-all grism and a 1″ slit. We obtained a spectrum with the Inamori-Magellan Areal Camera and Spectrograph (IMACS) mounted on the 6.5 m Magellan Baade telescope on 2018 August 6 ($\delta t \sim 51$ days), using the f/4 camera and 300 lines mm^{-1} grating with a 0″.9 slit. The data were reduced using standard procedures in IRAF and PyRAF to bias-correct, flat-field, and extract the spectrum. Wavelength calibration was achieved using HeNeAr comparison lamps, and relative flux calibration was applied using a standard star observed with the same setup.

We observed AT 2018cow on 2018 August 29 ($\delta t \sim 74$ days) with DEIMOS. We used a 0″.7 slit and the 600 lines mm^{-1} grating with the GG400 filter, resulting in a ~ 3 Å resolution over the range 4500–8500 Å. We acquired a spectrum with LRIS on 2018 September 9 ($\delta t \sim 85.8$ days). We used the 1″.0 slit with the 400 lines mm^{-1} grating, achieving a resolution of ~ 6 Å and spectral coverage of 3200–9000 Å. Due to readout issues, we lost a portion of the spectrum between 5800 and 6150 Å. Reduction of these spectra was done using standard IRAF routines for bias subtraction and flat-fielding. Wavelength and flux calibration were performed comparing the data to arc lamps and standard stars, respectively, acquired during the night and using the same setups. A final epoch of *BVRI* photometry was acquired with LRIS on 2018 October 5 ($\delta t \sim 112$ days).

We acquired one epoch of low-resolution NIR spectroscopy spanning 0.98–2.31 μm with the MMT using MMIRS on 2018 July 3 ($\delta t \sim 16.6$ days). Observations were performed using a 1″ slit width in two configurations: *zJ* filter (0.95–1.50 μm) + *J* grism ($R \sim 2000$), and *HK3* filter (1.35–2.3 μm) + *HK* grism ($R \sim 1400$). For each of the configurations, the total exposure time was 1800 s, and the slit was dithered between individual 300 s exposures. We used the standard MMIRS pipeline (Chilingarian et al. 2015) to process the data and to develop wavelength-calibrated 2D frames from which 1D extractions were made.

Figures 2–3 show our spectral series. These figures show the drastic evolution of AT 2018cow from an almost featureless spectrum around the optical peak with very broad features, to the clear emergence of H and He emission with asymmetric line profiles skewed to the red and significantly smaller velocities of a few 1000 km s^{-1}. In Table 3, we summarize our NIR/optical spectroscopic observations.

---

[34] Operated by the SMARTS Consortium.
[35] https://github.com/SMARTSconsortium/ANDICAM
[36] http://sngroup.oapd.inaf.it/snoopy.html
[37] http://www.sdss.org
[38] http://casu.ast.cam.ac.uk/
[39] http://starlink.eao.hawaii.edu/starlink
[40] http://www.ipac.caltech.edu/2mass/

---

[41] IRAF is distributed by the National Optical Astronomy Observatories, which are operated by the Association of Universities for Research in Astronomy, Inc., under cooperative agreement with the National Science Foundation.
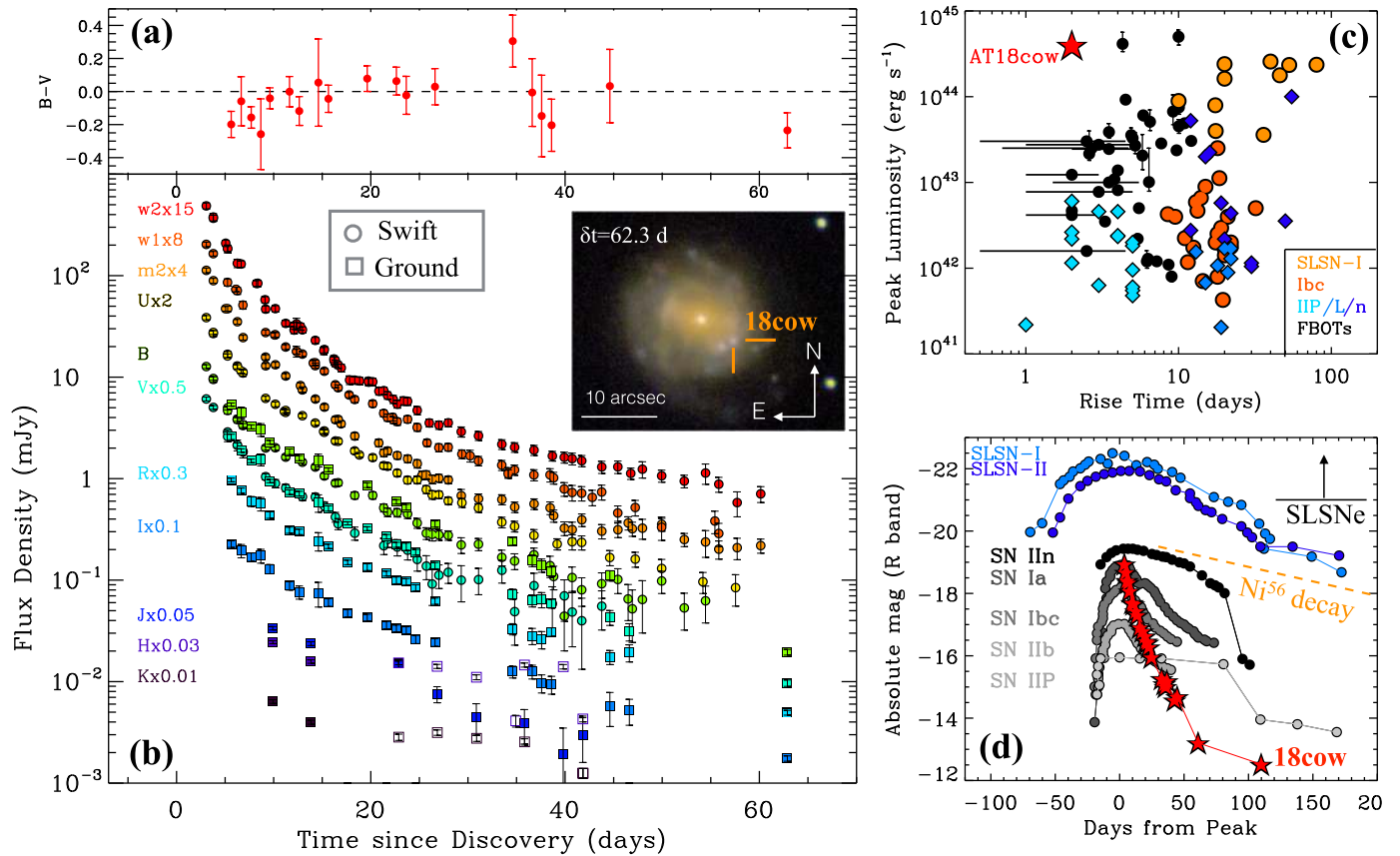
Figure 1. Panel (a): AT 2018cow maintains observed blue colors $(B − V) < 0$ until late times, while the UV/optical/NIR flux rapidly decays. Panel (b): filled circles: extinction-corrected, host-galaxy subtracted flux densities derived from *Swift*-UVOT observations. Filled squares: extinction-corrected flux densities derived from our CTIO photometry (*BVRI* at $\delta t < 50$ days), Keck photometry (*BVRI* at $\delta t > 50$ days), and UKIRT and WIYN photometry (*JHK*). For the NIR bands, empty symbols mark the times when significant contamination from the host-galaxy emission is present. Inset: RGB false-color image of AT 2018cow and its host galaxy obtained on 2018 August 17 with DEIMOS mounted on Keck II. The position of AT 2018cow is clearly off-center. Panels (c)–(d): optical light-curve properties of AT 2018cow in the context of other stellar explosions and FBOTs from the literature. AT 2018cow shows an extremely rapid rise time of a few days (as constrained by Perley et al. 2019; Prentice et al. 2018), and a decay significantly faster than ^{56}Ni-powered decays (orange dashed line in panel (d)). AT 2018cow rivals in luminosity the most luminous normal SNe in the *R*-band (panel (d)), but it is more luminous at peak than some SLSNe when its bolometric output is considered (panel (c); Section 2.8) due to its remarkably blue colors. Following Gal-Yam (2012), we show in panel (d) prototypical events for each class: PTF 09cnd (SLSN-I; Quimby et al. 2011); SN 2006gy (SLSN-II); the "Nugent template" for normal type Ia SNe, SN 2005cl (SN IIn; Kiewe et al. 2012); the average type Ibc light curve from Drout et al. (2011), SN 2011dh (SN IIb; Arcavi et al. 2011; Soderberg et al. 2012); and the prototypical type II-P SN 1999em (Leonard et al. 2002). Other references: Hamuy (2003), Campana et al. (2006), Taubenberger et al. (2006), Valenti et al. (2008), Botticella et al. (2009), Cobb et al. (2010), Kasliwal et al. (2010), Ofek et al. (2010), Poznanski et al. (2010), Andrews et al. (2011), Chomiuk et al. (2011), Arcavi et al. (2012), Bersten et al. (2012), Valenti et al. (2012), Drout et al. (2013), Inserra et al. (2013), Lunnan et al. (2013), Drout et al. (2014), Margutti et al. (2014), Vinkó et al. (2015), Nicholl et al. (2016), Arcavi et al. (2016), Whitesides et al. (2017), Pursiainen et al. (2018).

2.3. *Soft X-Rays:* Swift-*XRT and* XMM-Newton

The X-Ray Telescope (XRT) on board the *Neil Gehrels Swift Observatory* (Gehrels et al. 2004; Burrows et al. 2005) started observing AT 2018cow on 2018 June 19 (~3 days following discovery). We reduced the *Swift*-XRT data with HEASoft v.6.24 and corresponding calibration files, applying standard data filtering as in Margutti et al. (2013a). A bright X-ray source is detected at the location of the optical transient, with clear evidence for persistent X-ray flaring activity on timescales of a few days (Section 2.9), superimposed on an overall fading of the emission (Figure 4).

A time-resolved spectral analysis reveals limited spectral evolution. Fitting the 0.3–10 keV data with an absorbed power-law model within XSPEC, we find that the XRT spectra are well described by a photon index $\Gamma \sim 1.5$ and no evidence for intrinsic neutral hydrogen absorption (Figure 4, upper panel). We employ Cash statistics and derive the parameter uncertainties from a series of MCMC simulations. We adopt a Galactic neutral hydrogen column density in the direction of AT 2018cow, $N_{\rm H,MW} = 0.05 \times 10^{22}$ cm^{-2} (Kalberla et al. 2005). With a different method based on X-ray afterglows of GRBs, Willingale et al. (2013) estimated $N_{\rm H,MW} = 0.07 \times 10^{22}$ cm^{-2}. In particular, the earliest XRT spectrum extracted between 3 and 5 days since discovery can be fitted with $\Gamma = 1.55 \pm 0.05$ and can be used to put stringent constraints on the amount of neutral material in front of the emitting region, which is $N_{\rm H,int} < 6 \times 10^{20}$ cm^{-2} (we adopt solar abundances from Asplund et al. 2009 within XSPEC). The material is thus either fully ionized or absent (Section 3.3.2). The results from the time-resolved *Swift*-XRT analysis are reported in Table 4. The total XRT spectrum collecting data in the time interval 3–60 days can be fitted with an absorbed power law with $\Gamma = 1.55 \pm 0.04$ and $N_{\rm H,int} < 0.03 \times 10^{22}$ cm^{-2}. From this spectrum, we infer a 0.3–10 keV count-to-flux conversion factor of 4.3×10^{-11} erg cm^{-2} ct^{-1} (absorbed), 4.6×10^{-11} erg cm^{-2} ct^{-1} (unabsorbed), which we use to flux-calibrate the XRT light curve (Figure 4). At the distance of ~60 Mpc, the
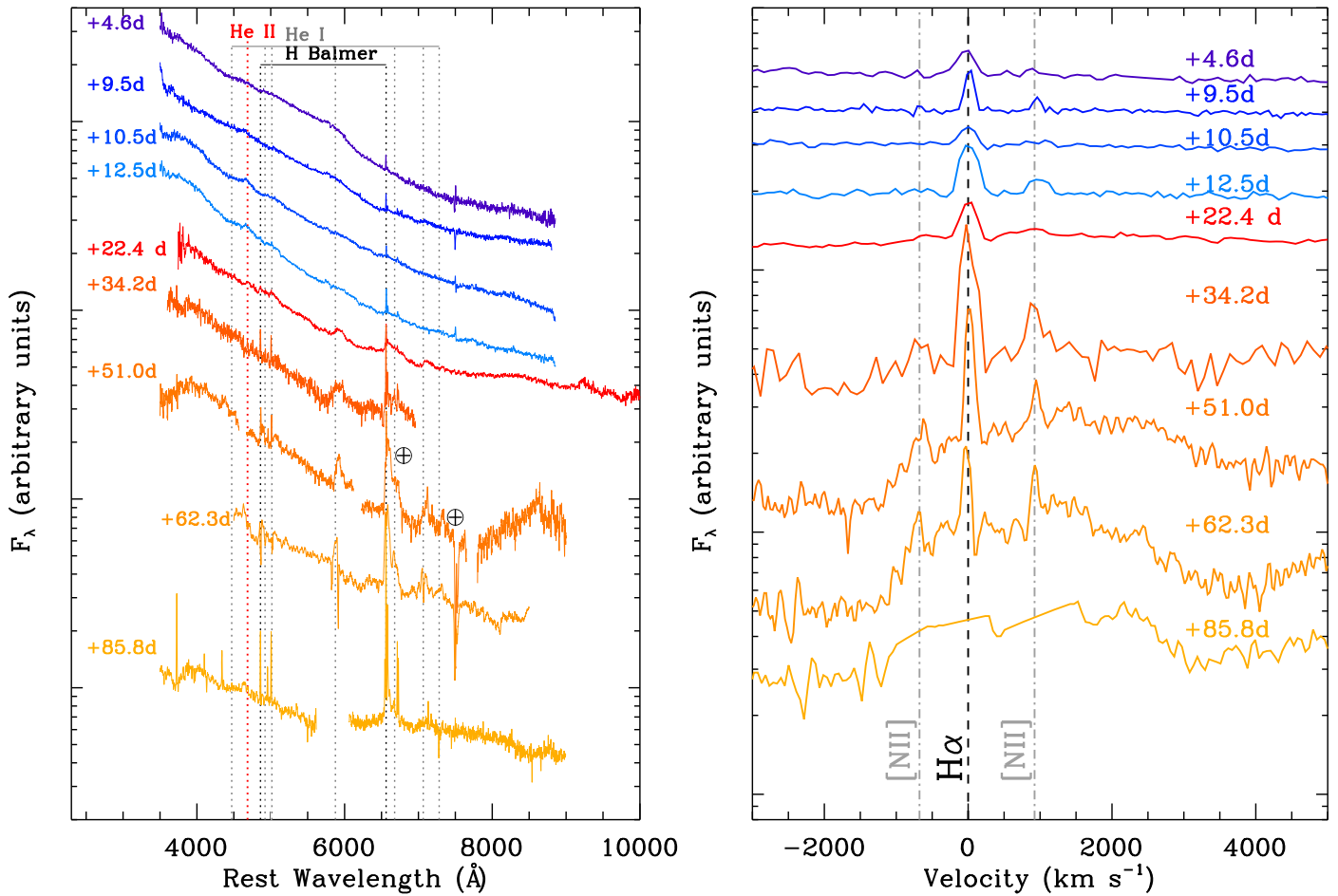
Figure 2. Optical spectral evolution of AT 2018cow (left panel), with a zoom-in to the Hα region of the spectrum in velocity space (right panel). At $\delta t \lesssim 20$ days, the spectrum exhibits only extremely broad features with $v \sim 0.1c$, in addition to narrow emission lines from the host galaxy. At $\delta t > 20$ days, He I and H features start to develop with velocities of a few 1000 km s^{-1} and a redshifted line profile. In the Hα panel on the right, we clipped the strong narrow-line emission from the host galaxy in our latest spectrum at $\delta t = 85.8$ days for display purposes.

inferred 0.3–10 keV isotropic X-ray luminosity at 3 days is $L_X \sim 10^{43}$ erg s^{-1}. AT 2018cow is significantly more luminous than normal SNe and shows a luminosity similar to that of low-luminosity GRBs (Figure 5). The spectrum also shows evidence for positive residuals above $\sim$8 keV, which are connected to the hard X-ray component of emission revealed by *NuSTAR* and *INTEGRAL* (Section 2.4).

We triggered deep *XMM-Newton* observations of AT 2018cow on 2018 July 23 ($\delta t \sim 36.5$ days, exposure time $\sim$32 ks, imaging mode; PI Margutti), in coordination with our *NuSTAR* monitoring. We reduced and analyzed the data of the European Photon Imaging Camera (EPIC)-pn data using standard routines in the Scientific Analysis System (SAS version 17.0.0) and the relative calibration files, and used MOS1 data as a validation check. After filtering data for high background contamination, the net exposure times are 24.0 and 31.5 ks for pn and MOS1, respectively. An X-ray source is clearly detected at the position of the optical transient. We extracted a spectrum from a circular region of 30″ radius centered at the source position. Pile-up effects are negligible as we verified with the task epatplot. The background was extracted from a source-free region on the same chip. We estimate a 0.3–10 keV net count rate of 0.519 ± 0.005 c/s. The X-ray data were grouped to a minimum of 15 counts per bin. The 0.3–10 keV spectrum is well fitted by an absorbed

power-law model with best-fitting $\Gamma = 1.70 \pm 0.02$ and marginal evidence for $N_{\mathrm{H,int}} \sim 0.02 \times 10^{22}$ cm^{-2} at the 3σ c. l. for $N_{\mathrm{H,MW}} = 0.05 \times 10^{22}$ cm^{-2}. Given that the uncertainty on $N_{\mathrm{H,MW}}$ is also $\sim$0.02 $\times$ 10^{22} cm^{-2}, we consider this value as an upper limit on $N_{\mathrm{H,int}}$ at 36.5 days.

We acquired a second epoch of deep X-ray observations with *XMM-Newton* on 2018 September 6 ($\delta t \sim 82$ days; PI Margutti). The net exposure times are 30.5 and 36.8 ks for pn and MOS1, respectively. AT 2018cow is clearly detected with a net 0.3–10 keV count rate of (6.0 ± 0.7) × 10^{-3} c s^{-1}. We used a source region of 20″ to avoid contamination by a faint unrelated source located 36″.8 southwest from our target (at earlier times, AT 2018cow is significantly brighter and the contamination is negligible). The spectrum of AT 2018cow is well fitted by a power-law model with $\Gamma = 1.62 \pm 0.20$ with unabsorbed 0.3–10 keV flux $\sim$2 × 10^{-14} erg cm^{-2} s^{-1}. We find no evidence for intrinsic neutral hydrogen absorption. Finally, we note that comparing the two *XMM-Newton* observations, we find no evidence for a shift of the X-ray centroid, from which we conclude that X-ray emission from the host-galaxy nucleus, if present, is subdominant and does not represent a significant source of contamination. The complete 0.3–10 keV X-ray light curve of AT 2018cow is shown in Figure 4.
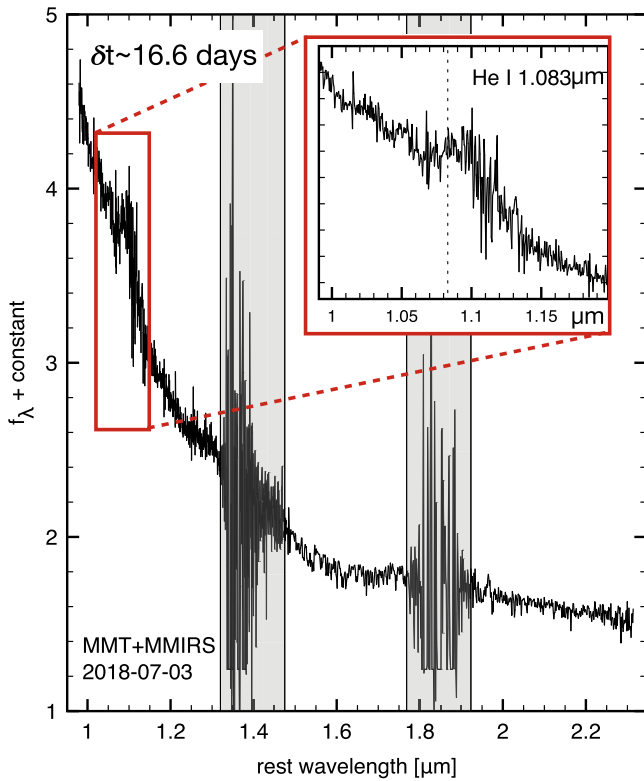
Figure 3. An NIR spectrum of AT 2018cow acquired at ∼17 days shows the emergence of He I emission with a characteristic redshifted line profile, as observed at optical wavelengths (Figure 2). The gray bands mark regions of strong telluric absorption.
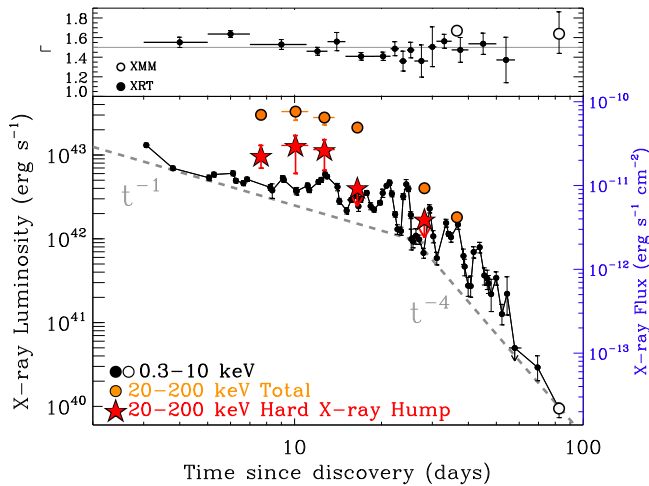

Figure 4. Temporal evolution of AT 2018cow at soft (black, 0.3–10 keV) and hard (orange and red, 20–200 keV) X-ray energies, as captured by *Swift*-XRT, *XMM-Newton*, *NuSTAR*, and *INTEGRAL*. Soft X-rays are well modeled with a power-law spectrum with photon index $\Gamma \sim 1.5$ and limited temporal evolution (upper panel). Above ∼20 keV, an additional transient spectral component appears at $t < 15$ days. Orange dots: total luminosity in the 20–200 keV band. Red stars: contribution of the additional hard X-ray energy component above the extrapolation of the power-law component from lower energies. Dashed gray lines: reference t^{-1} and t^{-4} power-law decays to guide the eye.

2.4. Hard X-Rays: NuSTAR and INTEGRAL

INTEGRAL started observing AT 2018cow on 2018 June 22 18:38:00 UT until July 8 04:50:00 UT ($\delta t \sim 6$–22 days) as part of a public target of opportunity observation. The total on-source
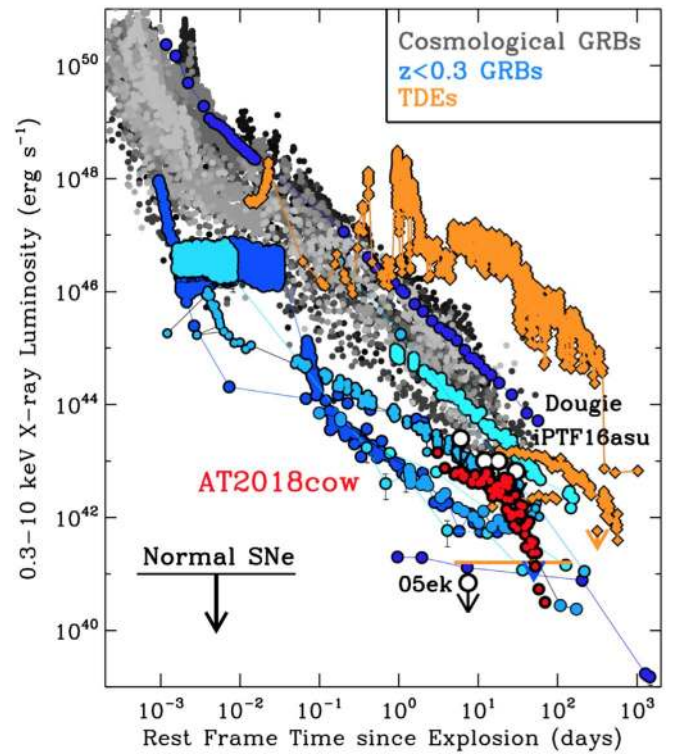

Figure 5. X-ray emission from AT 2018cow (red circles) in the context of long GRBs at cosmological distances (shades of gray), long GRBs in the local universe (shades of blue), tidal disruption events (TDEs; orange diamonds), and normal core-collapse SNe (black arrow and circle), which later show $L_X < 10^{41}$ erg s^{-1}. The upper limits on the X-ray emission from the very rapidly declining type Ic SN 2005ek; the rapidly rising iPTF16asu, which later showed a Ic-BL spectrum (Whitesides et al. 2017); and the fast-rising and luminous transient "Dougie" are marked with empty circles. AT 2018cow is significantly more luminous than normal SNe and competes in luminosity with local GRBs. References: Margutti et al. (2013a, 2013b), Drout et al. (2013), Vinkó et al. (2015), Margutti et al. (2017), Ross & Dwarkadas (2017), and Eftekhari et al. (2018).

time is ∼900 ks (details are provided in Table 5). A source of hard X-rays is clearly detected at the location of AT 2018cow at energies ∼30–100 keV with significance 7.2σ at $\delta t \sim 6$ days. The source is no longer detected at $\delta t \gtrsim 24$ days (Figure 6). After reconstructing the incident photon energies with the latest available calibration files, we extracted the hard X-ray spectrum from the ISGRI detector (Lebrun et al. 2003) on the IBIS instrument (Ubertini et al. 2003) of *INTEGRAL* (Winkler et al. 2003) for each of the ∼2 ks long individual pointing of the telescope dithering around the source. We used the Off-line Scientific Analysis Software (OSA) with a sky model comprising only AT 2018cow, which is the only significant source in the field of view. The energy binning was chosen to have 10 equally spaced logarithmic bins between 25 and 250 keV, the former being the current lower boundary of the ISGRI energy window. We combined the spectra acquired in the same *INTEGRAL* orbit. We use these spectra in Section 2.5 to perform a time-resolved broadband X-ray spectral analysis of AT 2018cow.

We acquired a detailed view of the hard X-ray properties of AT 2018cow between 3 and 80 keV with a sequence of four *NuSTAR* observations obtained between 7.7 and 36.5 days (PI Margutti; Table 6). The *NuSTAR* observations were processed using NuSTARDAS v1.8.0 along with the *NuSTAR* CALDB released on 2018 March 12. We extracted source spectra and light curves for each epoch using the nuproducts FTOOL
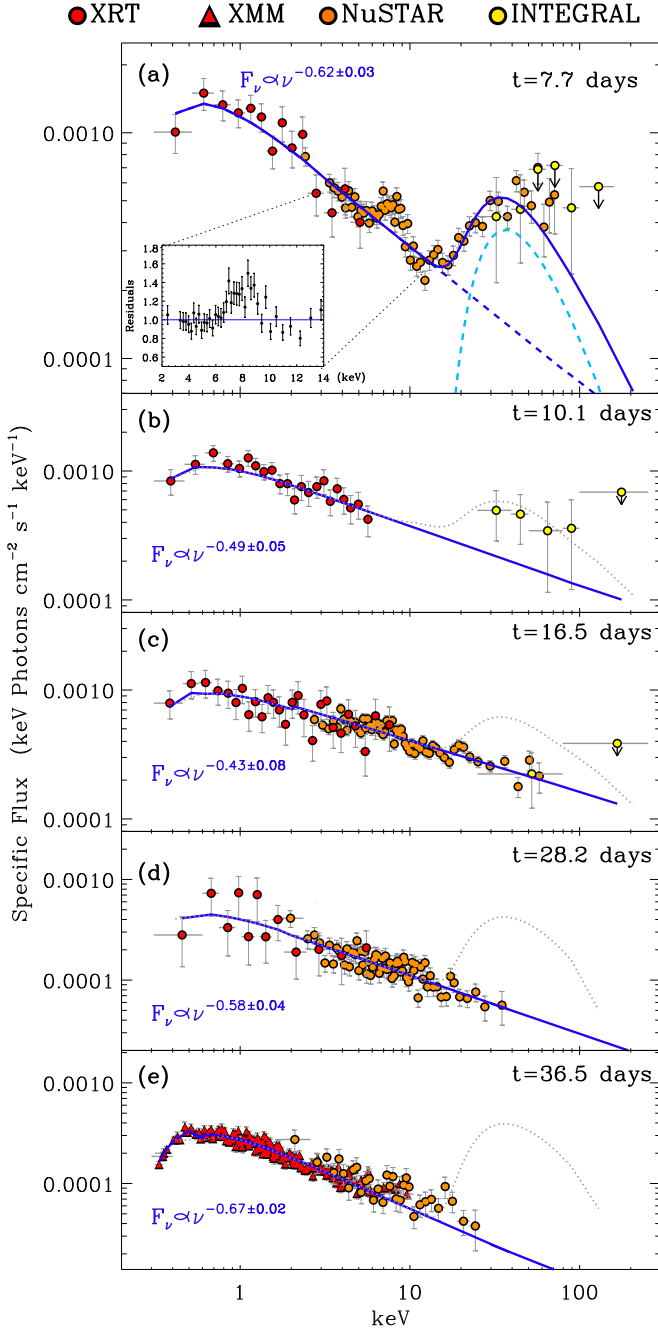
Figure 6. Broadband X-ray spectral evolution of AT 2018cow. Coordinated observations of *Swift*-XRT, *XMM-Newton*, *INTEGRAL*, and *NuSTAR* revealed the presence of a hard X-ray emission component that dominates the spectrum above ~15 keV at early times ≲15 days (dashed light-blue line in panel (a)). The hard X-ray component later subsides. At $\delta t > 15$ days, the broadband X-ray spectrum is well described by an absorbed power law with negligible intrinsic absorption (thick blue line in panels (b)–(d)). Black dotted line: early-time hard X-ray "bump." Inset of panel (a): zoom-in into the region of positive residuals around 6–10 keV.

using a 30″ extraction region centroided on the peak source emission. For the background spectra and light curves, we extracted the data from a larger region (~85″) located on the same part of the focal plane. We produced response files (RMFs and ARFs) for each FPM and for each epoch using the standard `nuproducts` flags for a point source.

AT 2018cow is well detected at all epochs. The first *NuSTAR* spectrum at 7.7 days shows a clear deviation from a pure

absorbed power-law model with $\Gamma \sim 1.5$ and reveals instead the presence of a prominent excess of emission above ~15 keV, which matches the level of the emission captured by *INTEGRAL*, together with spectral features around 7–9 keV. By day 16.5, the hard X-ray bump of emission disappeared, and the spectrum is well modeled by an absorbed power law (Figure 6). We model the evolution of the broadband X-ray spectrum as detected by *Swift*-XRT, *XMM-Newton*, *NuSTAR*, and *INTEGRAL* in Section 2.5.

2.5. Joint Soft X-Ray and Hard X-Ray Spectral Analysis

Our coordinated *Swift*-XRT, *XMM-Newton*, *NuSTAR*, and *INTEGRAL* monitoring of AT 2018cow allows us to extract five epochs of broadband X-ray spectroscopy (~0.3–100 keV) from 7.7 days to 36.5 days. We performed joint fits of data acquired around the same time, as detailed in Table 7. Our results are shown in Figure 6. We find that the soft X-rays at energies ≲7 keV are always well described by an absorbed simple power-law model with photon index $\Gamma \approx 1.5$–1.7 with no evidence for absorption from neutral material in addition to the Galactic value. Our most constraining limits from the time-resolved analysis are $N_{\rm H,int} < (0.03 - 0.04) \times 10^{22}\,{\rm cm}^{-2}$ (Table 7).

Remarkably, at ~7.7 days, *NuSTAR* and *INTEGRAL* data at $E > 15$ keV reveal the presence of a prominent component of emission of hard X-rays that dominates over the power-law component.[42] We model the hard X-ray emission component with a strongly absorbed cutoff power-law model (light-blue dashed line in Figure 6, top panel). This is a purely phenomenological model that we use to quantify the observed properties of the hard emission component. A cutoff power law is preferred to a simple power-law model, as a simple power law would overpredict the highest energy data points at 7.7 days. From this analysis, the luminosity of the hard X-ray component at $\delta t \sim 7.7$ days is $L_{\rm x,hard} \sim 10^{43}\,{\rm erg\,s}^{-1}$ (20–200 keV). A joint analysis of *Swift*-XRT+*INTEGRAL* data at $\delta t \sim 10.1$ days indicates that the component of hard X-ray emission became less prominent, and then disappeared below the level of the soft X-ray power law by $\delta t \sim 16.5$ days, as revealed by the coordinated *Swift*-XRT, *XMM*, and *NuSTAR* monitoring (Figure 6). We derive upper limits on the luminosity of the undetected hard X-ray emission component at $\delta t \geqslant 16.5$ days assuming a similar spectral shape to the one observed at $\delta t \sim 7$–10 days. As shown in Figure 4, the hard X-ray component fades quickly below the level of the power-law component that dominates the soft X-rays, which at this time evolves as $L_{\rm x} \propto t^{-1}$. The hard and soft X-ray emission components clearly show a distinct temporal evolution, suggesting that they originate from different emitting regions. Table 1 lists the energy radiated by each component of emission.

We note that the first spectrum at 7.7 days shows positive residuals around ~6–9 keV (Figure 6, inset). Typical spectral features observed in accretion disks (both around X-ray binaries and active galactic nuclei, AGNs) and interacting SNe are Fe Kα emission (between 6.4 and 6.97 keV depending on the ionization state) and the Fe K-band absorption edge. Typical interpretations of blueshifted iron-line profiles include

---

[42] It is interesting to note in this respect the faint hard X-ray emission detected by *Swift*-BAT in the first 15 days, with flux consistent with the *NuSTAR* observations; see Figure 1 in Kuin et al. (2019).

Table 1
Energy Radiated by AT 2018cow at $3 < \delta t < 60$ days

Component	Band	Radiated Energy (erg)
Power law	0.3–10 keV	$9.8^{+0.2}_{-0.1} \times 10^{48}$
Power law	0.3–50 keV	$2.5^{+0.4}_{-0.3} \times 10^{49}$
Hard X-ray bump	20–200 keV	$\sim 10^{49}$
Blackbody	UVOIR	$1.0^{+0.2}_{-0.2} \times 10^{50}$
Non-thermal[a]	UVOIR	$\sim 5 \times 10^{48}$
Total		$\sim 1.4 \times 10^{50}$ erg

Note.
[a] Based on the analysis from Perley et al. (2019).

edge-on (or highly inclined) accretion disks or highly ionized absorption (e.g., Reeves et al. 2004). As a reference, interpreting the spectral feature detected in AT 2018cow at $E \sim 8$ keV with width ~ 1 keV as Fe emission would require a blueshift corresponding to $v \sim 0.1c$ and Doppler broadening with similar velocity. We discuss possible physical implications in Section 3.3.3.

2.6. Radio: VLA and VLBA

We observed AT 2018cow with the Karl G. Jansky Very Large Array (VLA) starting from $\delta t \sim 82$ days until $\delta t \sim 150$ days. The data were taken in the VLA's D configuration under program VLA/18A-123 (PI Coppejans). We reduced the data using the pwkit package (Williams et al. 2017), using 3C 286 as the bandpass calibrator and VCS1 J1609+2641 as the phase calibrator. We imaged the data using standard routines in CASA (McMullin et al. 2007) and determined the flux density of the source at each frequency by fitting a point-source model using the imtool package within pwkit. This package uses a Levenberg–Marquardt least-squares optimizer to fit a small region in the image plane centered on the source coordinates with an elliptical Gaussian corresponding to the CLEAN beam. These data are shown together with the rest of our radio observations in Figure 7 and Table 8.

We also obtained 22.3 GHz VLBI observations of AT 2018cow with the High Sensitivity Array of the National Radio Astronomy Observatory (NRAO) on 2018 July 7 (Bietenholz et al. 2018). The array consisted of the NRAO Very Long Baseline Array with the exception of the North Liberty station (9×25 m diameter) and the Effelsberg antenna (100 m diameter). We recorded both senses of circular polarization at a total bit rate of 2048 Mbit s^{-1}. The observations were phase-referenced to the nearby compact source QSO J1619+2247, with a cycle time of ~ 100 s. The amplitude gains were calibrated using the system temperature measurements made by the VLBA online system and refined by self-calibration on the calibrator sources, with the gains normalized to a mean amplitude of unity to preserve the flux-density scale as much as possible. We will report on the VLBI results in more detail in a future paper, but we include the total flux density observed with VLBI here. On 2018 July 7.96 (UT), we found 5850 ± 610 μJy at 22.3 GHz. The value was obtained by fitting a circular Gaussian directly to the visibilities by least squares. As the source is not resolved, the nature of the model does not affect the flux density, and a value well within our stated uncertainties is obtained if, for example, a circular disk model is used. The array has good u–v coverage down to

baselines of length <30 Mλ; therefore, only flux density on angular scales >8 mas would be resolved out. At this epoch, the projected angular size of AT 2018cow is <8 mas even in the case of relativistic expansion, which implies that our measurement of the radio flux density from AT 2018cow is reliable. The uncertainty is the statistical one with a 10% systematic one added in quadrature. Although at our observing frequency of 22.3 GHz some correlation losses might be expected, the visibility phases were consistent from scan to scan, and we do not expect correlation losses larger than our stated uncertainty.

From our modeling of the VLA measurements at $t > 80$ days, we find that the radio SEDs are well described by a smoothed broken power law with decreasing spectral peak flux $F_{\rm pk} \propto t^{-1.7\pm0.1}$ and peak frequency $\nu_{\rm pk} \propto t^{2.2\pm0.1}$ (thick lines in Figure 7). At $\nu > \nu_{\rm pk}$, the optically thin part of the spectrum scales as $F_\nu \propto \nu^{-1.4\pm0.1}$, while below the spectral peak we find $F_\nu \propto \nu^{1.2\pm0.1}$. We place our VLBA and VLA measurements in the context of radio observations from the literature (An 2018; Bright et al. 2018; de Ugarte Postigo et al. 2018a; Dobie et al. 2018a, 2018b, 2018c; Ho et al. 2019; Horesh et al. 2018; Nayana & Chandra 2018; Smith et al. 2018a). An extrapolation of this model back in time shows that this model adequately represents the evolution of AT 2018cow at $t > 35$ days (Figure 7). At earlier times, the optically thin spectrum scales as $F_\nu \sim \nu^{-1.0}$, and we find evidence for a steeper optically thick spectrum $F_\nu \propto \nu^2$. A detailed discussion of the modeling of the entire data set will be presented in D. L. Coppejans et al. (2018, in preparation).

The radio luminosity and temporal behavior of AT 2018cow at ~ 9 GHz are more similar to those of the most luminous normal SNe, while AT 2018cow is significantly less luminous than cosmological GRBs (Figure 8). However, differently from radio SNe that show a constant $F_{\rm pk}$ with time and $\nu_{\rm pk} \propto t^{-1}$ (e.g., Chevalier 1998; Soderberg et al. 2005, 2012), in AT 2018cow the peak flux rapidly decreases with time. The rising light curve until $\delta t \sim 100$ days also makes it distinct from low-energy GRBs in the local universe (Figure 8). The radio flux-density measurements of AT 2018cow are presented in Table 8.

2.7. Search for Prompt γ-Rays with the IPN

The large X-ray luminosity of AT 2018cow initially suggested a connection with long GRBs. Thus motivated, we searched for bursts of prompt γ-ray emission between the time of the last optical non-detection and the first optical detection of AT 2018cow (i.e., between 2018 June 15 03:08 UT and June 16 10:35 UT; Prentice et al. 2018). During this time interval, one burst was detected on 2018 June 15 11:05:56 UT by the spacecraft of the Inter-Planetary Network (IPN; *Mars Odyssey*, Konus/*Wind*, *INTEGRAL* SPI-ACS, *Swift*-BAT, and *Fermi*-GBM). The burst localization by the IPN, *INTEGRAL*, and the GBM, however, excludes at high confidence the location of AT 2018cow, from which we conclude that there is no evidence for a burst of γ-rays associated with AT 2018cow down to the IPN threshold (i.e., 10 keV–1 MeV 3 s peak flux $< 3 \times 10^{-7}$ erg cm^{-2} s^{-1} for a typical long GRB spectrum with Band parameters $\alpha = -1$, $\beta = -2.5$, and $E_p = 300$ keV; e.g., Band et al. 1993). For the time interval of interest, the IPN duty cycle was $\sim 97\%$. For AT 2018cow, the IPN thus rules out at 97% c.l. bursts of γ-rays with peak luminosity $> 10^{47}$ erg s^{-1},
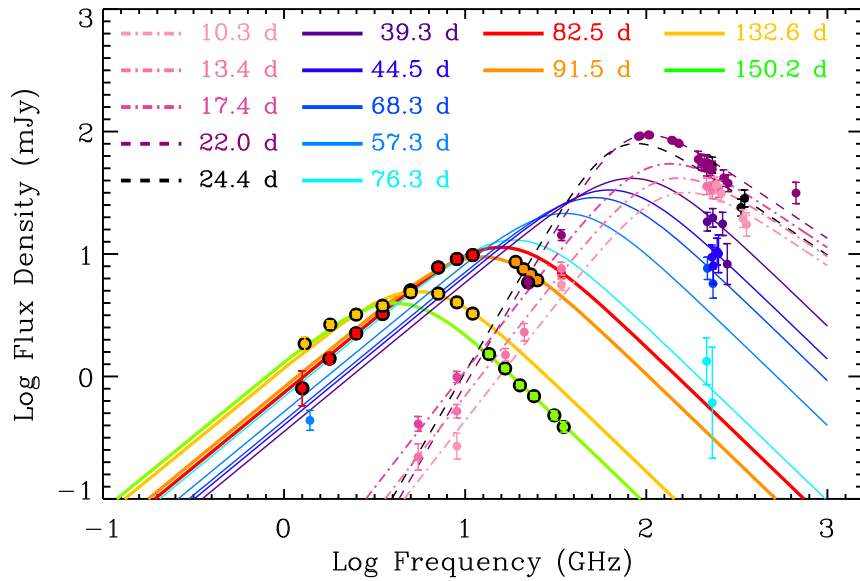
Figure 7. The temporal evolution of the radio spectrum of AT 2018cow at $t > 10$ days is well described by a smoothed broken power-law model with decreasing peak frequency ν_{pk}. Symbols with black contours: VLA and VLBI data presented in this paper. Other data in the plot have been collected from Ho et al. (2019), Bright et al. (2018), Smith et al. (2018a), Dobie et al. (2018a, 2018b, 2018c), Nayana et al. (2018), Nayana & Chandra (2018), Horesh et al. (2018), and An (2018). The model that best fits the VLA data set at $t > 80$ days has $F_{pk} \propto t^{-1.7 \pm 0.1}$ and $\nu_{pk} \propto t^{-2.2 \pm 0.1}$, with an optically thin spectral index $\beta_1 = 1.4 \pm 0.1$ and an optically thick index $\beta_2 = 1.2 \pm 0.1$.

which is the level of the lowest luminosity GRBs detected (e.g., Nava et al. 2012).

We now examine which limits we can place on the probability of detection of weaker bursts, which would only trigger *Fermi*-GBM and/or *Swift*-BAT in the same time interval considerd above. Taking Earth-blocking and duty cycle into account, the joint non-detection probability by *Fermi*-GBM (8–1000 keV fluence limit of $\sim 4 \times 10^{-8}\,\mathrm{erg\,cm^{-2}}$) and *Swift*-BAT (15–150 keV fluence limit of $\sim 6 \times 10^{-9}\,\mathrm{erg\,cm^{-2}}$ based on the weakest burst detected within the coded field of view, FOV) is $\sim 29\%$. The non-detection probability of weaker bursts by *Swift*-BAT is $\sim 71\%$ (within the coded FOV) and $\sim 46\%$ (outside the coded FOV).

2.8. Bolometric Emission and Radiated Energy

Performing a self-consistent flux calibration of the UVOT photometry and applying a dynamical count-to-flux conversion that accounts for the extremely blue colors of the transient, we find that the UV+*UBV* emission from AT 2018cow is well modeled by a blackbody function at all times. We infer an initial temperature $T_{bb} \sim 30{,}000$ K and radius $R_{bb} \sim 8 \times 10^{14}$ cm, consistent with Perley et al. (2019). R_{bb} and T_{bb} show a peculiar temporal evolution, with R_{bb} monotonically decreasing with time (with a clear steepening around 20 days), while the temperature plateaus at $\sim 15{,}000$ K, with no evidence for cooling at $\delta t > 20$ days (Figure 9). Indeed, $\delta t \sim 20$ days marks an important transition in the evolution of AT 2018cow: H and He features emerge in the spectra, the hard X-ray hump disappears, L_X approaches the level of the optical emission and later starts a steeper decline, while the soft X-ray variability becomes more pronounced with respect to the continuum.

After the optical peak, we find that the resulting UV/optical bolometric emission is well modeled by a power-law decay $t^{-\alpha}$ with best-fitting $\alpha = 2.50 \pm 0.06$ (Figure 9), in agreement with Perley et al. (2019). Also consistent with Perley et al. (2019), we find that the *R*, *I*, and NIR data from AT 2018cow are in clear

excess of the thermal blackbody emission and represent a different component. In Figure 9, we show that the combined energy release of the thermal UV/optical emission and the soft X-rays (0.3–50 keV) follows a decay $\propto t^{-\alpha}$ with $\alpha = 1.94 \pm 0.04$. This result is relevant if the thermal optical/UV and the soft X-rays are manifestations of the same physical component, like energy release from a central engine (Section 3.1.1). Table 1 lists the energy radiated by each component of emission.

2.9. Temporal Variability Analysis

We examined the 0.3–10 keV emission at $\delta t = 3.5$–55 days for evidence of periodicity using the Lomb–Scargle period-ogram (LSP; Lomb 1976; Scargle 1982), and the Fast χ^2 algorithm[43] by Palmer (2009), both of which are suitable for unevenly spaced series. As a first step, we removed the overall trend of the time series, which was found to be best modeled by a simple exponential $\exp(k - t/t^*)$, with $k = -0.82 \pm 0.08$ and $t^* = 14.7 \pm 0.9$ days. We applied the LSP and the Fast χ^2 techniques to the resulting residuals.

We calculated the LSP using the Numerical Recipes implementation (Press et al. 1992), exploring the frequency range 0.005–0.65 day^{-1}, corresponding to $1/(4T)$ and to an average Nyquist frequency, respectively, where T is the total duration. To assess the significance of the peaks we detected, one must consider two issues: (i) the presence of red noise and (ii) the number of independent frequencies (e.g., Horne & Baliunas 1986). We addressed (i) through a number of Monte Carlo simulations. We generated 5×10^3 time series with the same sequence of observing times, t_i, every time shuffling the observed count rates and associated uncertainties so as to keep the same rate distribution and the same variance. For each of the simulated series, we calculated the LSP under the same prescriptions as for the real one. We addressed (ii) through the identification of the peaks in all of the LSPs (both the true one
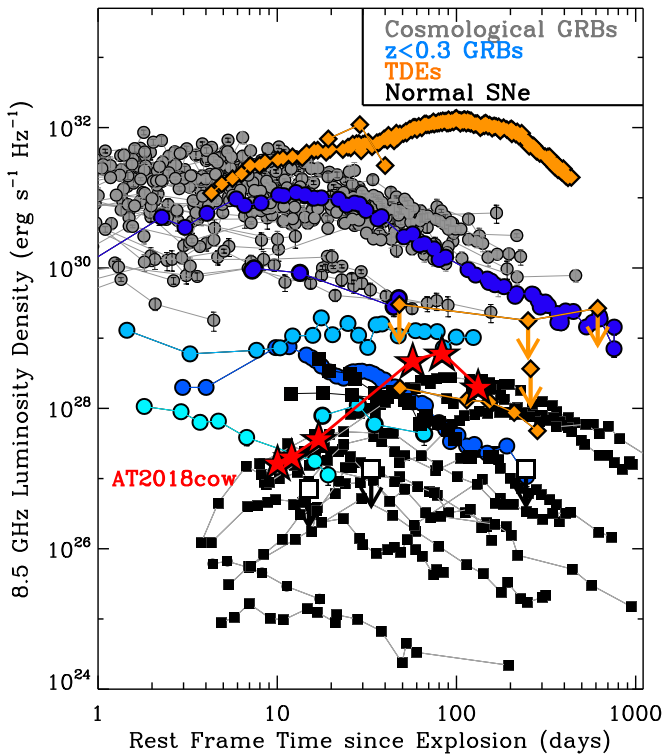
---

[43] http://public.lanl.gov/palmer/fastchi.html

9

Figure 8. Radio emission from AT 2018cow (red stars), in the context of long GRBs (gray circles for GRBs at cosmological distances and shades of blue for GRBs in the local universe), TDEs (orange diamonds), and normal H-stripped core-collapse SNe including Ic-BL (black squares). The empty square at $t <$ 20 days marks the position of the extremely rapidly declining SN Ic 2005ek, which was not detected in the radio, while the empty squares at $t > 20$ days mark the upper limits to the radio emission from the rapidly rising iPTF16asu, which showed Ic-BL spectral features at later times. The temporal evolution and luminosity of AT 2018cow are comparable to those of the most luminous normal SNe. References: Berger et al. (2012), Cenko et al. (2012b), Chomiuk et al. (2012), Chandra & Frail (2012), Zauderer et al. (2013), Drout et al. (2013), Chornock et al. (2014), Margutti et al. (2013b), Nicholl et al. (2016), Alexander et al. (2016), Margutti et al. (2017), Whitesides et al. (2017), and Eftekhari et al. (2018).

and the ones from the shuffled data) by means of the peak-search algorithm MEPSA (Guidorzi 2015): given that only separate peaks are identified as independent structures, this properly accounts for the power associated with correlated frequencies. The significance of the peaks found in the real LSP was then compared against the distribution of peaks in the LSPs from the shuffled data. The result is shown in Figure 10.

We further apply the Fast χ^2 algorithm to detect periodic harmonic signals within unevenly spaced data affected by variable uncertainties. For a given number of harmonics and any given trial frequency, the Fast χ^2 algorithm determines the solution that minimizes the χ^2. This way, for a given number of harmonics, the best fundamental frequency along with its harmonics is given by the global minimum χ^2. We applied the method to the observed X-ray detrended light curve, each time allowing for one to six harmonics, as a trade-off between the need to provide a relatively simple modeling and the possibility of a rather complex periodic signal involving several harmonics. The explored frequencies are in the range 0.05–1 day^{-1}. To assess the significance of our results, we applied Fast χ^2 to the sample of synthetic light curves and compared the results from the real time series. We find significant power ($\sim 3\sigma$ Gaussian) on a modulation timescale of $\sim$4 days in the first 40 days,

consistent with the results from the LSP. We note that a similar variability timescale was also independently reported by Kuin et al. (2019).

Finally, we investigate whether there is correlated temporal variability between the X-ray and the UV/optical in AT 2018cow. We fit a third-order polynomial to the soft X-ray, $w1$, $w2$, and $m2$ light curves in log–log space to remove the overall temporal decay trend. Our time series consists of the ratios of the observed fluxes over the best-fitting "continuum," where uncertainties have been propagated following standard practice. We find that all of the UV light curves show a high degree of correlation with p-values $<0.01\%$ for either the Spearman Rank test or the Kendall Tau test. We also find a hint for correlated behavior between the UV bands and the X-rays with limited significance corresponding to $P \gtrsim 5\%$ (Spearman Rank test). The correlation is stronger at $\delta t < 30$ days.

3. Multiband Inferences

In this section, we discuss basic inferences on the physical properties of AT 2018cow based on the information provided by each part of the electromagnetic spectrum individually, before synthesizing the information and speculating on the intrinsic nature of AT 2018cow in Section 4.

3.1. Thermal UV–Optical Emission

The key observational results are: (i) a very short rise time to peak, $t_{\rm rise} \sim$ few days (Perley et al. 2019; Prentice et al. 2018). (ii) Large bolometric peak luminosity, $L_{\rm pk,bol} \sim 4 \times 10^{44}$ erg s^{-1}, significantly more luminous than normal SNe and more luminous than some SLSNe (Figure 1). (iii) Persistent blue colors, with lack of evidence for cooling at $\delta t \gtrsim 30$ days (the effective temperature remains $> 15,000$ K). (iv) Large blackbody radius $R_{\rm bb} \sim 8 \times 10^{14}$ cm inferred at $\delta t \sim 3$ days (Figure 9). (v) Persistent optically thick UV/optical emission with no evidence for transition into a nebular phase at $\delta t < 90$ days (Figure 2). (vi) The spectra evolve from a hot, blue, and featureless continuum around the optical peak, to very broad features with $v \sim 0.1\,c$ at $\delta t \sim$ 4–15 days (Figure 2). (vii) Redshifted H and He features emerge at $\delta t > 20$ days with significantly lower velocities $v \sim 4000$ km s^{-1} (Figure 2), implying an abrupt change of the velocity of the material which dominates the emission. The centroid of the line emission is offset to the red with $v \sim 1000$ km s^{-1} (Figure 2). (viii) There is evidence for an NIR excess of the emission with respect to a blackbody model from early to late times, as pointed out by Perley et al. (2019; Figure 11).

3.1.1. Engine-powered Transient

For optical/UV emission powered by the diffusion of thermal radiation from an initially compact opaque source, the light curve rises and peaks on the diffusion timescale (Arnett 1982),

$$t_{\rm pk} \approx \left(\frac{M_{\rm ej}\kappa}{4\pi v_{\rm ej}c} \right)^{1/2} \approx 2.7 \ {\rm days} \left(\frac{M_{\rm ej}}{0.3 M_\odot} \right)^{1/2} \left(\frac{v_{\rm ej}}{0.1c} \right)^{-1/2}, \quad (1)$$

where we use $\kappa = 0.1$ cm^2 g^{-1} as an estimate of the effective opacity due to electron scattering or Doppler-broadened atomic lines. For $t_{\rm pk} \sim 2$–4 days (Figure 1), Equation (1) implies a low ejecta mass $M_{\rm ej} \sim 0.1$–$0.5\,M_\odot$ and high ejecta velocity $v_{\rm ej} \sim 0.05$–$0.1c$ to match the inferred blackbody radius at early times, corresponding to a kinetic energy of the optical/UV-emitting
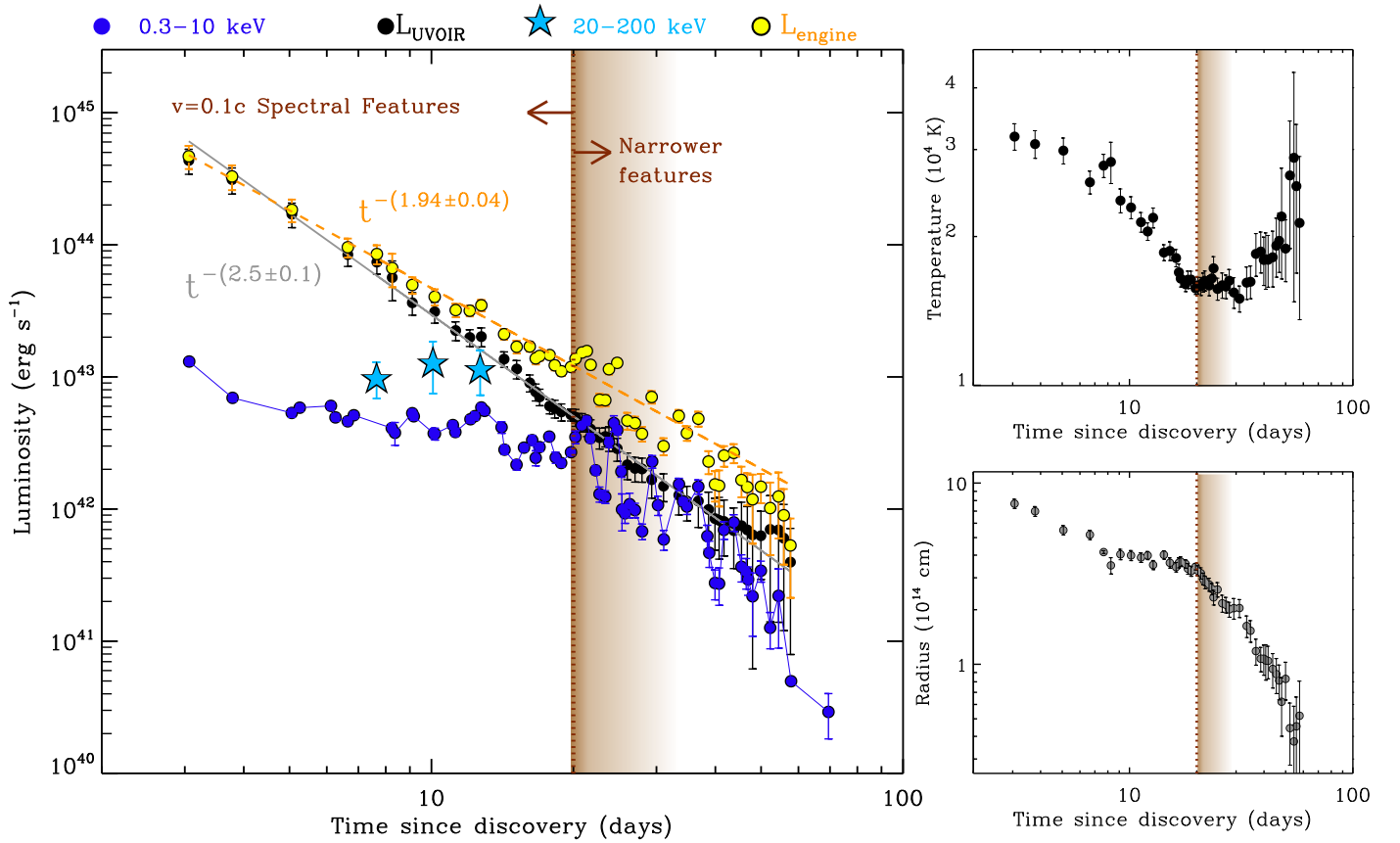
Figure 9. (Left panel) luminosity evolution of different components of emission: soft X-ray 0.3–10 keV (L_X; blue filled circles), hard X-ray bump of emission in the 20–200 keV band (light-blue stars), optical bolometric luminosity estimated from a blackbody fit to the UV/optical photometry ($L_{UVOIR} \propto t^{-2.5\pm0.1}$; black circles). Yellow circles: "engine" luminosity ($L_{engine} = L_X + L_{UVOIR} \propto t^{-1.94\pm0.04}$, where L_X has been integrated between 0.3-50 keV). (Right panels) evolution of the best-fitting blackbody temperature (upper panel) and radius (lower panel). Brown shaded areas mark the approximate time of onset of narrower spectral features in the optical spectra. Interestingly, $\delta t \sim 20$ days marks an important time in the evolution of AT 2018cow: $L_X \approx L_{UVOIR}$, the rate of decay of L_X increases and the X-ray variability becomes more prominent, the blackbody temperature plateaus with no evidence for cooling at $\delta t > 20$ days, while the radius decreases at a faster rate. Notably, around this time, broader H and He spectral features emerge in the optical spectra (Figure 2), while the hard X-ray spectral "hump" completely disappears.
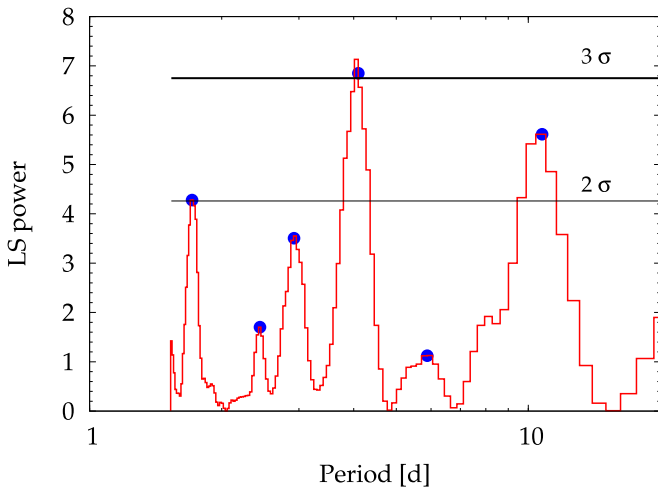

Figure 10. Lomb–Scargle periodogram for the 0.3–10 keV X-ray time series. Horizontal lines correspond to the significance levels (Gaussian). The most significant peak (3σ) is found on a period of $T_1 = 4.0$ days. Two other peaks above 2σ are at $T_2 = 10.4 \pm 2.1$ days (2.6σ) and one at $T_3 = 1.7 \pm 0.1$ days (2.0σ), respectively.

material $E_k \sim 10^{50.5}$–$10^{51.5}$ erg (consistent with the inferences by Perley et al. 2019 and Prentice et al. 2019). The low ejecta mass immediately excludes light-curve models powered by ^{56}Ni decay,

which would require $M_{Ni} > 6\,M_\odot$ to reproduce the large peak luminosity of AT 2018cow, and instead demands another energy source. We note that $M_{ej} \sim 0.1$–$0.5 M_\odot$ should be viewed as a constraint on the fast-moving ejecta mass that participates in the production of the high-luminosity peak. As we will see in the next sections, the phenomenology of AT 2018cow requires the presence of additional, slower material preferentially distributed in an equatorial belt.

One potential central energy source is an "engine," such as a millisecond magnetar or accreting black hole, which releases a total energy E_e over its characteristic lifetime, t_e. The engine deposits energy into a nebula behind the ejecta at a rate

$$L_e(t) = \frac{E_e}{t_e} \frac{(\alpha - 1)}{(1 + t/t_e)^\alpha}, \qquad (2)$$

where $\alpha = 2$ for an isolated magnetar (Spitkovsky 2006), $\alpha = 2.38$ for an accreting magnetar (Metzger et al. 2018), $\alpha = 5/3$ for fallback in a TDE (e.g., Rees 1988; Phinney 1989), and $\alpha < 5/3$ in some supernova fallback models (e.g., Coughlin et al. 2018) or viscously spreading disk accretion scenarios (e.g., Cannizzo et al. 1989). In engine models, the late-time decay of the bolometric luminosity obeys $L_{opt} \propto L_e \propto t^{-\alpha}$, such that the measured value of $\alpha \approx 2$–2.5
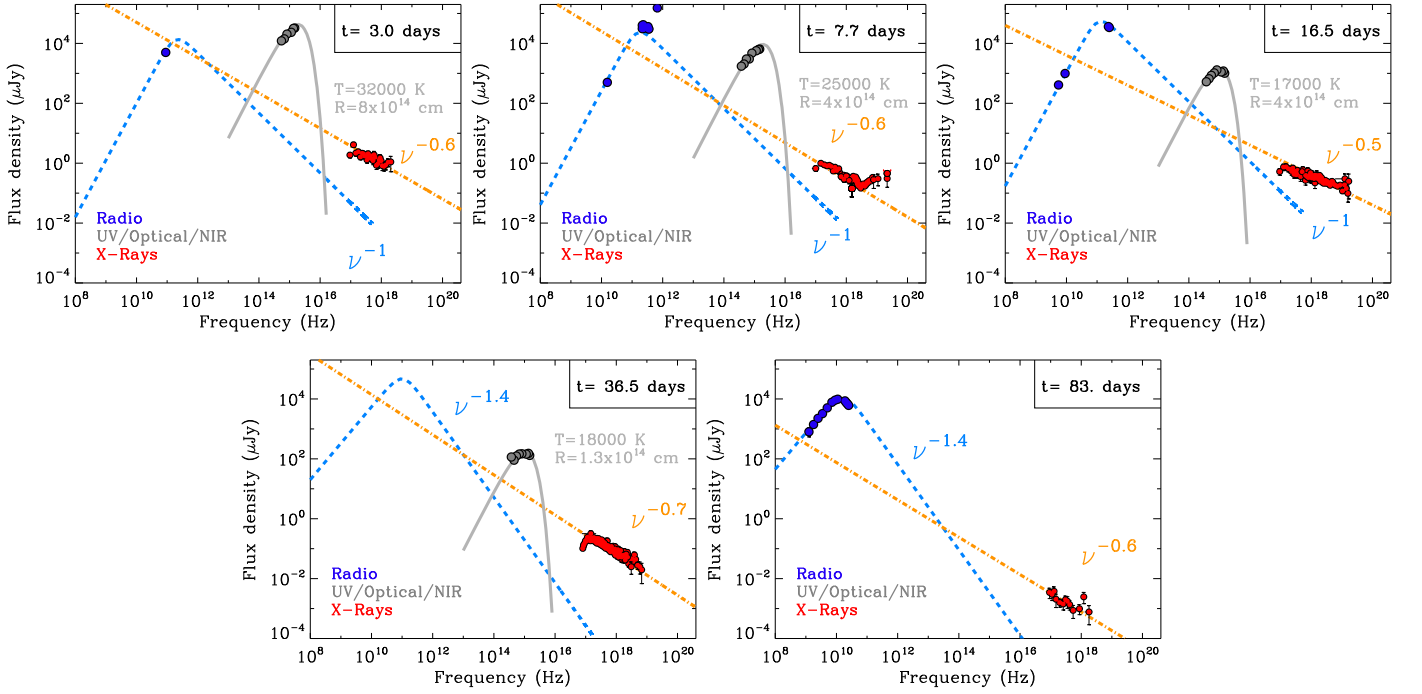
Figure 11. Evolution of the broadband radio to hard X-ray spectrum of AT 2018cow from around the time of optical peak at 3 days to the time of the last X-ray detection at 83 days. The presence of the excess of emission at hard X-rays is clearly apparent in the 7.7 day SED. Blue, gray, and red filled circles mark radio, optical, and X-ray observations, respectively. The radio data shown in the SEDs at $\delta t < 20$ days are from Ho et al. (2019), de Ugarte Postigo et al. (2018b), Bright et al. (2018), and Dobie et al. (2018a). Orange dotted–dashed line: best-fitting power-law model from Section 2.5. Blue dashed line: best-fitting radio model from Section 2.6. Gray thick line: best-fitting blackbody model from Section 2.8. The X-ray, optical, and radio originate from three distinct emission components with different temporal and spectral evolution. The SED at 7.7 days collects radio measurements obtained between ∼6–8 days. Notable is the highest frequency radio data point, which might be connected to the non-thermal component invoked by Perley et al. (2019) to explain the NIR excess.

(Section 2.8, Figure 9) would be consistent with a magnetar engine.[44] However, given the uncertainties in the bolometric correction, the TDE/supernova fallback case ($\alpha = 5/3$) may also be allowed. Finally, the "engine" may not be a compact object at all, but rather a deeply embedded radiative shock, produced as the ejecta interact with a dense medium.

As a concrete example, consider an isolated magnetar ($\alpha = 2$), which at times $t \gg t_e$ obeys $L_e \approx (E_e t_e)/t^2$. Assuming that most of the energy is released over $t_e \ll t_{pk}$ (as justified by the narrowly peaked light-curve shape) and that most of the engine energy is not radiated, but instead used to accelerate the ejecta to its final velocity v_{ej}, then $E_e \gtrsim M_{ej} v_{ej}^2/2$, with $E_{rad} \approx \int_{t_{pk}}^{\infty} L_e dt \approx E_e t_e/t_{pk}$, from which it follows that

$$t_e \gtrsim \frac{2E_{rad}}{M_{ej} v_{ej}^2} t_{pk} \sim 3 \times 10^3 \mathrm{s} \left(\frac{v_{ej}}{0.1c}\right)^{-2} \left(\frac{M_{ej}}{0.3 M_\odot}\right)^{-1}. \quad (3)$$

Here we used the total radiated UVOIR energy, $E_{rad} \sim 10^{50}$ erg from Table 1. The engine is thus relatively constrained: it must release a total energy E_e that varies from $E_{rad} \sim 10^{50}$ erg to $E_k \sim 10^{50.5}$–$10^{51.5}$ erg, most of it over a characteristic lifetime $t_e \sim 10^3$–10^5 s.

---

[44] A precise measurement of the late-time optical decay will only be possible after AT 2018cow has faded away (allowing us to accurately remove the host-galaxy contribution). Here we note that steeper decays of L_{opt} would also be consistent with a magnetar engine shining through low ejecta mass, which become "transparent" and incapable of retaining and thermalizing the engine energy. A similar scenario was recently invoked by Nicholl et al. (2018) to explain the rapid decay of the SLSN 2015bn at late times.

We conclude with constraints on the properties of a Ni-powered transient that might be hiding within the central-engine-dominated emission. In the context of the standard Arnett (1982) modeling, modified following Valenti et al. (2008), and assuming a standard SN-like explosion with $M_{ej} \sim$ a few $M_\odot$ and $E_k \sim 10^{51}$–10^{52} erg, we place a limit $M_{Ni} < 0.06 M_\odot$ to not overproduce the observed optical–UV thermal emission, consistent with Perley et al. (2019). The limit becomes significantly less constraining, $M_{Ni} < 0.2$–$0.4 M_\odot$, if we allow for smaller $M_{ej} \sim 0.5 M_\odot$, as in this case the diffusion timescale is shorter (i.e., the transient emission peaks earlier), the γ-rays from the ^{56}Ni decay are less efficiently trapped and thermalized within the ejecta, and the transient enters the nebular phase earlier. However, the large M_{Ni}/M_{ej} would result in red colors as the UV emission would be heavily suppressed via iron-line blanketing, which is not observed. The observed blue colors (Figure 1) indicate instead that emission from a Ni-powered transient with small ejecta is never dominant, which implies $M_{Ni} \lesssim 0.1 M_\odot$.

3.1.2. Shock Breakout

Alternatively, we consider the possibility that the high luminosity and rapid evolution of AT 2018cow result from a shock breakout from a radially extended progenitor star, an inflated progenitor star, or thick medium (i.e., if the star experiences enhanced mass loss just before stellar death). Shock breakout scenarios have been invoked to explain some fast-rising optical transients (e.g., Ofek et al. 2010; Drout et al. 2014; Arcavi et al. 2016; Shivvers et al. 2016; Tanaka et al. 2016).

For a typical SN shock velocity $v_{\rm sh} \approx 10^4$ km s^{-1} and the observed peak time of AT 2018cow, the inferred stellar radius is $R_\star \approx v_{\rm sh} t_{\rm pk} \gtrsim 10^{14}$ cm $\sim$10 au, much larger than red supergiant stars. Furthermore, the explosion of such a massive star is expected to be followed by a longer plateau phase not observed in the monotonically declining light curve of AT 2018cow. We conclude that shock breakout from a stellar progenitor is not a viable mechanism for AT 2018cow.

The effective radius of a massive star could be increased just prior to its explosion by envelope inflation or enhanced mass loss timed with stellar death, as observed in a variety of SNe (e.g., Smith 2014). Assuming an external medium with a wind-like density profile $\rho_w = \dot{M}_w/(4\pi v_w r^2) = A/r^2$ and radial optical depth $\tau_w = \int_r^\infty \rho_{\rm w} \kappa dr \simeq \rho_w r\kappa$, the photon diffusion timescale is

$$t_{\rm pk,w} \sim \tau_w \frac{r}{c} \approx \frac{A\kappa}{c} \approx 1.9 \, {\rm day} \left(\frac{A}{10^5 A_\star} \right), \quad (4)$$

where $A_\star = 5 \times 10^{11}$ g cm^{-1} (i.e., $A = A_\star$ for the standard mass-loss rate $\dot{M}_w = 10^{-5} M_\odot$ yr^{-1} and wind velocity $v_w = 10^3$ km s^{-1}; e.g., Chevalier & Li 2000). The luminosity of the radiative shock $L_{\rm sh} = (9\pi/8)\rho_w v_{\rm sh}^3 r^2$ at the breakout radius $r = ct_{\rm pk,w}/\tau_w$ is

$$L_{\rm sh}(t_{\rm pk,w}) \simeq \frac{9\pi}{8} v_{\rm sh}^3 \frac{ct_{\rm pk}}{\kappa_{\rm opt}}$$
$$\approx 2 \times 10^{44} \, {\rm erg \, s^{-1}} \left(\frac{t_{\rm pk}}{2 \, {\rm days}} \right) \left(\frac{v_{\rm sh}}{10^4 \, {\rm km \, s^{-1}}} \right)^3. \quad (5)$$

From Equations (5) and (4), we conclude that a shock breakout from an extended medium with density structure corresponding to an effective mass-loss rate $A \sim 10^5 A_\star$ can explain both the timescale and peak luminosity of the optical emission from AT 2018cow. Following the initial breakout, radiation from deeper layers of the expanding shocked wind ejecta would continue to produce emission. However, such a cooling envelope is predicted to redden substantially in time (e.g., Nakar & Piro 2014), in tension with the observed persistently blue optical/UV colors and lack of cooling at $\delta t > 20$ days (Figure 9). We conclude that, even if a shock breakout is responsible for the earliest phases of the optical emission and for accelerating the fastest ejecta layers, a separate, more deeply embedded energy source is needed at late times to explain the properties of AT 2018cow.

3.1.3. Reprocessing by Dense Ejecta and the Spectral Slope of the Optical Continuum Emission

We argued in previous sections that the sustained blue emission from AT 2018cow is likely powered by the reprocessing of radiation from a centrally located X-ray source embedded within the ejecta. Here we discuss details of the reprocessing picture and what can be learned about the ejecta structure of AT 2018cow.

Late-time optical spectra at $\delta t > 20$ days (Figure 2) show line widths of $\sim$4000 km s^{-1} ($\sim$0.01c), indicating substantially lower outflow velocities than at earlier times (when $v \sim 0.1c$), and an abrupt transition from very high velocity to lower velocity emitting material (Figure 9). Although it might be possible to explain this phenomenology in a spherically

symmetric model with a complex density profile, a more natural explanation is that the ejecta/circumstellar medium (CSM) of AT 2018cow is aspherical, e.g., with fast-expanding material along the polar direction and slower expanding dense matter in the equatorial plane (Figure 12). This picture is independently supported by the observed properties of X-ray emission discussed and by the emission-line profiles, as discussed in Sections 3.3 and 3.1.4.[45]

Although we approximated the UV/optical spectral energy distribution (SED) with a blackbody function in Section 2.8, the true SED is likely to deviate from a single blackbody spectrum. The observed slope of the early optical SED, $L_\nu \propto \nu^{1.2}$, can be used to constrain the ejecta stratification in reprocessing models. Ignoring Gaunt factors and using the result from radiative transfer calculations that do not assume local thermodynamic equilibrium (LTE), which indicate that in the outer layers of the reprocessor the free electron temperature T_e tend to level off to a constant value much greater than the effective temperature (e.g., Hubeny et al. 2000; Roth et al. 2016), the free–free emissivity in the optical to infrared is $j_\nu^{\rm ff} \propto n_e n_i \propto \rho^2$ (where n_e and n_i are the number density of electrons and positive ions, respectively, and we used the fact that $h\nu \ll kT_e$). This result holds as long as the material is highly ionized.

While the bound electrons are coupled to the radiation field and are likely to be out of thermal equilibrium, the free electrons should be in LTE, so that $j_\nu^{\rm ff} = \alpha_\nu^{\rm ff} B_\nu(T_e)$. For $h\nu \ll kT_e$, we find $\alpha_\nu^{\rm ff} \propto \rho^2 \nu^{-2}$. We assume that near the surface of the emitting material the density can be locally modeled by a power law in radius $\rho \propto r^{-n}$, for some $n > 1$. Due to the ionization from the engine, electron scattering dominates the opacity. The total optical depth (integrated from the outside in) is then wavelength-independent and $\tau_{\rm es}(r) \sim (1/(n-1))\rho_0 \kappa_{\rm es} r_0^n r^{1-n}$, where r_0 is some reference radius within the region where the power-law expression for the density holds, and $\rho_0 \equiv \rho(r_0)$. Let $\alpha^{\rm es}$ and $\alpha_\nu^{\rm abs}$ denote the opacity coefficients from electron scattering and continuum absorption, respectively. We define an opacity ratio $\epsilon_\nu = \alpha_\nu^{\rm abs}/(\alpha^{\rm es} + \alpha_\nu^{\rm abs}) \approx \alpha_\nu^{\rm abs}/\alpha^{\rm es} \propto \rho\nu^{-2}$.

The effective optical depth to absorption is $\tau_{\rm eff}(\nu) \sim \sqrt{\epsilon_\nu} \tau_{\rm es}$, where $\tau_{\rm es}$ is measured from the outside in, and we evaluate ϵ_ν at the thermalization depth $r_{\nu,\rm therm}$, which is the radius where $\tau_{\rm eff}(\nu) = 1$. We define $\tau_{\rm es}(r_{\nu,\rm therm}) \equiv \tau_{\nu,\rm therm}$. It follows that $\tau_{\nu,\rm therm} \approx 1/\sqrt{\epsilon_\nu} \propto \rho^{-1/2}\nu^1$, which implies that the thermalization radius scales with ν as $r_{\nu,\rm therm} \propto \nu^{\frac{2}{2-3n}}$. Following Roth et al. (2016), we can approximate the observed spectrum as $L_\nu \approx 4\pi \int_{r_{\nu,\rm therm}}^\infty j_\nu 4\pi r^2 dr$. Substituting the scalings above, we find[46]

$$L_\nu \approx \frac{(4\pi)^2}{2n-3} j_\nu(r_{\nu,\rm therm}) r_{\nu,\rm therm}^3 \propto r_{\nu,\rm therm}^{3-2n} \propto \nu^{\frac{4n-6}{3n-2}}. \quad (6)$$

For $n = 2$, we have $L_\nu \propto \nu^{1/2}$, in reasonable agreement with the results by Roth et al. (2016). For large n, this tends toward

---

[45] Aspherical ejecta may be supported by the early detection of time-variable optical polarization ($p \sim 0.3\%$–1%; Smith et al. 2018b). However, the nonthermal NIR component identified by Perley et al. (2019) could also explain this polarization, which is consistent with the claimed rise of the polarization into the red.

[46] A related analysis by Shussman et al. (2016) results in $L_\nu \propto \nu^{\frac{30n-16}{21n-8}}$ when converted to our notation, which has a similar behavior to our result for large n. In that work, rather than assuming that T_e levels off near the surface, the authors assume that $T_e \propto \tau^{1/4}$.

an asymptotic scaling $L_\nu \propto \nu^{4/3}$, which is similar to the measured slope of the optical continuum of AT 2018cow.

We conclude that in AT 2018cow optical continuum radiation is reprocessed in a layer with a steep density gradient $n \gg 1$. Our derivation also indicates that the spectral slope should be roughly independent of the luminosity of the engine, as is observed, as long as the high ionization state is maintained.

3.1.4. Spectral Line Formation

In AT 2018cow, no clear spectral lines are apparent at early times, which can be understood as the result of a high degree of ionization and the low contrast of broad spectral features with very large velocities $\sim 0.1c$. H and He lines with $v \sim 4000$ km s^{-1} emerge at $\delta t > 20$ days (Figure 2; see also Perley et al. 2019) with asymmetric line profiles in which the red wing extends farther than the blue wing. This spectral line shape emerges naturally in radiative transfer calculations of line formation in an optically thick, expanding atmosphere (Roth & Kasen 2018). The line photons must scatter several times before escaping, and in the process they do work on the gas and lose energy in proportion to the volume-integrated divergence of the radial velocity component. However, these calculations also predict a net blueshift for the centroid of the line, which is not observed in AT 2018cow. In AT 2018cow, emission lines possess redshifted centroids (Figure 2). The redshift of the line centroids is hard to accommodate in spherical models and points to asphericity in the ejecta of AT 2018cow. A potential geometry of the expanding ejecta that would be consistent with the observed redshifted line centroids is that of an equatorially dense reprocessing layer and a low-density polar region, where the projected area of the photosphere on the receding side is larger than that on the approaching side, due to the angle the observer makes with the equatorial plane. A schematic diagram of this geometry is shown in Figure 12.

3.2. Radio Emission at $\nu < 100$ GHz

The key observational results are (i) an optically thick spectrum with $F_\nu \propto \nu^2$ at $\nu < 100$ GHz at $t < 35$ days. The spectrum later develops an excess of emission at low frequencies, which was noted by Ho et al. (2019), and that makes the optically thick spectrum less steep, $F_\nu \propto \nu^{1.2}$. (ii) The spectral peak frequency cascades down with time. Differently from normal radio SNe, the spectral peak flux also markedly evolves with time, with $F_{\rm pk} \propto t^{-1.7 \pm 0.1}$ at $t > 80$ days. (iii) With $L_\nu \sim 4 \times 10^{27}$ erg s^{-1} Hz^{-1} at $\nu \sim 9$ GHz around $\delta t \sim 20$ days and a rising emission with time until $t \sim 100$ days, the radio emission from AT 2018cow is also markedly different from GRBs in the local universe and cosmological GRBs (Figure 8).

3.2.1. Radio Emission from External Shock Interaction

The observed radio emission from AT 2018cow in the first weeks ($F_\nu \propto \nu^2$ at $\nu < 100$ GHz; Figure 7) is consistent with being self-absorbed synchrotron radiation likely produced from an external shock generated as the ejecta interacts with a dense external medium, as observed in radio SNe (e.g., Soderberg et al. 2005, 2012). While we leave the detailed modeling of the broadband radio emission from AT 2018cow to a dedicated paper (D. L. Coppejans et al. 2018, in preparation), here we

present basic inferences on the physical properties of its radio-emitting material obtained by adopting the standard modeling of self-absorbed synchrotron emission in SNe by Chevalier (1998).

In the context of self-absorbed synchrotron emission from a freely expanding blast wave propagating into a wind medium, the observed peak luminosity $L_{\nu,\rm pk}$, spectral peak frequency $\nu_{\rm pk}$, and peak time $t_{\rm pk}$ directly constrain the environment density, blast wave velocity, magnetic field, and energy. Following Chevalier (1998) and Soderberg et al. (2005), in Figure 13 we show that the measured peak flux and peak frequency of the radio SEDs at $t \sim 80$–150 days (corresponding to $L_{\nu,\rm pk} \leqslant 4 \times 10^{28}$ erg s^{-1} Hz^{-1} and $\nu_{\rm pk} < 20$ GHz) imply a shock/outer ejecta velocity $v_{\rm sh} \sim 0.1c$ interacting with a dense medium with an effective $A \sim 10$–$100 A_\star$ (depending on $\epsilon_B = 0.1$–0.01). The corresponding wind density is

$$n_w = \frac{\rho_w}{m_p} = \frac{\dot{M}}{4\pi v_w r^2 m_p} \approx 9 \times 10^6 \,{\rm cm}^{-3} \left(\frac{A}{100 A_\star} \right) v_{0.1}^{-2} t_{\rm wk}^{-2}, \tag{7}$$

where we have taken $r = vt$ as the shock radius, $v_{0.1} \equiv v_{\rm sh}/0.1c$, $t_{\rm wk} \equiv t/{\rm week}$. For these parameters, the equipartition energy (which is a lower limit to the kinetic energy of radio-emitting material) is $E_{\rm eq} \sim 2 \times 10^{48}$ erg and the magnetic field decreases from ~ 1 G to ~ 0.4 G from $t \sim 80$ days to 150 days. From the radio SED around 20 days presented in Ho et al. (2019; point with the highest luminosity in Figure 13), we infer a similar shock velocity of $v_{\rm sh} \sim 0.1c$, indicating limited deceleration of the blast wave into the environment.

Shock velocities $\sim 0.1\,c$ are common among normal stripped-envelope radio SNe (Figure 13). The values $A \sim 10$–$100 A_\star$ needed to explain the luminosity of the radio emission of AT 2018cow are similar to those inferred in previous radio-bright SNe (e.g., SN 2003L; Chevalier & Fransson 2006), but substantially smaller than the values $A \sim 10^5 A_\star$ needed on smaller radial scales to explain the early optical peak if the latter is powered by shock breakout from a wind (Equations (4), (5)). The velocity of the fastest ejecta inferred from the radio $\sim 0.1c$ is consistent with that needed to explain the rapid optical rise time (Equation (1)).

We can further constrain the environment density using the lack of evidence for a low-frequency cutoff in the radio spectrum (Figure 7) due to free–free absorption (e.g., Weiler et al. 2002), as follows. The optical depth of the forward shock to Thomson scattering and free–free absorption is given, respectively, by

$$\tau_{\rm T} \simeq \frac{\dot{M} \kappa_{\rm es}}{4\pi v_w r} \approx 0.01 \left(\frac{A}{100 A_\star} \right) v_{0.1}^{-1} t_{\rm wk}^{-1}, \tag{8}$$

$$\tau_{\rm ff} \simeq \frac{\alpha_{\rm ff} r}{3} \approx 10 \left(\frac{\nu}{1\,{\rm GHz}} \right)^{-2} \left(\frac{T_{\rm g}}{10^6\,{\rm K}} \right)^{-3/2} \left(\frac{A}{100 A_\star} \right)^2 v_{0.1}^{-3} t_{\rm wk}^{-3}, \tag{9}$$

where we have taken $\kappa_{\rm es} = 0.38$ cm^2 g^{-1} for fully ionized solar-composition ejecta and $\alpha_{\rm ff} \approx 0.03 n_w^2 \nu^{-2} T_{\rm g}^{-3/2}$ cm^{-1} as the free–free absorption coefficient, where $T_{\rm g}$ is the temperature of the gas, normalized to a value $T_{\rm g} \gtrsim 10^6$ K, following the argument by Ho et al. (2019).
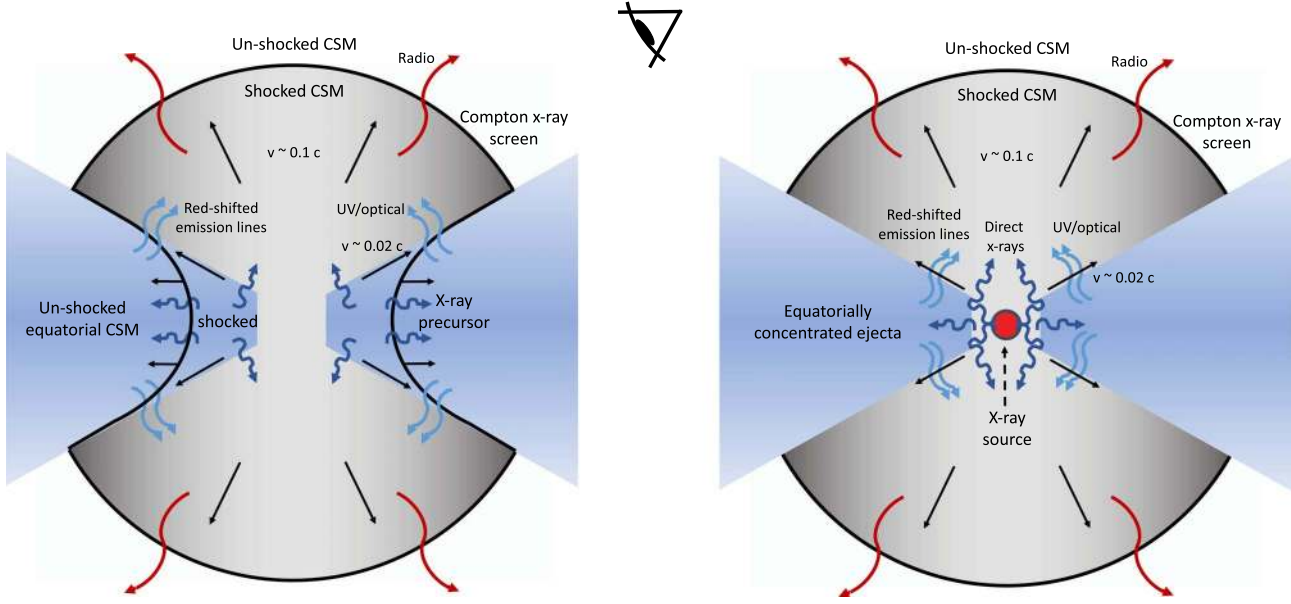
Figure 12. A shock-driven (left panel) or compact-object driven (right panel) origin of the emission from AT 2018cow. Left panel: the source of radiative energy is the interaction between the AT 2018cow ejecta and the CSM, consisting of a dense equatorial disk and less dense polar regions. Optical/UV emission at early times is primarily from the cooling of the fastest moving polar ejecta $v \sim 0.1c$, which shocks the CSM, leading to radio emission. The ejecta also drive a slower shock in the denser equatorial material, which leads to X-ray emission. For some lines of sight, the optical depth is large enough to modify the intrinsic spectrum and produce the hard X-ray energy "hump." The equatorial shock also launches a radial outflow with $v \sim 0.02c$ that wraps around the disk. After $\sim$20 days, the optical/UV emission in AT 2018cow is powered by the reprocessing of precursor X-rays that penetrate ahead of the equatorial shock into the disk. The optical photosphere at this time is located within the $v \sim 0.02c$ outflow. This transition from a situation where the photosphere resides in the fast polar matter at $\delta t < 20$ days (and a large fraction of X-rays are reprocessed) to one in which we are directly seeing the inner shell/disk at $\delta t > 20$ days is what causes the simultaneous change of the X-ray and optical properties of AT 2018cow. The radio emission is unaffected as it originates from the external shock. Our viewing angle presents us with a large emitting area from the receding side of the disk outflow and a limited view of the approaching side, leading to redshifted line peaks. Right panel: the central energy source of X-rays is a compact object (e.g., a magnetar or accreting black hole). The X-rays are emitted by the engine and then scatter off the inner funnel walls toward the observer.

From Figure 7, the optically thick part of the radio spectrum, which scales as $F_\nu \propto \nu^2$, without any evidence for free–free absorption, demands $\tau_{\rm ff}(15\,{\rm GHz}) \ll 1$ at $t = 6.5$ days and $\tau_{\rm ff}(5\,{\rm GHz}) \ll 1$ at $t = 12$ days. These limits translate into similar upper limits on the environment density:

$$\frac{A}{A_\star} < 1000 v_{0.1}^{3/2} \left(\frac{T_g}{10^6\,{\rm K}}\right)^{3/4}, \qquad (10)$$

consistent with the values $A \sim 10$–$100 A_\star$ for $v_{\rm sh} \sim 0.1c$ (Figure 13).

We conclude with considerations of the shock microphysics parameters and the properties of the distribution of electrons responsible for the radio emission. The radio emission is produced by relativistic electrons accelerated into a power-law distribution at the forward shock, e.g., $dN/d\gamma_e \propto \gamma_e^{-p}$ with $p \geqslant 2$. The Lorentz factor $\gamma_e = \gamma_\nu$ of the electrons which contribute at the radio frequency $\nu = 0.3(eB\gamma_e^2/2\pi m_e c)$ is

$$\gamma_\nu \simeq 4.6 \left(\frac{m_e c \nu}{eB}\right)^{1/2}$$

$$\approx 153 \epsilon_{\rm B,-2}^{-1/4} \, t_{\rm wk}^{1/2} \left(\frac{\nu}{100\,{\rm GHz}}\right)^{1/2} \left(\frac{A}{100 A_\star}\right)^{-1/4}, \qquad (11)$$

where we have estimated the magnetic field behind the shock to be

$$B_{\rm sh} = (6\pi \epsilon_B \rho_{\rm w} v_{\rm sh}^2)^{1/2} \approx 5.1\,{\rm G}\, \epsilon_{\rm B,-2}^{1/2} \, t_{\rm wk}^{-1} \left(\frac{A}{100 A_\star}\right)^{1/2}. \qquad (12)$$

From Figure 13, for $\epsilon_B \ll 0.01$, we would require larger values $A \gtrsim 100 A_\star$, incompatible with the observed lack of free–free absorption (Equation (10)).

As shown in Section 3.3.1, electrons with $\gamma_e \sim \gamma_\nu$ responsible for the optically thin radio emission $\nu \gtrsim \nu_{\rm sa}$ cool rapidly due to inverse-Compton (IC) emission in the optical/UV radiation of AT 2018cow. Therefore, above $\nu \gtrsim \nu_{\rm sa}$, the fast-cooling scaling holds (e.g., Granot & Sari 2002):

$$F_\nu = \nu^{-p/2} \underset{p=2-3}{\approx} \nu^{-1} - \nu^{-1.5}. \qquad (13)$$

Our radio SEDs at $t > 80$ days, with $F_\nu \propto \nu^{-1.4\pm0.1}$ above ν_{sa} confirms this inference (Figure 7). The predicted luminosity in the optical/NIR band ($\nu \gtrsim 10^{14}\,{\rm Hz} \gg \nu_{\rm sa}$) is thus similar to, or smaller than, the radio luminosity $\nu L_\nu \sim$ a few $\times 10^{40}\,{\rm erg\,s^{-1}}$ and thus is insufficient to explain the possible non-thermal NIR excess of luminosity $\sim 10^{42}\,{\rm erg\,s^{-1}}$ identified by Perley et al. (2019). Any non-thermal component in the IR/optical range cannot be from the same synchrotron source as the forward shock that produces the radio emission at $\nu < 100\,{\rm GHz}$.

The radio emission at $\nu > 100\,{\rm GHz}$ reported at early times is also more luminous than predicted by our model (Figure 7). This observation might suggest that the very early radio data at $\nu > 300\,{\rm GHz}$ might be dominated by a separate emission component (e.g., reverse shock) if it is physically associated with AT 2018cow (Figure 7).

3.2.2. Constraints on Off-axis Relativistic Jets

The observed radio emission is consistent with arising from non-relativistic ejecta with velocity similar to that of normal SNe

($v_{\rm sh} \sim 0.1c$) interacting with dense CSM with $A \sim 10$–$100A_\star$. No high-energy prompt emission was detected in association with AT 2018cow (Section 2.7). However, AT 2018cow showed evidence for broad spectral features in the optical emission, with velocities comparable to and even larger than those seen in broad-lined SNe Ic associated with GRBs (Modjaz et al. 2016, Figure 2). In this section, we constrain the properties of an off-axis jet in AT 2018cow. Emission from a collimated outflow originally pointed away from our line of sight becomes detectable as the blast wave decelerates into the environment and relativistic beaming of the radiation becomes less severe with time (e.g., Granot et al. 2002).

The observed radio emission from an off-axis jet primarily depends on the jet-opening angle (θ_j), off-axis angle ($\theta_{\rm obs}$), jet isotropic equivalent kinetic energy ($E_{\rm k,iso}$), environment density (parametrized as n and $\dot{M}$ for an ISM and wind-like medium, respectively), and shock microphysical parameters (ϵ_B, ϵ_e). We employ realistic simulations of relativistic jets propagating into an ISM and wind-like medium to capture the effects of lateral jet spreading with time, finite jet-opening angle, and transition into the non-relativistic regime. We ran the code BOXFIT (v2; van Eerten et al. 2010, 2012) at 1.4 GHz, 9 GHz, 15 GHz, and 34 GHz for a range of representative parameters of long GRB jets ($E_{\rm k,iso} = 10^{50} - 10^{55}$ erg, $\epsilon_B = 10^{-4} - 10^{-2}$, $\epsilon_e = 0.1$) and environment densities ($n = 10^{-3} - 10^{2}$ cm^{-3}, $\dot{M} = 10^{-8} - 10^{-3} M_\odot$ yr^{-1}). We use $p = 2.5$ and explore the parameter space for two jets of $\theta_j = 5°$ and $\theta_j = 30°$, representative of strongly collimated and less collimated outflows, respectively (as found for normal GRBs and low-energy GRBs; e.g., Racusin et al. 2009; Margutti et al. 2013b; Ryan et al. 2015).

With reference to Figure 14, we find that less collimated outflows with $\theta_j = 30°$ are ruled out in the ISM case for large densities $n > 1$ cm^{-3}. For a wind-type medium with $\dot{M}_w \sim 10^{-3} - 10^{-4} M_\odot$ yr^{-1}, consistent with the values $A \sim 10$–$100A_\star$ inferred for the forward shock radio emission, jets with $E_{\rm k,iso} \geqslant 10^{52}$ erg are presently ruled out for $\epsilon_e = 0.1$, $\epsilon_B = 0.01$, and jet-opening angles $\theta_j \approx 5°$–$30°$, corresponding to beaming-corrected jet energies $E_k \geqslant 4 \times 10^{49}$ erg (for $\theta_j = 5°$) or $E_k \geqslant 10^{51}$ erg (for $\theta_j = 30°$). Successful jets with $E_j < 4 \times 10^{49}$ erg ($\theta_j = 5°$) and $E_j < 10^{51}$ erg ($\theta_j = 30°$) propagating into a wind medium with $\dot{M} < 10^{-4} M_\odot$ yr^{-1} are allowed.

3.3. Hard and Soft X-Ray Emission

The key observational results are as follows: (i) luminous X-ray emission discovered at the level of $L_X \sim 10^{43}$ erg s^{-1}. L_x is significantly larger than seen in normal SNe and is similar to the values seen in GRBs in the local universe (Figure 5). (ii) Persistent X-ray flaring with short variability timescales of a few days superimposed on a secular decay, which is initially gradual $\propto t^{-1}$ but then steepens around $\delta t \sim 25$ days to a faster decay $\propto t^{-4}$ around the same time as the appearance of narrow optical features. (iii) Presence of two X-ray components of emission with distinct temporal evolution and spectral properties: a persistent source in the >0.1 keV range, as well as a transient component of hard X-ray emission at energies >10 keV detected at $\delta t \sim 8$ days and which disappears by $\delta t \sim 17$ days (Figure 6). (iv) The persistent X-ray spectral component of the emission is well modeled by $F_\nu \propto \nu^{-\beta}$ with $\beta \sim 0.5$ with no evidence for intrinsic neutral hydrogen absorption (Figure 4).
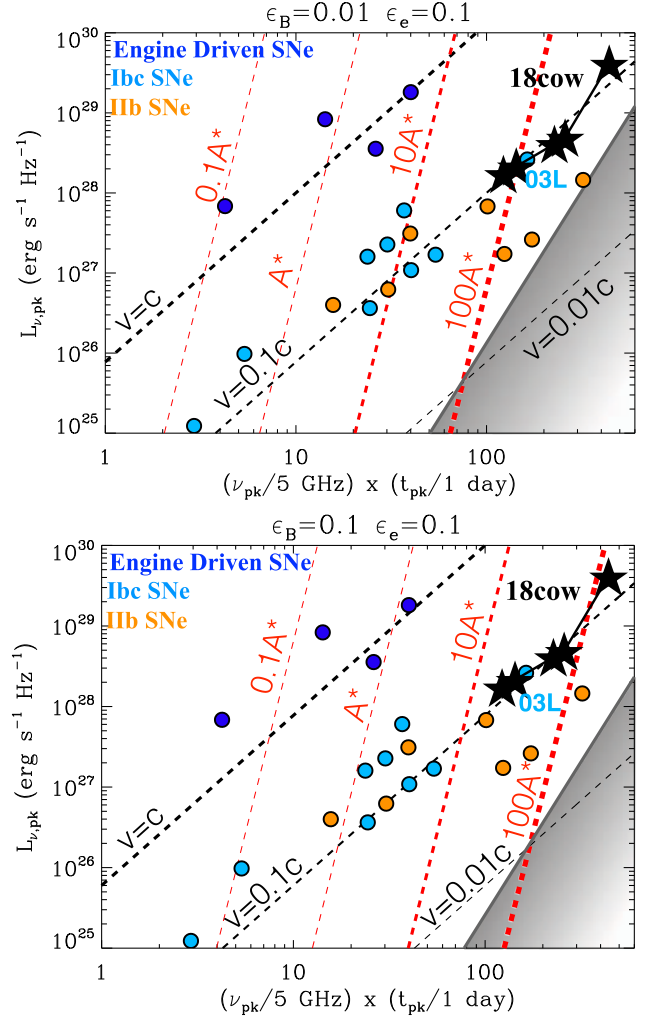

Figure 13. Phase space of radio observables: peak radio luminosity ($L_{\nu,{\rm pk}}$), peak spectral frequency ($\nu_{\rm pk}$), and peak time ($t_{\rm pk}$). Black (red) dashed lines: lines of constant shock velocity (constant mass-loss rate) following the standard formulation of synchrotron self-absorbed radio emission from a freely expanding blast wave in a wind-like environment (e.g., Chevalier 1998; Soderberg et al. 2005, 2012). Black stars: AT 2018cow at $t > 20$ days, for the epochs for which the peak of the SED is well constrained (Figure 7). The data point with the highest $L_{\nu,{\rm pk}}$ is from Ho et al. (2019). Gray area: region of the parameter space ruled out based on the lack of evidence for free–free absorption (Section 3.2.1, Equation (10)). In both panels, we assume $\epsilon_e = 0.1$. The upper (lower) panel is for $\epsilon_B = 0.1$ ($\epsilon_B = 0.01$). Blue, light-blue, and orange filled circles mark the position of the engine-driven SN with relativistic ejecta (i.e., GRBs and relativistic SNe), normal H-stripped core-collapse SNe, and type IIb SNe, respectively, from Soderberg et al. (2012).

Below we discuss the physical origin of the X-ray emission associated with AT 2018cow.

3.3.1. X-Ray Emission from External Shock Interaction

We first consider the possibility that the X-rays originate from the same forward shock responsible for the radio synchrotron emission (Section 3.2.1). The kinetic luminosity of the radio-emitting forward shock,

$$L_{\rm sh} = 4\pi r^2 \frac{9}{32} v_{\rm sh}^3 \rho_w \approx 5 \times 10^{42} \ {\rm erg \ s^{-1}} v_{0.1}^3 \left(\frac{A}{100A_\star} \right), \quad (14)$$

is close to the X-ray luminosity of AT 2018cow (Figure 4). This suggests a picture in which the X-rays are IC emission from optical/UV photons upscattered by relativistic electrons accelerated at the forward shock. Further supporting this scenario, the radio-to-X-ray luminosity ratio $\nu_{sa} L_{\nu_{sa}}/L_X \sim 0.02$ is comparable to the ratio of the magnetic energy density $U_B = B_{sh}^2/8\pi$ (Equation (12)) to the optical/UV photon energy density $U_\gamma = L_{opt}/(4\pi c r_{sh}^2)$, where $r_{sh} = v_{sh}t$,

$$\frac{U_B}{U_\gamma} \simeq 0.02\epsilon_{B,-2}v_{0.1}^2 t_{wk}^2 \left(\frac{A}{100A_\star}\right), \quad (15)$$

where $L_{opt} = 8 \times 10^{43} t_{wk}^{-2}$ erg s^{-1}.

However, the IC forward shock model cannot naturally explain the $F_\nu \propto \nu^{-0.5}$ spectrum of the persistent X-ray component, offers no consistent explanation of the transient hard X-ray component, and has difficulties accounting for the observed short-timescale variability, as we detail below.

Electrons heated or accelerated at the shock cool in the optical radiation field on the expansion timescale for electron Lorentz factors above the critical value,

$$\gamma_c \simeq \frac{3m_e c}{4\sigma_T U_\gamma t} = \frac{3\pi r^2 m_e c^2}{\sigma_T L_{opt} t}\bigg|_{r=vt} \approx 1.0 v_{0.1}^2 t_{wk}^3, \quad (16)$$

where $\sigma_T \simeq 6.6 \times 10^{-25}$ cm^2 is the Thomson cross-section. The electrons responsible for upscattering optical/UV seed photons of energy $\epsilon_{opt} \simeq 3kT_{opt} = 5\text{eV}(T_{opt}/2 \times 10^4\text{K})$ eV to X-ray energy $E_X = (4/3)\epsilon_{opt}\gamma_X^2$ must possess Lorentz factors

$$\gamma_X \approx \left(\frac{3E_X}{4\epsilon_{opt}}\right)^{1/2} \approx 12\left(\frac{E_X}{1\text{ keV}}\right)^{1/2}. \quad (17)$$

The values $\gamma_X \approx 6\text{–}40$ needed to populate the XRT bandpass 0.3–10 keV, though lower than those producing the millimeter radio emission (Equation (11)), are in the fast-cooling regime $\gtrsim \gamma_c$ for the first few weeks of evolution. Thus, while for slow-cooling electrons the observed $F_\nu \propto \nu^{-0.5}$ spectrum would match the expectation $F_\nu \propto \nu^{-(p-1)/2} \approx \nu^{-0.5} - \nu^{-1}$ for $p = 2\text{–}3$, it is incompatible with the fast-cooling expectation, $F_\nu \propto \nu^{-p/2}$, which gives a much softer spectrum than observed, $F_\nu \approx \nu^{-1} - \nu^{-1.5}$, for $p = 2\text{–}3$.

We now consider an IC origin of the transient hard X-ray component of emission, which shows a rising slope of $F_\nu \propto \nu^{0.5}$ (Figure 6). This emission is too hard to be free–free or synchrotron radiation (it violates the "synchrotron death line"; e.g., Rybicki & Lightman 1979), possibly hinting at an IC origin. In addition to accelerating electrons into a non-thermal distribution, the forward shock is also predicted to heat electrons (Sironi et al. 2015), generating a relativistic Maxwellian particle distribution with a mean thermal Lorentz factor,

$$\gamma_{th} \approx f_e \frac{m_p}{2m_e}\left(\frac{v_{sh}}{c}\right)^2 \approx 4.6(f_e/0.5)v_{0.1}^2, \quad (18)$$

where $f_e = 0.5$ is the fraction of the shock energy imparted to the electrons.[47] Thus, it may be tempting to associate the transient hard X-ray "bump" with IC emission by a relativistic

---

[47] Further Coulomb heating of the electrons by ions downstream of the shock (e.g., Katz et al. 2011) is inefficient given the low densities of the forward shock.
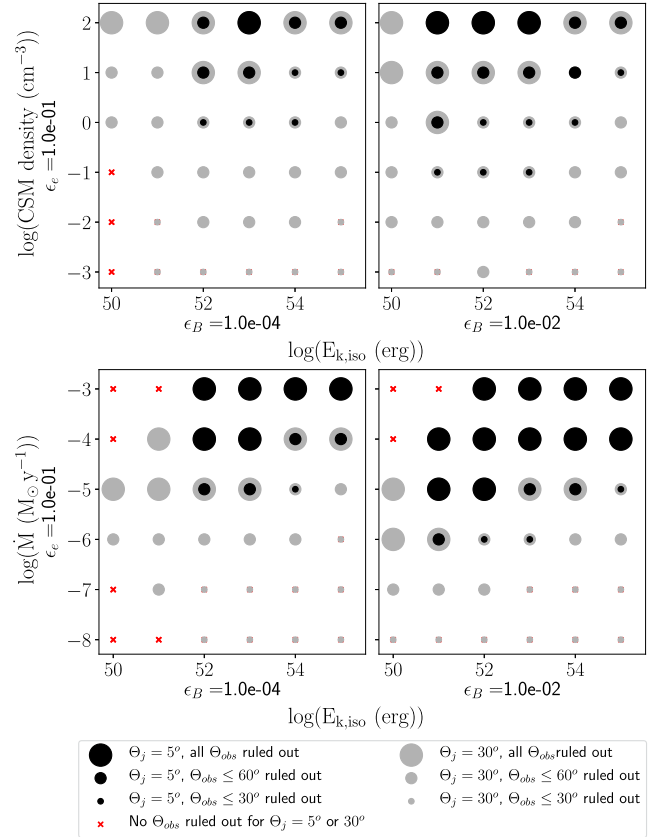

Figure 14. Constraints on off-axis relativistic jets in AT 2018cow, for a range of microphysical parameters (ϵ_e and ϵ_B), jet-opening angles θ_j, off-axis angle θ_{obs}, jet isotropic equivalent kinetic energies $E_{k,iso}$, and environment densities. Upper (lower) panel: ISM (wind) environment. We assume a wind velocity $v_w = 1000$ km s^{-1} (i.e., $\dot{M} = 10^{-5} M_\odot$ yr^{-1} corresponds to $A = A_*$).

Maxwellian distribution of electrons. However, the expected spectral peak would occur at an energy

$$E_{X,th} = \frac{4}{3}\gamma_{th}^2 \epsilon_{opt} \approx 0.14(f_e/0.5)v_{0.1}^2\left(\frac{T_{opt}}{2 \times 10^4 \text{ K}}\right)\text{keV}, \quad (19)$$

which is a factor of $\lesssim 100$ smaller than the observed peak $E_X \approx 50$ keV.

A final problem of the forward shock model is the rapid and persistent X-ray variability, which in this model has to be attributed to density inhomogeneities in the environment (e.g., a series of thin shells or "clumps"). The shortest allowed variability time Δt if the ejecta cover a large fraction of the solid angle is the light-crossing time, which for a shock of radius $r_{sh} = v_{sh}t$ with $v_{sh} \approx 0.1\text{–}0.2c$ (Section 3.2.1) is constrained to obey

$$\frac{\Delta t}{t} \gtrsim \frac{r_{sh}}{ct} \sim \frac{v_{sh}}{c} \approx 0.1\text{–}0.2. \quad (20)$$

We measure the properties of the X-ray flares in AT 2018cow following the same procedure as is used for long GRBs, adopting a Norris et al. (2005) profile. We find that the X-ray flares in AT 2018cow show much faster variability and violate this expectation, and furthermore show no evidence for a linear increase of their duration as the blast wave expands, contrary to expectations (Figure 15). Instead, our analysis in Section 2.9 suggests the presence of a dominant timescale of variability of

a few days. In Figure 15, we show that the X-ray variability observed in AT 2018cow is also not consistent with the expectations from density fluctuations encountered by a relativistic jet (with an observation either on axis or off axis). Differently from Rivera Sandoval et al. (2018), we thus conclude that density fluctuations in the CSM environment of AT 2018cow are unlikely to be the physical cause of the observed X-ray variability. The very rapid turnoff of the X-ray emission as $L_X \propto t^{-4}$ at $\delta t > 20$ days (Figure 4) is also difficult to accommodate in models where the X-ray emission is powered by an external shock (the typical L_X decline is $\propto t^{-1}$ for a spherical blast wave and $\propto t^{-2}$ for a collimated outflow after "jet break," e.g., Granot & Sari 2002).[48]

3.3.2. X-Rays from a Central Hard X-Ray Source

We consider an alternative scenario in which the observed X-rays originate primarily from an internal hard radiation source (either in the form of shocks or a compact object; Figure 12), embedded within an aspherical, potentially bipolar ejecta shell. The asphericity of the ejecta is a key requirement to explain the observed X-ray properties. The high-density material at lower latitudes (blue region in Figure 12) is opaque to X-rays below $\sim$15 keV due to bound–free absorption. The observed X-rays in this energy range either escape directly through the highly ionized low-density polar ejecta (lighter gray shaded region in Figure 12) and/or are scattered into the line of sight by this material. The X-rays absorbed by the dense equatorial shell are reprocessed to lower frequencies and are powering the optical light curve. The polar cavity is initially narrow and grows with time as the ejecta dilutes, expands, and becomes progressively transparent.

This scenario provides a natural explanation of the transient hard X-ray spectral component of Figure 6 created by the combined effect of photoelectric absorption at soft X-ray energies $\lesssim$10 keV and Compton-downscattering of very hard X-rays at $>$50–100 keV. Here we assume transmission and reflection through neutral gas, and leave the discussion of Fe-line formation to the next section. The power-law spectrum that dominates at soft X-ray energies $E < 10$ keV is instead produced by X-ray photons that reach the observer without being absorbed or Compton-downscattered (i.e., these photons provide a direct view of the central engine). At high energies, the spectral shape of the observed spectrum is controlled by the Thomson optical depth along our line of sight τ_T. At early times, close to the optical peak at $t_{pk} \sim t_{diff} \approx 3$ days (Equation (1)), $\tau_T \sim (c/v_{ej})(\kappa_{es}/\kappa) \sim 20$–40, where $v_{ej} \sim$ 0.1–0.2c and $\kappa_{es} \sim 4\kappa$. At this time, nearly all of the UV/ X-ray radiation of the central X-ray source is absorbed by the shell and reprocessed into optical/UV radiation. However, as the ejecta expands with time, its optical depth decreases $\tau_T \propto t^{-2}$, reducing the fraction of the central X-rays being absorbed. At the time of our first NuSTAR/INTEGRAL observations at $\delta t \sim 8$ days, $\tau_T \sim 3$, resulting in moderate downscattering and attenuation of radiation at $E \gtrsim 511$ keV/ $\tau_T^2 \sim 50$ keV (Figure 6). For the same parameters, we calculate $\tau_T \lesssim 1$ at $\delta t \sim 17$ days, by which time Compton-down-scattering plays a negligible role. This prediction is consistent

with our observation of an uninterrupted power-law spectrum extending from 0.3 keV to $\sim$70 keV at $\delta t \geqslant 17$ days (Figure 6).

The observed soft X-ray spectral shape is controlled by the bound–free optical depth τ_{bf}. Most opacity in the keV range is the result of photoelectric absorption by CNO elements, particularly the usually abundant oxygen. The bound–free opacity of oxygen is

$$\kappa_{bf} = \frac{f_n X_O \sigma_{bf}}{16 m_p}, \qquad (21)$$

where X_O is the oxygen mass fraction, f_n is its neutral fraction, and

$$\sigma_{bf} = \sigma_{th}(\nu/\nu_{th})^{-3}, \; \nu \gtrsim \nu_{th}, \qquad (22)$$

where for K-shell electrons of oxygen we have $\sigma_{th} = (2$–$1) \times 10^{-19}$ cm^{-2} and $h\nu_{th} = 0.74$–0.87 keV. Following Metzger (2017), the neutral fraction in an ejecta shell of mass M_{ej} and radius $R_{ej} = v_{ej}t$ due to photoionization by X-ray luminosity $L_X \approx \nu_{th} L_{\nu_{th}}$ is

$$f_n \approx \frac{\alpha_{rec} M_{ej} h\nu_{th}}{m_p L_X v_{ej} t \sigma_{th}} \approx \frac{4\pi \alpha_{rec} \tau_T (v_{ej}t) h\nu_{th}}{m_p L_X \sigma_{th} \kappa_{es}}, \qquad (23)$$

where for K-shells of oxygen $\alpha_{rec} \approx 10^{-12}$ cm^3 s^{-1} (Nahar & Pradhan 1997) for temperatures $\sim$10^6 K characteristic of the X-ray photoheated gas (Ho et al. 2019). The X-ray optical depth at $\nu_{th} \sim 1$ keV is thus

$$\tau_{bf} = \tau_T \frac{\kappa_{bf}}{\kappa_{es}} \sim \frac{\pi}{4} \frac{\alpha_{rec}}{\kappa_{es}^2} \frac{\tau_T^2 X_O}{m_p^2} \frac{h\nu_{th}}{L_X} v_{ej} t$$

$$\sim 0.01 \left(\frac{X_O}{0.01}\right) \tau_T^2 \left(\frac{t}{1 \text{ week}}\right) \nu_{0.1} \left(\frac{L_{keV}}{10^{43} \text{ erg s}^{-1}}\right)^{-1}. \qquad (24)$$

For ejecta with an oxygen abundance close to solar abundance ($X_O \sim 0.01$), $\sim$keV X-rays of luminosity $\sim$10^{43} erg s^{-1} ionize the ejecta sufficiently to escape unattenuated on timescales of a couple weeks when the Thomson column along the low-density polar region is also low $\tau_T \lesssim 1$. However, at earlier times, we expect $\tau_{bf} \gtrsim 1$ when τ_T is larger, i.e., around the time of the NuSTAR/INTEGRAL spectral "hump" (Figure 6).

We quantitatively explore the predictions of our model by performing a series of Monte Carlo calculations where we follow the escape of photons as they propagate through a uniform shell of radius R_{sh} and thickness $2R_{sh}$ with a polar cavity of opening angle $\theta_{sh} = 30°$ carved into it. We assume an isotropic source with intrinsic spectrum $F_\nu \propto \nu^{-0.5}$ as observed and self-consistently account for photoelectric absorption and Compton-scattering. Figure 16 shows the results for the transmitted X-rays for different lines of sight θ_{obs} and optical depth τ_T. Polar observing angles (i.e., small θ_{obs}) receive a larger fraction of "direct" X-rays (including X-rays reflected off the cavity walls; Figure 12) at any τ_T, while more equatorial views with larger θ_{obs} are associated with more prominent "humps," as a larger fraction of X-rays intercepts absorbing/ scattering material. However, as τ_T drops with time as a result of the shell expansion, X-rays become detectable from a larger range of viewing angles while the "hump" moves to lower energies to eventually disappear.

In our model, (i) the X-ray variability is intrinsic to the central source, rather than being a consequence of inhomo-geneities in the external medium. (ii) The soft X-rays $\lesssim$10 keV,

---

[48] The hint of a correlation of the UV and X-ray variability of Section 2.9 also supports an "internal" origin of the X-ray emission.
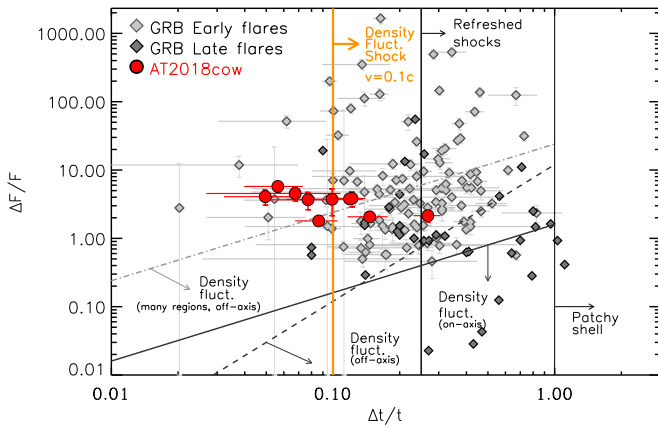
Figure 15. Flux contrast $\Delta F/F$ vs. relative variability $\Delta t/t$ for X-ray flares in AT 2018cow (red filled circles) and long GRB flares at early $t < 1000$ s and late times $t > 1000$ s (gray diamonds). Kinematically allowed regions of the parameter space in the context of relativistic collimated outflows are marked with black/gray solid, dashed, and dotted–dashed lines (details in Ioka et al. 2005). A slower shock with $v_{sh} \sim 0.1$–$0.2c$ like the one powering the radio emission in AT 2018cow is expected to produce $\Delta t/t \geqslant 0.1$–0.2 if the overdensity region covers a large fraction of the solid angle (orange line). Flares in AT 2018cow have been fitted using the same procedure as that used for long GRBs adopting a Norris et al. (2005) profile. The width of a flare Δt is measured at $1/e$ of the flare peak value. Variability in AT 2018cow violates the expectations from density fluctuations in relativistic jets and slower shocks. Long GRB flare data are from Chincarini et al. (2010), Margutti et al. (2010), and Bernardini et al. (2011).

which originate directly from the engine, may show more pronounced time variability than those associated with the transient hard X-ray spectral component, which instead are diffusing through an optically thick shell. (iii) The true luminosity evolution of the central source is the sum of the optical and X-ray luminosities (L_{engine} in Figure 9); the fact that the X-ray light curve decreases less rapidly at early times than the optical light curve, as shown in Figure 9, is a consequence of the increasing fraction of escaping X-ray radiation with time.

3.3.3. The Connection of AT 2018cow to Other Astrophysical Sources with Compton-hump Spectra

In the previous section, we provided a proof of concept that interaction (in the form of scattering and absorption) of X-ray photons from a source located within expanding ejecta with temporally declining optical depth τ provides a natural explanation of the broadband X-ray spectrum of AT 2018cow. The model is agnostic with regard to the physical nature of both the X-ray radiation and the reprocessing medium. The incident hard X-ray radiation in AT 2018cow might originate from an embedded shock, or from a central "nebula" (similar to a pulsar-wind nebula around a young magnetar), or an X-ray "corona" around an accreting BH.

Consistent with the picture above, reflection emission from the reprocessing of inverse-Compton photons off a thick accretion flow produces a "Compton-hump" feature similar in shape to what we observed in AT 2018cow. Such emission is typical of X-ray binaries (XRBs) and AGNs (e.g., Risaliti et al. 2013; Tomsick et al. 2014 for recent examples), where a high-energy power-law component associated with the Compton-upscattering of seed thermal photons from the BH accretion disk by a hot cloud of electrons—the "corona"—interacts with cold matter in the disk. Reflection emission is typified by a ~ 30 keV Compton hump along with prominent Fe $K\alpha$-band emission and Fe K-shell absorption edges (e.g., Figure 1 of
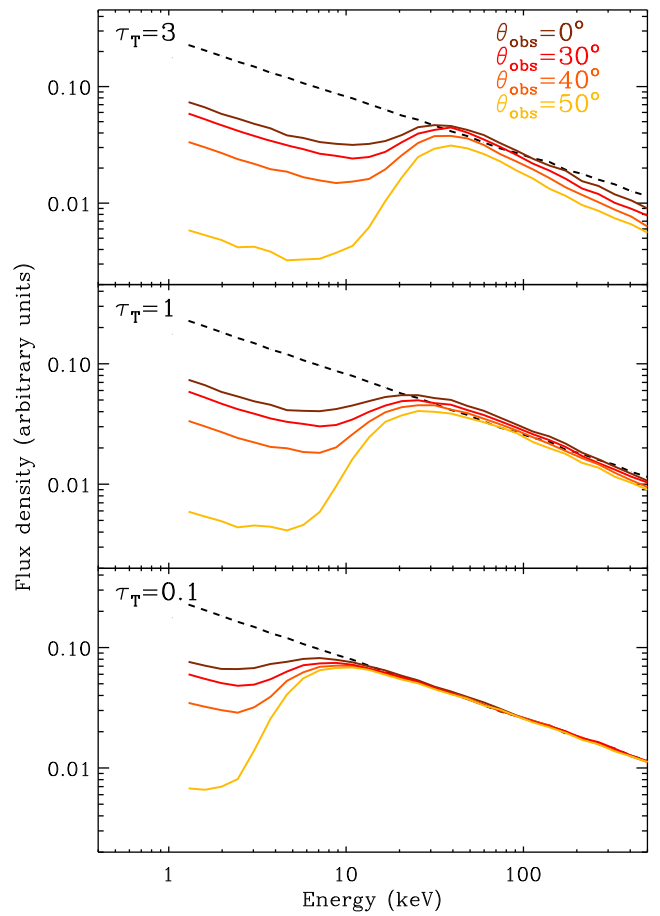

Figure 16. Transmitted X-ray spectrum from a central source with intrinsic spectrum $F_\nu \propto \nu^{-0.5}$ (black dashed line) for different viewing angles θ_{obs}. A shell of material of optical depth τ_T, radius R_{sh}, and thickness $2R_{sh}$ with a polar cavity of opening angle $\theta_{sh} = 30°$ surrounds the source (motivated by the geometry shown in Figure 12). At larger optical depths and intermediate viewing angles, the transmitted spectrum shows a "hump" of emission above ~ 10 keV that becomes less prominent and disappears at lower τ_T, as observed in AT 2018cow.

Reeves et al. 2004; Risaliti et al. 2013), which can all become broadened by relativistic effects. It is tempting to associate the transient excess of emission around ~ 8 keV detected in the first spectrum of AT 2018cow (Figure 6, inset) with a Fe K-shell spectral feature (emission/absorption). The ~ 8 keV excess of emission disappears by 16.5 days together with the hump, which supports the idea of a physical link between the two components and motivates our attempt below to model AT 2018cow with standard disk-reflection models. While the actual geometry of AT 2018cow is likely to be more complicated than in standard accretion disks (for AT 2018cow the reprocessing material might be rapidly expanding and diluting), the same physics of hard X-ray radiation reprocessing (including reflection and partial transmission) applies.

Fitting the broadband X-ray data of AT 2018cow at $\delta t = 7.7$ days with a Comptonized disk-reflection model via simpl (Steiner et al. 2009) acting on a thermal component and relxill (Dauser et al. 2014) produces a good fit to the data ($\chi^2/$d.o.f.~ 1.0), matching a $kT_e \geqslant 30$ keV corona, with reflection fraction $R_f \gtrsim 1$ (Figure 17).[49] The best-fitting model predicts a

---

[49] R_f is the ratio of Compton-scattered photons that illuminate the disk as compared to those reaching the observer.

moderate optical depth to the corona $\tau \sim 1$–2, which illuminates the walls of the reprocessing material in a funnel-like geometry. If sufficiently compact, the innermost corona may be Compton-thick, which would produce a thermal feature at the coronal temperature, partially accounting for the hard X-ray excess. In this model, the 7–9 keV excess is naturally explained as Fe–K fluorescence emission originating away from the core along the funnel, where the ionization parameter drops below $\log \xi \equiv L/nR^2 \lesssim 4$. In this model, the Fe–K feature is primarily distorted by the orbital and thermal motion of the gas to produce the observed broad blueshifted Fe–K emission. In this scenario, the observed disappearance of the hard X-ray Compton hump and associated Fe emission can be explained by either (i) a decline in the accretion rate, which makes the funnel opening angle grow. The corona is both less confined to a compact geometry and the walls of the funnel are extended, jointly resulting in less illumination and a diminished contribution from reflection. (ii) Or, if the hard excess is supplied somewhat by a Compton-thick coronal core with $kT_e \sim 30$ keV, then as $\dot{M}$ declines, the region becomes optically thin, causing the high-energy thermal feature to drastically fade.

Finally, we address the question of super-Eddington luminosity, which is of particular relevance if the $L_X \gtrsim 10^{43}$ erg s^{-1} in AT 2018cow is powered by a stellar-mass BH (discussed in Section 4.2). In the case of intermediate-mass BHs (IMBHs) discussed in Section 4.3, the required accretion rate would only be mildly super-Eddington. Theoretical studies of super-Eddington accretion flows have recently experienced a surge of interest thanks to the observational finding that numerous ultraluminous X-ray sources (ULXs), systems that are brighter than the Eddington limit of stellar-mass black holes, are in fact powered by pulsars (e.g., Walton et al. 2018a, 2018b). Theoretical models predict that highly super-Eddington accretion produces a funnel geometry in the central flow (Sądowski & Narayan 2015), not dissimilar from our model above. The emission is collimated and generally paired with powerful outflows, including radiatively powered jets (Sądowski & Narayan 2015). In these systems, the seed X-ray luminosity can be "boosted" by a factor of ~tens by scatterings by hot coronal electrons at $\tau \sim 1$–2. The underlying seed X-ray emission from the disk is then required to be $\sim 10^3 L_{\rm Edd}$ for a BH of a few $M_\odot$, in line with the observed super-Eddington emission in known NS ULXs.

3.4. The Excess of NIR Continuum Emission

Perley et al. (2019) identified an excess of NIR emission with respect to the UV/optical blackbody with $F_\nu \propto \nu^{-0.75}$, which they interpret as non-thermal synchrotron emission physically connected with the radio–millimeter emission at $\nu > 100$ GHz. Our observations confirm the presence of the NIR excess (Figure 11). As shown in Figure 11, the extrapolation of the model that best fits the radio observations at $\nu < 100$ GHz severely underpredicts the NIR flux. From theoretical arguments, we inferred in Section 3.2.1 that electrons radiating at >100 GHz must be fast cooling, which would predict a steeper radio-to-NIR spectral slope than what is needed to connect the radio to the NIR band on the same synchrotron SED. Extrapolating the X-ray component to the NIR frequency range produces the same result of under-predicting the observed NIR emission. We conclude that the NIR excess is unlikely to be directly related to the same

populations of electrons that produce the non-thermal radio emission at $\nu < 100$ GHz or the X-ray radiation.

Kuin et al. (2019) favored a different interpretation of the NIR excess as free–free emission from an expanding "atmosphere" with a shallow density gradient. The NIR-emitting material would be located at larger distances than that of the optical-/UV-emitting material. This process is well known to produce an NIR excess of emission in hot stars surrounded by dense winds and luminous blue variables (see, e.g., Wright & Barlow 1975) and has been invoked to explain the NIR excess in SN 2009ip (Margutti et al. 2014). In this scenario, the spectral slope is directly connected with the density gradient of the NIR-emitting material, and it is not expected to evolve with time, as observed, as long as the high ionization state is maintained. From Equation (6), the measured spectral slope $F_\nu \propto \nu^{-0.75}$ suggests a medium with a shallow density gradient of ionized material $\rho \propto r^{-n}$ with $n < 2$. In these conditions, matching the observed NIR luminosity requires large densities corresponding to an effective mass-loss rate $\gg 100A^*$, which is inconsistent with our findings from the radio data modeling (Section 3.2.1). More complicated geometries with a detached equatorial shell might provide a more consistent explanation. However, regardless of the geometry, this class of models does not naturally account for the NIR temporal variability reported by Perley et al. (2019).

An alternative model consists of a light echo (i.e., radiation reprocessed by a shell of material at some distance $R_{\rm shell}$). The NIR excess is already present in the first SED at ~3.4 days, as presented by Perley et al. (2019), which implies an upper limit to the location of the reprocessing shell through simple light-travel time arguments $R_{\rm shell} < 9 \times 10^{15}$ cm. Following Dwek (1983), we estimated that at these distances only large dust grains with radius $\geqslant 10\ \mu$m might have been able to survive the harsh environment created by the luminous and hot radiation from AT 2018cow, which makes the light-echo interpretation contrived.

We conclude that the observed NIR excess of emission is not directly related to the non-thermal X-ray and radio emission at $\nu < 100$ GHz and that an "extended atmosphere" or light-echo models are unlikely to offer a quantitative explanation of the observed phenomenology.

4. Interpretation: The Intrinsic Nature of AT 2018cow

In this section, we synthesize the previous discussion into a concordant picture to explain our multiwavelength data, and we speculate on the intrinsic nature of AT 2018cow within a "central X-ray source" hypothesis. Any model for the central X-ray source must at a minimum abide by the following constraints:

1. An "engine" that releases a total energy $E_e \sim 10^{50}$–$10^{51.5}$ ergs, over a characteristic timescale $\sim 10^3$–10^5 s, with a late-time luminosity decay $L_e \propto t^{-\alpha}$ with $\alpha \sim 2$–2.5. The engine has a relatively hard intrinsic X-ray spectrum $F_\nu \propto \nu^{-0.5}$ and is responsible for the highly variable X-ray emission (Figure 18).

2. Presence of relatively dense CSM material extending to radii $\gtrsim 10^{16}$ cm. Its radial profile is not well constrained, but the gaseous mass corresponds to that of an effective wind mass-loss parameter $A \sim 10$–$100\,A_\star$, similar to the CSM around luminous radio SNe (Figures 8 and 13). The timescale for a stellar progenitor to lose a mass
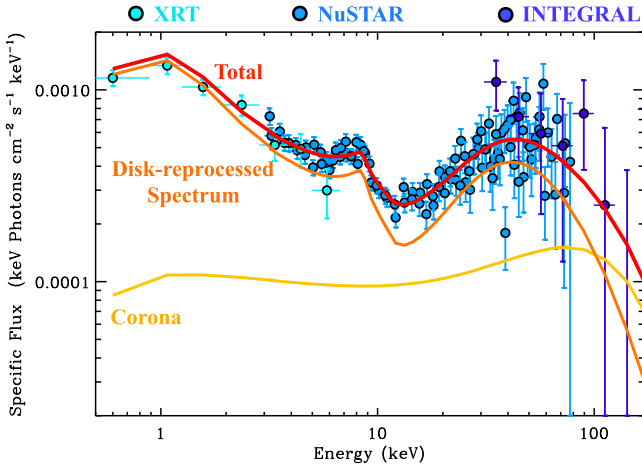
Figure 17. The broadband X-ray spectrum of AT 2018cow at $\delta t = 7.7$ days is well fitted by a Comptonized disk-reflection model. This model naturally accounts for the 6–9 keV excess as Fe K-band fluorescence emission distorted by the orbital and thermal motion of the gas. We note that the 6–9 keV excess shows evidence for substructure that is likely important to constrain the details of the physical conditions at play and that will be quantitatively explored in a future dedicated work.

comparable to the ejecta mass $\sim 1\,M_\odot$ for such parameters is only $\sim 10^3$–10^4 yr, necessitating a phase of stellar evolution that is short relative to the main-sequence lifetime.

3. Asymmetric distribution of material in the vicinity of AT 2018cow, with denser CSM/ejecta in the equatorial plane and less dense, fast-expanding ejecta along the polar direction.

4. Presence of hydrogen and helium in the ejecta.

5. Limited amounts of ^{56}Ni synthesized, $M_{\rm Ni} \lesssim 0.04\,M_\odot$.

6. Low ejecta mass ~ 0.1–$1\,M_\odot$ with a wide range of velocities, from the fastest $v_{\rm ej} \approx 0.1$–$0.2c$ (as needed to explain the early optical rise and radio emission) to the slowest $v_{\rm ej} \lesssim 0.02c$ (needed to explain the persistent optically thick photosphere and narrower late-time emission lines). This range of velocities may be attributed to the aspherical (e.g., bipolar) structure of the ejecta (Figure 12). A similar aspherical geometry is suggested by the shape of the optical emission lines (Figure 2) and by the emergent time-dependent spectrum of the central X-ray source (Figure 16).

7. For a medium with $A \sim 10$–$100\,A_\star$, jets viewed off-axis with $E_{\rm k,iso} \geqslant 10^{52}$ erg are ruled out for jet opening angles $\theta_{\rm j} \approx 5°$–$30°$ corresponding to beaming-corrected jet energies $E_{\rm k} \geqslant 4 \times 10^{49}$ erg (for $\theta_{\rm j} = 5°$) or $E_{\rm k} \geqslant 10^{51}$ erg (for $\theta_{\rm j} = 30°$; Figure 14). On-axis jets with $E_{\rm k,iso} \geqslant 10^{52}$ erg are ruled out for the entire range of environment densities considered, $\dot{M} \geqslant 10^{-8}\,M_\odot\,{\rm yr}^{-1}$, consistent with the non-detection of a prompt γ-ray signal by the IPN.

8. The engine model needs to be able to naturally accommodate the simultaneous transition between two phenomenologically distinct phases of evolution in the X-ray and optical bands, with the first phase characterized by featureless optical spectra and the presence of a hard X-ray spectral hump, and the second phase at $\delta t > 20$ days (when $L_{\rm X} \sim L_{\rm UVOIR}$), characterized by the emergence of H and He emission in the spectra and a

steeper X-ray decay with more pronounced variability. This transition could represent the photosphere radius receding from the fast polar ejecta to the slower equatorially concentrated reprocessing material, in the process at least partially exposing the central engine to our vantage point as high-latitude viewers.

9. Finally, any engine model needs to be naturally compatible with the location of AT 2018cow within a faint spiral arm of the star-forming dwarf spiral galaxy CGCG 137-068 (Figure 1; Perley et al. 2019).

Figure 12 illustrates the geometry of AT 2018cow in the context of engine-driven models, where the engine is in the form of either a deeply embedded internal shock (left panel) or a compact object (right panel). In the case of a deeply embedded internal shock, the denser equatorial material existed before the AT 2018cow event, while in the case of a compact-object central engine, the thick equatorial torus might have been created by AT 2018cow (i.e., is part of the AT 2018cow ejecta).

Potential engine models are summarized in Table 2. Some models, like NS–NS and WD–NS mergers, and stripped-envelope SNe, are immediately ruled out by the presence of H/He in the ejecta. Below we discuss the more promising possibilities, some of which were already considered by Prentice et al. (2018), Perley et al. (2019), and Kuin et al. (2019), though in some cases we reach different conclusions.

4.1. Millisecond Magnetar from a Successful Supernova with Low Ejecta Mass

One possibility is a core-collapse event with low ejecta mass giving birth to a rapidly spinning magnetar. The presence of hydrogen in the ejecta favors low-mass stellar progenitors that have been theoretically linked to electron-capture SNe (ecSNe; e.g., Miyaji et al. 1980; Nomoto et al. 1982), rather than an ultra-stripped massive star explosion (e.g., Tauris et al. 2015). ecSNe are expected to originate from progenitors with mass ~ 8–$10\,M_\odot$ and are predicted to have low explosion energy $E_{\rm k} \sim 10^{50}$ erg, small ^{56}Ni production ($\sim 10^{-3}\,M_\odot$), and ejecta mass of a few $M_\odot$. The low $M_{\rm Ni}$ and explosion $E_{\rm k}$ are consistent with our inferences for AT 2018cow, as most of the kinetic energy of the fast ejecta of AT 2018cow might have been provided by the engine (as opposed to the initial explosion). The larger $M_{\rm ej}$ of ecSN models can also be consistent with AT 2018cow, as our constraint $M_{\rm ej} < 0.3\,M_\odot$ from Section 3.1.1 applies to the fastest polar ejecta only. Special circumstances are, however, required to create the aspherical ejecta distribution of AT 2018cow and to produce a magnetar remnant. We speculate that the rapid rotation of the star, needed to endow the magnetar engine with its rapid rotation, or a jet/wind bubble (see below) could impart the ejecta with the needed equatorial–polar density asymmetry, and that these special requirements naturally explain why AT 2018cow-like transients are much rarer than 8–$10\,M_\odot$ progenitor stars in the nearby universe.

To explain the required engine energy $E_{\rm e} \gtrsim 10^{50}$–$10^{51.5}$ erg as rotational energy of the magnetar, its initial spin period should obey $P_0 \sim 3$–20 ms. The duration of the engine for an isolated magnetar is given by the dipole spin-down time (e.g., Spitkovsky 2006), which for a $1.4\,M_\odot$ NS is given by

$$t_{\rm e} = t_{\rm sd} \approx 1.4 \times 10^4\,{\rm s}\left(\frac{B_{\rm d}}{10^{15}\,{\rm G}}\right)^{-2}\left(\frac{P_0}{10\,{\rm ms}}\right)^2. \qquad (25)$$

Thus, to explain the engine timescale $t_e \sim 10^3$–10^5 s for $P_0 \sim 3$–20 ms, we require a magnetar with $B_{\rm d} \approx 10^{15}$ G, in
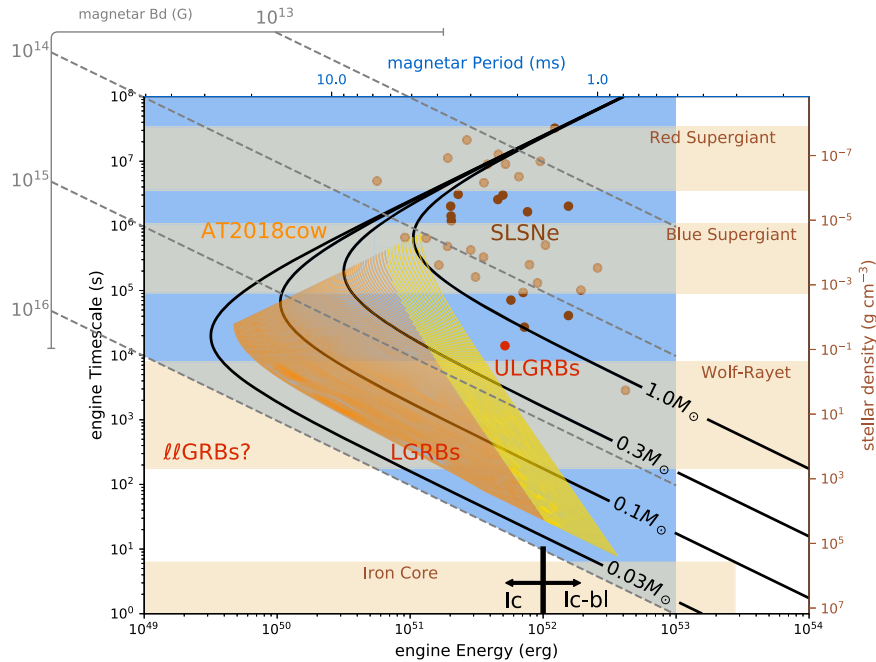
Figure 18. Parameter space of engine-powered transients showing the permissible region for AT 2018cow (orange and yellow) in comparison to SLSNe (brown circles) and long GRB engines (red circles, including ultralong GRBs—ULGRBs—and low-luminosity GRBs—llGRBs). Accommodating the rise time and peak luminosity of AT 2018cow requires an engine that deposits $E_e \sim 10^{50}$–10^{52} erg over a timescale of $t_e \sim 10^3$–10^5 s. The orange–yellow region spans the range of possible ejecta masses (marked by black curves) and initial explosion energies (different green lines). Highlighted in yellow is the parameter space where a jet with energy E_e would be able to successfully break out of the confining ejecta. The light-brown shaded regions mark several fallback progenitor model parameters, while the blue shaded region bounds the range of plausible magnetar parameters (engine energy $E_e \leqslant 10^{53}$ erg and dipole magnetic field $B_d < 10^{16}$ G). Adapted from Margalit et al. (2018).

agreement with the findings by Prentice et al. (2018). This strong B field is in the range of "magnetars" normally invoked as central engines of GRBs (Metzger et al. 2011), but larger than those inferred for SLSNe, which typically require $B_d \sim 10^{14}$ G (e.g., Kasen & Bildsten 2010; Inserra et al. 2013; Nicholl et al. 2017). Alternatively, the intrinsic dipole magnetic field of the magnetar could be weaker, but the effective spin-down rate could be enhanced due to fallback accretion from the progenitor star (Metzger et al. 2018); such a scenario predicts a spin-down luminosity $L_e \propto t^{-2.38}$, steeper than the usual $\propto t^{-2}$ for an isolated magnetar.

The source of the X-ray emission in this case is the "nebula" of hot plasma and magnetic fields inflated by the magnetar behind the expanding SN ejecta (e.g., Metzger & Piro 2014). Though the details of the nebular spectrum are uncertain, the inferred $F_\nu \propto \nu^{-0.5}$ would be consistent with synchrotron radiation.

It is natural to ask whether the same engine responsible for creating the nebula of luminous variable X-rays would also be expected to create a successful relativistic jet. Margalit et al. (2018) showed that the central engine jet can escape homologously expanding ejecta if the energy of the jet exceeds a critical value:

$$E_j \gtrsim 0.195 (\gamma_j/2)^{-4} E_{k,0} \sim 10^{49} - 10^{50}\ \mathrm{erg}, \qquad (26)$$

where $E_{k,0} \gtrsim 10^{51}$ erg is the initial kinetic energy of the explosion and γ_j is the jet Lorentz factor while propagating through the star (values of $\gamma_j \sim 2$–3 are required to produce jet opening angles similar to those of GRBs; Mizuta & Ioka 2013). Thus, if a modest fraction of the engine energy goes into a

collimated jet, a jet could break through the star on a timescale $\lesssim t_e \sim 10^3$–10^5 s prior to the optical peak.

Our prompt γ-ray search with the IPN in Section 2.7 led to no evidence for prompt bursts of γ-ray emission in AT 2018cow that might be associated with successful jets (in analogy with GRBs). Our analysis in Section 3.2.2 limits the allowed parameter space to successful jets with $E_{k,iso} < 10^{52}$ erg and $\epsilon_B < 0.01$ propagating into a medium with $\dot{M} < 10^{-4}\ M_\odot\ \mathrm{yr}^{-1}$, corresponding to $E_j < 4 \times 10^{49}$ erg ($\theta_j = 5°$) and $E_j < 10^{51}$ erg ($\theta_j = 30°$).

Regardless of whether a tightly collimated jet is created, a wider jet or wind bubble from the engine could impart the ejecta with the needed aspherical (e.g., bipolar) structure, even starting with spherical ejecta. During this process, the secondary shock driven through the ejecta on timescale $\ll t_e$ accelerates the outer layers of the ejecta to $v \sim 0.1$–$0.2c$ (e.g., Kasen et al. 2016; Blondin & Chevalier 2017; Suzuki & Maeda 2017), explaining the early optical rise and the non-thermal radio emission.

4.2. Failed Explosion of a Blue Supergiant Star

Another possibility is the core collapse of a massive star that initially fails to explode as a successful SN, instead creating a black hole remnant (e.g., Quataert & Kasen 2012; Dexter & Kasen 2013; Quataert et al. 2018). Blue supergiant stars have been recently invoked as progenitors of ultralong GRBs (e.g., Quataert & Kasen 2012; Gendre et al. 2013; Nakauchi et al. 2013; Wu et al. 2013; Liu et al. 2018; Perna et al. 2018; Quataert et al. 2018). Fernández et al. (2018) showed that the failed explosion of a blue supergiant star ($M_\star \approx 25\ M_\odot$; $R_\star \approx 70$–$150\ R_\odot$), originating from the neutrino-induced mass loss that follows the formation of the NS (Nadezhin 1980;

Table 2
Central X-Ray "Engine" Models for AT 2018cow

Model	Ejecta Mass/Velocity	Engine Timescale	CSM?	He?	H?	References
NS–NS Merger Magnetar	✗	✓	✗	✗	✗	1
WD–NS Merger	✓	✓	✗	✗	✗	2
IMBH TDE	✓	Maybe[a]	✗	✓	✓	3
Stripped-Envelope SN + Magnetar/BH	✓	✓	✓	Maybe	✗	4
Electron Capture SN + Magnetar	✓	✓	✓	✓	✓	5
Blue Supergiant Failed SN + BH	✓	✓	✓	✓	✓	6
SN + Embedded CSM Interaction	✓	✓	✓	✓	✓	7

Note.
[a] If circularization is efficient.

References. (1) Yu et al. (2013), Metzger & Piro (2014), (2) Margalit & Metzger (2016), (3) Chen & Shen (2018), (4) Tauris et al. (2015), (5) e.g., Miyaji et al. (1980), Nomoto et al. (1982), Moriya et al. (2014), and references therein, (6) Fernández et al. (2018); Quataert et al. (2018), (7) Andrews & Smith (2018), Metzger & Pejcha (2017).

Lovegrove & Woosley 2013; Piro 2013; Coughlin et al. 2018), results in the shock-driven ejection of ∼0.1 $M_\odot$ at a velocity $v \sim 0.02c$. The remaining star then accretes onto the newly formed black hole.

If the envelope of the remaining bound star has sufficient angular momentum, it will form an accretion disk around the newly formed BH, possibly producing the BH accreting scenario that well explains the broadband X-ray spectrum of Section 3.3.3. The disk will also produce wind ejecta that collides with the outflowing unbound shell, thermalizing its energy and accelerating it to a higher velocity $v_{ej} \sim 0.1c$ (e.g., Dexter & Kasen 2013). The timescale of the engine in this case is set by the gravitational freefall time of the outer layers of the blue supergiant progenitor onto the central black hole,

$$t_e \sim t_{ff} \approx \left(\frac{R_\star^3}{GM_\star}\right)^{1/2} \approx 1.3d \left(\frac{M_\star}{25M_\odot}\right)^{-1/2} \left(\frac{R_\star}{50R_\odot}\right)^{3/2}, \quad (27)$$

consistent with the constraints on the engine lifetime t_e. The engine luminosity in this scenario would be expected to decay as the fallback rate, $L_e \propto t^{-5/3}$ (however, see Tchekhovskoy & Giannios 2015).

We conclude by commenting on the rate of occurrence of AT 2018cow-like transients in the universe. In principle, it is possible to distinguish among the different progenitor paths based on the rate of transient events with similar properties (energetics, timescales, and environments). From the PanSTARRS sample, Drout et al. (2014) inferred an FBOT rate of 4%–7% for the core-collapse SN rate. However, although AT 2018cow shows blue featureless spectra at early times and a fast rise to peak similar to the PanSTARRS FBOTs, all of the PanSTARRS FBOTs are significantly less luminous at peak $L_{pk} \leqslant 3 \times 10^{43}$ erg s^{-1} (compared to $L_{pk} \sim 4 \times 10^{44}$ erg s^{-1} of AT 2018cow). It is thus unclear how representative is the PanSTARRS FBOT rate of AT 2018cow-like transients. Future observations and analysis will provide an answer to this question. In this work, we will not speculate any further on AT 2018cow-like transient rates.

4.3. Tidal Disruption by an Intermediate-mass Black Hole?

Alternatively, Perley et al. (2019) and Kuin et al. (2019) suggested that AT 2018cow could have been caused by the tidal disruption of a main-sequence star by an intermediate-mass black hole (IMBH) not coincident with the host-galaxy nucleus. For an IMBH of mass $M_\bullet$, the fallback time of the

mostly tightly bound debris following a TDE is given by (e.g., Stone & Metzger 2016; Chen & Shen 2018)

$$t_{fb} \approx 4.1 \text{ days} \left(\frac{M_\bullet}{10^4 M_\odot}\right)^{1/2} \left(\frac{M_\star}{M_\odot}\right)^{1/5}, \quad (28)$$

where we have assumed a mass–radius relationship $M_\star \propto R_\star^{0.8}$ appropriate for the lower main sequence. t_{fb} is similar to the observed rise time of AT 2018cow. Therefore, if circularization of the debris is relatively efficient, such that the light curve rises on the initial fallback time, then an IMBH mass of $10^4 M_\odot$ could explain the short rise time of the emission. We note however that the circularization timescale of the TDE debris is a highly debated point in the literature (see, e.g., Chen & Shen 2018, who claim the circularization process could take years). Efficient circularization could be particularly problematic for such a low-mass black hole, as the angle through which the stream precesses due to general relativistic effects is extremely small (unless the pericenter of the tidally disrupted star was well within the tidal radius, which is unlikely).

One complication of this scenario is that the IMBH would be accreting at a rate exceeding its Eddington luminosity $L_{Edd} \approx 10^{42} M_{\bullet,4}$ erg s^{-1} by a large factor $\gtrsim 10$–100 at early times (Figure 9). However, recent radiation MHD simulations of super-Eddington flows by Jiang et al. (2014) find that radiative efficiencies of ∼5% (similar to thin disks) are possible for flows accreting up to $22\dot{M}_{Edd}$, in the range relevant here. Sądowski & Narayan (2016) find a similar result for the kinetic luminosities from the disk. If coming from the inner disk, the relevant radiation temperature would be close to that of the disk photosphere at the ISCO radius,

$$kT_{eff} \approx 0.11 \text{ keV} \left(\frac{\dot{M}}{\dot{M}_{Edd}} \frac{0.1}{\eta}\right)^{1/4} \left(\frac{M_\bullet}{10^4 M_\odot}\right)^{-1/4}. \quad (29)$$

Although this is softer than the required emission of the central X-ray source powering AT 2018cow, an additional process like inverse-Compton-scattering of soft photons from the disk by the corona electrons could create the necessary high-energy tail (as described in Section 3.3.3).

Perhaps a larger problem with the IMBH scenario is the origin of the dense external CSM responsible for the self-absorbed radio emission (Figure 13), which must then be present prior to the tidal disruption. Interpreted as a wind of

velocity $v_w = 10^4 \, \mathrm{km \, s^{-1}}$, characteristic of AGN outflows, one requires a mass-loss rate of $\sim 10^{-2}$–$10^{-3} \, M_\odot \, \mathrm{yr^{-1}}$, in excess of the Eddington accretion rate of $\dot{M}_{\mathrm{Edd}} \approx L_{\mathrm{Edd}}/0.1c^2 \approx 10^{-4} M_\odot \, \mathrm{yr^{-1}}$, for a $10^4 \, M_\odot$ BH. Alternatively, if the CSM represents an accretion flow onto the IMBH, the required accretion rate on radial scales $r \sim 3 \times 10^{15}$ cm achieved by the forward shock on timescales of weeks would be

$$\dot{M} \sim \frac{M_{\mathrm{enc}}}{t_{\mathrm{ff}}} \sim 3 \times 10^{-4} M_\odot \, \mathrm{yr^{-1}}, \qquad (30)$$

where $M_{\mathrm{enc}} \sim 3 \times 10^{-6} \, M_\odot$ is the effective mass at radius r for $A \sim 30 A_\star$ (as needed to explain the radio observations) and $t_{\mathrm{ff}} \sim (r^3/GM_\bullet)^{1/2} \approx 2 \times 10^7$ s is the freefall time for $M_\bullet = 10^4 \, M_\odot$. Therefore, unless the IMBH were already embedded in a gas-rich AGN-like environment prior to the tidal disruption event, it is challenging to explain the inferred presence of the external CSM.

4.4. Embedded Equatorial CSM Shock

Although we disfavor an external CSM shock as the origin of the observed X-ray emission from AT 2018cow (Section 3.3.1), the central source could be powered by a deeply embedded, internal shock (e.g., Andrews & Smith 2018). If the CSM were concentrated in an equatorial ring or sheet, this shock would be localized to the dense equatorial region (e.g., the central X-ray source would in fact be an X-ray ring; Figure 12, left panel). One way to explain the steeply decaying luminosity of AT 2018cow, $L_e \propto t^{-\alpha}$ with $\alpha \approx 2$–2.5, would be if the shock were decelerating. In this class of models, the torus of dense material existed before the AT 2018cow event. However, the very short rise time of AT 2018cow is directly related to its fast polar ejecta, and it is thus an intrinsic property of AT 2018cow, independent of the denser equatorial ring.

Consider the CSM to have a radial density profile $\rho \propto r^{-\gamma}$. If the shock is radiative, then its self-similar deceleration evolution is momentum conserving, and so, for a disk of vertical scale-height H with a constant aspect ratio $H/r \sim$ constant, we have $\rho v_{\mathrm{sh}} R_{\mathrm{sh}}^3 \propto R_{\mathrm{sh}}^{4-\gamma}/t = $ constant, i.e., $R_{\mathrm{sh}} \propto t^{1/(4-\gamma)}$ and $v_{\mathrm{sh}} \sim R_{\mathrm{sh}}/t \propto t^{(\gamma-3)/(4-\gamma)}$. Therefore, the shock luminosity would evolve as

$$L_e = L_{\mathrm{sh}} \propto v_{\mathrm{sh}}^3 R_{\mathrm{sh}}^2 \rho \propto t^{(2\gamma-7)/(4-\gamma)}. \qquad (31)$$

For a constant CSM density profile $\gamma = 0$, we find $L_{\mathrm{sh}} \propto t^{-7/4}$, similar to the luminosity decay of AT 2018cow.

Not addressed in this scenario is the relatively soft intrinsic spectrum of the X-rays escaping from the shock. Given the high shock velocities, one would expect the shock-heated gas to emit through the free–free process, which for a single-temperature plasma predicts $F_\nu \propto \nu^0$ at frequencies $\nu \ll kT_{\mathrm{sh}}$, where T_{sh} is the post-shock temperature, flatter than that observed for AT 2018cow. However, due to the aspherical shape of the shock front and various hydrodynamical instabilities that radiative shocks are susceptible to, the post-shock gas cannot be characterized by a single temperature (e.g., Steinberg & Metzger 2018). As the velocity of the shock decreases with time, the temperature of the post-shock gas will also decrease. This would result in a greater fraction of the shock power emerging at UV/soft X-ray frequencies, which are more easily absorbed by the ejecta, and thus could contribute to the observed rapid late-time decay in the X-ray luminosity $L_x \propto t^{-4}$. Future theoretical work is required to assess the X-ray emission emerging from

shocks propagating into aspherical environments, as similar physics is at work in a variety of astrophysical transients (e.g., SNe IIn, luminous red novae, and classical novae; e.g., Andrews & Smith 2018; Metzger & Pejcha 2017).

5. Conclusions

In this first extensive radio-to-γ-ray study of an FBOT, we uncovered a new class of astronomical transients that are powered by a central engine and are characterized by luminous and long-lived radio and X-ray emission. Events similar to AT 2018cow can be detected with current X-ray/radio facilities in the local universe at $z \leqslant 0.2$.

Our study highlights the importance of follow-up observations across the spectrum, including the hard X-ray range at $E > 10 \, \mathrm{keV}$, which are rarely performed. This monitoring campaign led to the discovery of a new spectral component of hard X-ray emission at $E \geqslant 10 \, \mathrm{keV}$, with unprecedented properties among astronomical transients—but reminiscent of "Compton humps" and Fe K-shell emission observed in AGNs and XRBs—which would have been entirely missed in the absence of NuSTAR/INTEGRAL observations. At the same time, observations of AT 2018cow on the low-frequency end of the spectrum at $\nu < 100 \, \mathrm{GHz}$ revealed a non-relativistic blast wave propagating into a relatively dense environment, with radio luminosity similar to the brightest radio SNe.

The X-ray and UV/optical emission of AT 2018cow instead display stark differences with respect to those of normal SNe, and point toward a small amount of asymmetrically distributed H-/He-rich ejecta. Asymmetry is a key property of AT 2018cow. The need for a departure from spherical symmetry independently arises from the peculiar velocity gradient of the optically emitting material, from the redshifted centroids of the optical/NIR emission-line profiles, and from the X-ray temporal and spectral properties of the broadband X-ray emission. Our analysis furthermore identified two distinct phases of evolution of AT 2018cow, marked by the simultaneous change of its optical and X-ray properties around ~ 20 days.

The observed properties of AT 2018cow rule out traditional models where the transient emission is powered by the radioactive decay of ^{56}Ni and are not consistent with interaction-powered models, where the entire spectrum originates from the external interaction of the blast wave with the environment (which was suggested by Rivera Sandoval et al. 2018). Our detailed modeling shows that the phenomenology of AT 2018cow requires the presence of a central source of high-energy radiation shining through low-mass ejecta with pronounced equatorial–polar asymmetry. The "central engine" might be either in the form of a compact object (like a millisecond magnetar or black hole), or a deeply embedded internal shock. We find that low-mass H-rich stars that have been predicted to end their lives as electron-capture SNe, or blue supergiant stars that fail to explode, are viable progenitor systems of AT 2018cow and are consistent with the location of AT 2018cow within a star-forming dwarf galaxy. The tidal disruption of a star by an off-center IMBH suggested by Perley et al. (2019) and Kuin et al. (2019) is disfavored by the large environmental density that we infer.

Panchromatic studies of future FBOTs will clarify whether AT 2018cow is a representative member of its class and will reveal the connection (or lack thereof) of FBOTs to other classes of explosive transients, like GRBs or TDEs (the only two types of transients that are known to show persistent and

Margutti et al.

rapid X-ray variability so far). In this respect, it is interesting to mention that hints of hard X-ray excesses have been reported in long GRBs (Margutti et al. 2008; Moretti et al. 2008), which are central-engine-powered explosions, and in ultralong GRBs (Stratta et al. 2013; Bellm et al. 2014), for which the connection to blue supergiant progenitors has already been suggested (e.g., Quataert & Kasen 2012; Gendre et al. 2013; Nakauchi et al. 2013; Wu et al. 2013; Liu et al. 2018).

Facilities: Swift, XMM, NuSTAR, INTEGRAL, Odyssey, WIND (Konus), Fermi, Magellan:Baade (LDSS2 imaging spectrograph, Boller & Chivens spectrograph), Magellan:Clay (LDSS2 imaging spectrograph), SOAR, Keck:I, Keck:II, WIYN, CTIO:0.9m, UKIRT, MMT, VLA, VLBA.

Software: BOXFIT (Version 2; van Eerten et al. 2010, 2012), CASA (McMullin et al. 2007), CIAO (Fruscione et al. 2006), HEAsoft (Version 6.24), HOTPANTS (Becker 2015), *INTEGRAL* Off-line Scientific Analysis (OSA), IRAF (Tody 1986, 1993), pwkit (Williams et al. 2017), SNOoPY (http://sngroup.oapd.inaf.it/snoopy.html), XMM-Newton SAS (Version 17.0), XSPEC (Arnaud 1996).

Appendix

Data tables and logs of our observations of AT 2018cow (Tables 3–12).

Table 3
Log of NIR/Optical Spectroscopic Observations

UT date	MJD (days)	Phase (days)	Instrument/ Telescope	Wavelength Range (Å)	Resolution (Å)
2018 Jun 21	58290.1	+4.6	Goodman red cam/SOAR	3500–8980	5.2
2018 Jun 26	58295.1	+9.5	Goodman red cam/SOAR	3530–8930	3.0
2018 Jun 27	58296.1	+10.5	Goodman red cam/SOAR	3500–8980	5.2
2018 Jun 29	58298.2	+12.5	Goodman red cam/SOAR	3500–8980	5.0
2018 Jul 03	58302.3	+16.6	MMIRS/MMT	9800–23100	5–17
2018 Jul 09	58308.2	+22.4	LDSS3/*Magellan* (Clay)	3800–10000	8.0
2018 Jul 21	58320.1	+34.2	Goodman red cam./SOAR	3500–7050	4.4
2018 Aug 06	58336.0	+51.0	IMACS/*Magellan* (Baade)	3500–9000	5
2018 Aug 17	58347.7	+62.3	DEIMOS/Keck II	4500–8500	3.0
2018 Sep 10	58371.2	+85.8	LRIS/Keck I	3200–9000	6.0

Table 4
Swift-XRT Time-resolved Spectral Analysis

Start (days)	End (days)	$N_{\mathrm{H,int}}$ (10^{22} cm^{-2})	Γ	Absorbed Flux 0.3–10 keV (erg s^{-1} cm^{-2})	Unabsorbed Flux 0.3–10 keV (erg s^{-1} cm^{-2})
3	5	<0.0624	1.55 ± 0.053	$2.01^{+0.10}_{-0.095} \times 10^{-11}$	$2.13^{+0.11}_{-0.10} \times 10^{-11}$
5	7	<0.0586	1.63 ± 0.035	$1.65^{+0.052}_{-0.052} \times 10^{-11}$	$1.77^{+0.056}_{-0.056} \times 10^{-11}$
7	11	<0.0919	1.52 ± 0.050	$8.19^{+0.34}_{-0.38} \times 10^{-12}$	$8.69^{+0.36}_{-0.40} \times 10^{-12}$
11	13	<0.0538	1.46 ± 0.040	$9.87^{+0.40}_{-0.36} \times 10^{-12}$	$1.04^{+0.042}_{-0.038} \times 10^{-11}$
13	15	<0.157	1.56 ± 0.093	$5.64^{+0.54}_{-0.43} \times 10^{-12}$	$6.00^{+0.57}_{-0.46} \times 10^{-12}$
15	19	<0.0641	1.41 ± 0.039	$5.26^{+0.19}_{-0.18} \times 10^{-12}$	$5.52^{+0.20}_{-0.19} \times 10^{-12}$
19	21.5	<0.0758	1.41 ± 0.042	$8.47^{+0.33}_{-0.36} \times 10^{-12}$	$8.89^{+0.35}_{-0.38} \times 10^{-12}$
21.5	23	<0.127	1.49 ± 0.071	$4.07^{+0.29}_{-0.26} \times 10^{-12}$	$4.30^{+0.31}_{-0.27} \times 10^{-12}$
23	24.5	<0.240	1.36 ± 0.10	$4.84^{+0.54}_{-0.51} \times 10^{-12}$	$5.06^{+0.56}_{-0.53} \times 10^{-12}$
24.5	26	<0.167	1.47 ± 0.080	$4.17^{+0.38}_{-0.30} \times 10^{-12}$	$4.40^{+0.40}_{-0.32} \times 10^{-12}$
26	29	<0.193	1.36 ± 0.16	$2.73^{+0.48}_{-0.36} \times 10^{-12}$	$2.85^{+0.50}_{-0.38} \times 10^{-12}$
29	31	<0.224	1.50 ± 0.21	$1.96^{+0.42}_{-0.36} \times 10^{-12}$	$2.07^{+0.44}_{-0.38} \times 10^{-12}$
31	35	<0.157	1.56 ± 0.071	$2.32^{+0.17}_{-0.16} \times 10^{-12}$	$2.47^{+0.18}_{-0.17} \times 10^{-12}$
35	40	<0.298	1.47 ± 0.13	$1.53^{+0.22}_{-0.16} \times 10^{-12}$	$1.61^{+0.23}_{-0.17} \times 10^{-12}$
40	50	<0.145	1.54 ± 0.11	$9.46^{+1.0}_{-0.89} \times 10^{-13}$	$1.00^{+0.11}_{-0.094} \times 10^{-12}$
50	58	<1.02	1.37 ± 0.23	$3.81^{+0.86}_{-0.70} \times 10^{-13}$	$3.99^{+0.90}_{-0.73} \times 10^{-13}$

Note. We model the 0.3–10 keV spectrum with an absorbed simple power-law spectrum (`ztbabs*tbabs*pow` within Xspec). The galactic column density of neutral hydrogen in the direction of AT 2018cow is $N_{\mathrm{H,MW}} = 0.05 \times 10^{22}$ cm^{-2} (Kalberla et al. 2005).

Table 5
Log of *INTEGRAL* Observations

Orbit	Start time (UT)	Stop time (UT)	Midtime (MJD) (days)	Phase (days)	On-time (ks)
1968	2018 Jun 22 18:39:55	2018 Jun 24 22:21:07	58292.9	7.4	164
1969	2018 Jun 25 10:33:59	2018 Jun 27 14:10:12	58295.5	10.1	169
1970	2018 Jun 28 01:32:03	2018 Jun 30 05:00:38	58298.1	12.7	176
1971	2018 Jun 30 18:05:43	2018 Jul 02 17:38:49	58300.7	15.3	156
1972	2018 Jul 03 10:08:38	2018 Jul 04 04:50:23	58302.8	17.4	59
1973	2018 Jul 06 00:56:16	2018 Jul 08 04:58:20	58306.1	20.7	175

Table 6
Log of *NuSTAR* Observations

ID	Start time (UT)	Stop time (UT)	Midtime (MJD) (days)	Phase (days)	Exposure Time (ks)
90401327002	2018 Jun 23 17:31:09	2018 Jun 24 11:01:09	58293.1	7.7	27.9
90401327004	2018 Jul 02 14:00:12	2018 Jul 03 07:30:00	58301.9	16.5	30.0
90401327006	2018 Jul 14 06:20:09	2018 Jul 14 23:35:00	58313.6	28.2	31.2
90401327008	2018 Jul 22 13:56:09	2018 Jul 23 09:06:09	58321.8	36.5	13.9

Table 7
Best-fitting Parameters of the Broadband X-Ray Spectra of AT 2018cow Obtained Combining *Swift*-XRT, *XMM*, *NuSTAR*, and *INTEGRAL* Observations

Epoch	Phase (days)	$N_{\rm H,int}$ (10^{22} cm^{-2})	Γ	$N_{\rm H,hard}$ (10^{22} cm^{-2})	$E_{\rm cutoff}$ (keV)	$F_{\rm x,hard}$ (20–200 keV) (10^{-11} erg cm^{-2} s^{-1})	Unabsorbed $F_{\rm x,soft}$ (0.3–10 keV) (10^{-11} erg cm^{-2} s^{-1})
1[a]	7.7	<0.06	1.62 ± 0.03	2100^{+150}_{-350}	72^{+25}_{-20}	$2.29^{+0.72}_{-0.69}$	$1.04^{+0.09}_{-0.04}$
2[b]	10.1	<0.07	1.49 ± 0.05	2100	31^{+21}_{-14}	$3.00^{+0.94}_{-1.60}$	$1.04^{+0.07}_{-0.07}$
3[c]	12.7	<0.11	1.51 ± 0.06	2100	31	$2.68^{+0.84}_{-1.20}$	$0.97^{+0.03}_{-0.06}$
4[d]	16.5	<0.04	1.43 ± 0.08	2100	31	<0.94	$0.79^{+0.04}_{-0.04}$
5[e]	28.2	<0.39	1.58 ± 0.04	2100	31	<0.40	$0.34^{+0.05}_{-0.05}$
6[f]	36.5	<0.03	1.67 ± 0.02	2100	31	<1.11	$0.21^{+0.01}_{-0.03}$

Notes. We model the data with the combination of an absorbed power-law and cutoff power-law model (`ztbabs*(tbabs1*pow+tbabs2*cutoffpl)`) within Xspec). The power law and cutoff power law are tied to have the same photon index Γ. We assume a galactic column density of neutral hydrogen $N_{\rm H,MW} = 0.05 \times 10^{22}$ cm^{-2} (Kalberla et al. 2005). Quantities without uncertainties have been frozen to the value reported. The absorbed cutoff power-law model is purely phenomenological.
[a] *Swift*-XRT data between $\delta t = 7.3$–8.0 days; *NuSTAR* ID 90401327002 ($\delta t = 6.8$–8.3 days); *INTEGRAL* orbit 1968 ($\delta t = 6.3$–8.5 days).
[b] *Swift*-XRT data between $\delta t = 9$–11.2 days; *INTEGRAL* orbit 1969 ($\delta t = 8.9$–11.2 days).
[c] *Swift*-XRT data between $\delta t = 11.6$–13.8 days; *INTEGRAL* orbit 1970 ($\delta t = 11.6$–13.8 days).
[d] *Swift*-XRT data between $\delta t = 16.1$–16.9 days; *NuSTAR* ID 90401327004 ($\delta t = 16.1$–16.9 days).
[e] *Swift*-XRT data between $\delta t = 27.8$–28.1 days; *NuSTAR* ID 90401327006 ($\delta t = 27.8$–28.5 days).
[f] *Swift*-XRT data between $\delta t = 36.1$–37.0 days; *XMM* ID 0822580401 ($\delta t = 36.6$–36.9 days); *NuSTAR* ID 90401327008 ($\delta t = 36.1$–36.9 days).

Table 8
Radio Flux-density Measurements with the VLA and VLBI

Start Date (UT)	Phase (days)	Frequency (GHz)	Bandwidth (GHz)	Flux Density (mJy)	Instrument
2018 Jul 08	21.6	22.3	0.3	5.85 ± 0.61	VLBI
2018 Sep 06	82.51	5.0	1.0	5.04 ± 0.04	VLA
2018 Sep 06	82.51	7.1	1.0	7.76 ± 0.09	VLA
2018 Sep 07	83.51	9.0	2.0	9.10 ± 0.30	VLA
2018 Sep 07	83.51	11.0	2.0	9.80 ± 0.40	VLA
2018 Sep 07	83.52	2.5	1.0	2.25 ± 0.11	VLA
2018 Sep 07	83.52	3.5	1.0	3.24 ± 0.06	VLA
2018 Sep 07	83.52	1.3	0.5	0.80 ± 0.26	VLA
2018 Sep 07	83.52	1.8	0.5	1.40 ± 0.13	VLA
2018 Sep 16	91.61	19.	2.0	8.62 ± 0.06	VLA
2018 Sep 16	91.61	21	2.0	7.52 ± 0.09	VLA
2018 Sep 16	91.61	23	2.0	6.81 ± 0.11	VLA
2018 Sep 16	91.61	25	2.0	6.10 ± 0.07	VLA
2018 Oct 27	132.56	1.3	⋯	1.85 ± 0.11	VLA
2018 Oct 27	132.56	1.8	⋯	2.65 ± 0.13	VLA
2018 Oct 27	132.56	2.5	⋯	3.20 ± 0.07	VLA
2018 Oct 27	132.56	3.5	⋯	3.78 ± 0.07	VLA
2018 Oct 27	132.56	5.0	⋯	4.87 ± 0.09	VLA
2018 Oct 27	132.56	7.1	⋯	4.75 ± 0.10	VLA
2018 Oct 27	132.56	9.0	⋯	4.03 ± 0.05	VLA
2018 Oct 27	132.56	11.0	⋯	3.26 ± 0.05	VLA
2018 Nov 13	150.22	31.1	⋯	0.481 ± 0.030	VLA
2018 Nov 13	150.21	35.0	⋯	0.387 ± 0.032	VLA
2018 Nov 13	150.21	20.1	⋯	0.847 ± 0.023	VLA
2018 Nov 13	150.21	24.0	⋯	0.690 ± 0.021	VLA
2018 Nov 13	150.21	13.5	⋯	1.52 ± 0.03	VLA
2018 Nov 13	150.21	16.6	⋯	1.16 ± 0.021	VLA

Note. For VLBI measurements, the listed uncertainties include systematics. For the VLA, we list statistical uncertainties only (systematic uncertainties are estimated to be at the level of ∼5%).

Table 9
Ground-based Optical Photometry (Vega Magnitudes): Observed Magnitudes

Phase (days)	V (mag)	B (mag)	R (mag)	I (mag)	Telescope
5.63	15.10 ± 0.04	14.90 ± 0.07	14.95 ± 0.05	15.05 ± 0.08	SMARTS+ANDICAM
6.66	15.30 ± 0.14	15.24 ± 0.04	15.21 ± 0.07	15.22 ± 0.16	SMARTS+ANDICAM
7.69	15.65 ± 0.05	15.50 ± 0.04	15.48 ± 0.12	15.37 ± 0.10	SMARTS+ANDICAM
8.68	15.72 ± 0.16	15.46 ± 0.14	15.54 ± 0.17	15.34 ± 0.17	SMARTS+ANDICAM
9.61	16.03 ± 0.05	15.99 ± 0.04	15.81 ± 0.08	15.67 ± 0.11	SMARTS+ANDICAM
11.63	16.27 ± 0.07	16.27 ± 0.06	16.18 ± 0.08	16.08 ± 0.10	SMARTS+ANDICAM
12.63	16.42 ± 0.06	16.30 ± 0.06	16.23 ± 0.07	16.24 ± 0.16	SMARTS+ANDICAM
14.61	16.47 ± 0.16	16.53 ± 0.21	16.45 ± 0.22	16.26 ± 0.30	SMARTS+ANDICAM
15.64	16.71 ± 0.05	16.67 ± 0.07	16.58 ± 0.05	16.49 ± 0.10	SMARTS+ANDICAM
17.62	⋯	17.03 ± 0.04	16.98 ± 0.06	16.75 ± 0.09	SMARTS+ANDICAM
19.63	17.09 ± 0.06	17.17 ± 0.05	17.10 ± 0.08	16.86 ± 0.08	SMARTS+ANDICAM
21.61	⋯	17.36 ± 0.05	17.25 ± 0.06	17.05 ± 0.09	SMARTS+ANDICAM
22.64	17.50 ± 0.06	17.56 ± 0.06	17.42 ± 0.08	17.13 ± 0.08	SMARTS+ANDICAM
23.65	17.63 ± 0.07	17.61 ± 0.09	17.46 ± 0.08	17.18 ± 0.09	SMARTS+ANDICAM
24.62	⋯	17.75 ± 0.07	17.61 ± 0.08	17.40 ± 0.10	SMARTS+ANDICAM
26.61	18.05 ± 0.08	18.07 ± 0.08	17.93 ± 0.08	17.48 ± 0.10	SMARTS+ANDICAM
34.61	18.47 ± 0.09	18.78 ± 0.13	18.62 ± 0.14	18.20 ± 0.14	SMARTS+ANDICAM
36.62	18.94 ± 0.14	18.94 ± 0.15	18.79 ± 0.20	18.20 ± 0.17	SMARTS+ANDICAM
37.59	19.06 ± 0.16	18.91 ± 0.19	18.88 ± 0.21	18.48 ± 0.22	SMARTS+ANDICAM
38.61	19.22 ± 0.12	19.01 ± 0.11	18.69 ± 0.10	18.51 ± 0.22	SMARTS+ANDICAM
44.61	19.32 ± 0.13	19.35 ± 0.18	19.31 ± 0.17	19.05 ± 0.40	SMARTS+ANDICAM
46.62	⋯	19.70 ± 0.21	19.20 ± 0.21	19.15 ± 0.31	SMARTS+ANDICAM
62.88	21.20 ± 0.07	20.97 ± 0.08	20.68 ± 0.06	20.34 ± 0.07	Keck II+DEIMOS
111.82	22.50 ± 0.30	22.01 ± 0.30	21.37 ± 0.30	21.19 ± 0.30	Keck I+LRIS

Table 10
Ground-based NIR Photometry (Vega Magnitudes): Observed Magnitudes

Phase (J) (days)	J[a] (mag)	Phase (H) (days)	H (mag)	Phase (K) (days)	K (mag)	Telescope
9.86	15.83 ± 0.06	9.86	15.54 ± 0.11	9.86	15.17 ± 0.22	WIYN
9.90	15.90 ± 0.04	9.91	15.24 ± 0.04	9.92	14.99 ± 0.05	UKIRT
13.83	16.27 ± 0.05	13.84	15.72 ± 0.04	13.84	15.50 ± 0.05	UKIRT
22.85	16.76 ± 0.10	22.86	15.75 ± 0.05	22.87	15.87 ± 0.08	UKIRT
26.82	17.51 ± 0.20	26.83	15.84 ± 0.05	26.85	15.76 ± 0.07	UKIRT
30.86	18.07 ± 0.37	30.88	16.11 ± 0.06	30.89	15.90 ± 0.07	UKIRT
35.82	18.24 ± 0.40	34.93	17.18 ± 0.14	35.84	15.98 ± 0.08	UKIRT
39.80	18.99 ± 0.87	35.83	15.81 ± 0.05	41.84	16.76 ± 0.12	UKIRT
41.82	18.52 ± 0.51	39.82	15.85 ± 0.05	⋯	⋯	UKIRT
⋯	⋯	41.83	17.13 ± 0.07	⋯	⋯	UKIRT
75.70	>20.06	75.70	>19.22	75.70	>19.03	MMT

Note.
[a] Host-galaxy-subtracted photometry.

Table 11
Swift-UVOT *v*-, *b*- and *u*-band Photometry: Observed Magnitudes

Phase (*v*) (days)	*v* (mag)	Phase (*b*) (days)	*b* (mag)	Phase (*u*) (days)	*u* (mag)
3.06	13.95 ± 0.05	3.06	13.96 ± 0.05	3.06	12.53 ± 0.05
3.79	14.15 ± 0.05	3.79	14.28 ± 0.07	3.78	12.92 ± 0.07
5.26	14.83 ± 0.11	3.79	14.25 ± 0.05	3.79	12.89 ± 0.05
5.26	14.73 ± 0.05	5.25	15.02 ± 0.08	5.25	13.42 ± 0.07
6.26	15.03 ± 0.12	5.25	14.96 ± 0.05	5.25	13.46 ± 0.05
6.26	15.03 ± 0.05	6.25	15.23 ± 0.09	6.25	13.71 ± 0.08
6.84	15.18 ± 0.13	6.25	15.23 ± 0.05	6.25	13.72 ± 0.05
6.84	15.19 ± 0.06	6.84	15.35 ± 0.09	6.84	13.88 ± 0.08
9.18	15.73 ± 0.06	6.84	15.37 ± 0.05	6.84	13.85 ± 0.05
10.18	15.87 ± 0.08	9.17	15.88 ± 0.05	6.64	13.83 ± 0.05
11.24	15.96 ± 0.07	10.17	15.88 ± 0.06	9.17	14.49 ± 0.05
12.96	16.14 ± 0.07	11.24	16.09 ± 0.06	10.17	14.63 ± 0.06
14.29	16.14 ± 0.07	12.96	16.20 ± 0.05	11.10	14.80 ± 0.05
15.22	16.31 ± 0.08	14.29	16.30 ± 0.05	11.23	14.78 ± 0.05
16.36	16.51 ± 0.08	15.21	16.49 ± 0.06	11.23	14.82 ± 0.06
16.64	16.63 ± 0.09	16.35	16.64 ± 0.06	12.95	14.90 ± 0.05
18.35	16.78 ± 0.10	16.64	16.63 ± 0.06	14.28	15.07 ± 0.06
21.34	16.96 ± 0.11	18.34	16.88 ± 0.07	15.14	15.27 ± 0.05
21.73	16.87 ± 0.10	20.20	16.88 ± 0.07	15.21	15.29 ± 0.05
22.72	16.98 ± 0.10	21.33	17.11 ± 0.07	15.21	15.26 ± 0.06
23.79	17.02 ± 0.11	21.72	17.18 ± 0.07	16.35	15.49 ± 0.06
24.78	17.13 ± 0.12	22.72	17.19 ± 0.07	16.64	15.50 ± 0.06
25.72	17.21 ± 0.12	23.79	17.21 ± 0.07	18.34	15.71 ± 0.06
26.32	17.38 ± 0.14	24.78	17.36 ± 0.08	18.83	15.80 ± 0.05
27.01	17.30 ± 0.10	25.72	17.52 ± 0.08	20.20	15.86 ± 0.07
29.31	17.35 ± 0.15	26.32	17.53 ± 0.09	21.33	16.04 ± 0.07
31.09	17.34 ± 0.11	27.01	17.54 ± 0.07	21.72	16.05 ± 0.07
27.98	17.27 ± 0.09	29.31	17.68 ± 0.10	22.71	16.20 ± 0.07
33.50	17.25 ± 0.11	31.09	17.67 ± 0.08	23.79	16.35 ± 0.07
36.80	17.39 ± 0.11	27.97	17.55 ± 0.07	24.78	16.34 ± 0.07
34.81	17.57 ± 0.12	33.49	17.83 ± 0.08	25.71	16.54 ± 0.08
38.69	17.73 ± 0.11	36.80	17.80 ± 0.08	26.32	16.64 ± 0.08
41.72	17.57 ± 0.12	34.80	17.87 ± 0.08	27.01	16.64 ± 0.07
40.73	17.47 ± 0.13	38.82	18.02 ± 0.09	29.38	16.79 ± 0.08
39.93	17.52 ± 0.12	38.46	17.92 ± 0.10	31.09	16.89 ± 0.08
46.50	17.62 ± 0.12	41.71	18.12 ± 0.09	27.97	16.76 ± 0.07
45.44	17.69 ± 0.13	40.73	18.03 ± 0.10	33.49	17.14 ± 0.09
43.78	17.68 ± 0.13	39.92	18.27 ± 0.10	36.80	17.35 ± 0.09
47.96	17.80 ± 0.21	46.49	18.18 ± 0.10	39.19	17.47 ± 0.07
46.93	17.64 ± 0.13	45.43	18.04 ± 0.09	34.80	17.21 ± 0.08
60.14	17.72 ± 0.12	43.77	18.08 ± 0.09	40.73	17.44 ± 0.10
54.46	17.85 ± 0.27	47.96	18.18 ± 0.13	44.60	17.64 ± 0.08
52.27	17.90 ± 0.11	46.92	18.24 ± 0.11	41.71	17.45 ± 0.09
49.95	17.54 ± 0.10	54.46	18.24 ± 0.20	47.23	17.66 ± 0.08
57.71	17.67 ± 0.18	52.27	18.23 ± 0.08	49.95	17.76 ± 0.10
55.83	17.80 ± 0.13	49.95	18.06 ± 0.08	57.55	17.93 ± 0.16
…	…	60.14	18.44 ± 0.10	54.19	17.89 ± 0.08
…	…	57.71	18.48 ± 0.18	60.14	17.93 ± 0.11
…	…	55.82	18.19 ± 0.09	…	…

Table 12
Swift-UVOT *w*1-, *w*2-, and *m*2-band Photometry (Vega Magnitudes): Observed Magnitudes

Phase (*w*1) (days)	*w*1 (mag)	Phase (*w*2) (days)	*w*2 (mag)	Phase (*m*2) (days)	*m*2 (mag)
3.06	11.84 ± 0.06	3.06	11.55 ± 0.07	3.07	11.68 ± 0.06
3.78	12.07 ± 0.06	3.79	11.82 ± 0.09	3.79	11.94 ± 0.06
5.25	12.77 ± 0.09	3.79	11.85 ± 0.07	5.05	12.63 ± 0.06
6.25	12.98 ± 0.09	5.06	12.47 ± 0.07	5.26	12.63 ± 0.07
6.84	13.33 ± 0.10	5.26	12.60 ± 0.09	6.26	12.95 ± 0.06
6.12	12.95 ± 0.06	5.26	12.59 ± 0.07	6.85	13.34 ± 0.06
6.12	12.95 ± 0.06	6.26	12.96 ± 0.10	9.18	14.03 ± 0.06
9.17	14.00 ± 0.06	6.65	12.98 ± 0.07	9.16	13.81 ± 0.06
10.11	14.06 ± 0.06	8.37	13.45 ± 0.07	10.18	14.00 ± 0.06
10.17	14.05 ± 0.06	9.17	14.08 ± 0.07	11.24	14.27 ± 0.06
11.23	14.35 ± 0.06	8.23	13.45 ± 0.07	12.75	14.51 ± 0.07
12.36	14.45 ± 0.13	9.11	13.85 ± 0.07	12.95	14.61 ± 0.07
12.37	14.46 ± 0.06	10.17	14.07 ± 0.07	12.96	14.60 ± 0.06
12.95	14.52 ± 0.06	11.24	14.42 ± 0.07	14.29	14.83 ± 0.07
14.08	14.73 ± 0.06	12.09	14.48 ± 0.08	15.22	15.03 ± 0.07
14.28	14.73 ± 0.06	12.11	14.59 ± 0.08	16.36	15.33 ± 0.07
14.28	14.79 ± 0.06	12.36	14.47 ± 0.08	16.94	15.43 ± 0.07
15.21	14.93 ± 0.07	12.36	14.44 ± 0.14	16.64	15.32 ± 0.07
16.35	15.25 ± 0.07	12.77	14.50 ± 0.08	18.35	15.72 ± 0.08
16.63	15.32 ± 0.07	12.96	14.58 ± 0.07	20.82	15.88 ± 0.09
17.77	15.48 ± 0.06	14.29	14.83 ± 0.07	21.34	16.11 ± 0.09
18.34	15.59 ± 0.07	15.16	15.09 ± 0.08	21.73	16.06 ± 0.08
20.20	15.68 ± 0.07	15.21	15.05 ± 0.07	22.72	16.17 ± 0.08
21.33	15.90 ± 0.08	16.21	15.28 ± 0.08	23.79	16.25 ± 0.09
21.72	16.00 ± 0.08	16.22	15.32 ± 0.10	24.78	16.36 ± 0.10
22.25	15.99 ± 0.08	16.35	15.32 ± 0.08	25.28	16.62 ± 0.10
22.32	16.05 ± 0.08	16.36	15.38 ± 0.08	25.72	16.61 ± 0.10
22.71	16.08 ± 0.08	16.96	15.49 ± 0.09	26.32	16.70 ± 0.10
23.79	16.03 ± 0.08	16.64	15.42 ± 0.08	27.02	16.68 ± 0.09
24.77	16.21 ± 0.08	17.82	15.77 ± 0.10	29.32	17.06 ± 0.14
25.79	16.54 ± 0.07	18.34	15.78 ± 0.08	31.10	17.12 ± 0.10
27.01	16.64 ± 0.08	18.84	15.79 ± 0.09	27.98	16.72 ± 0.08
30.22	16.80 ± 0.11	19.76	15.80 ± 0.08	34.82	17.29 ± 0.10
29.38	16.76 ± 0.09	19.77	15.82 ± 0.09	33.50	17.14 ± 0.10
31.08	16.90 ± 0.09	20.20	15.82 ± 0.08	38.82	17.46 ± 0.12
27.97	16.63 ± 0.08	20.84	16.03 ± 0.09	38.46	17.30 ± 0.13
34.16	17.11 ± 0.09	21.34	16.02 ± 0.08	36.81	17.22 ± 0.11
34.15	17.14 ± 0.07	21.72	16.13 ± 0.08	41.72	17.54 ± 0.12
33.48	16.98 ± 0.09	22.30	16.21 ± 0.09	40.73	17.71 ± 0.14
38.46	17.15 ± 0.12	23.37	16.25 ± 0.09	39.93	17.69 ± 0.12
36.79	17.15 ± 0.10	22.72	16.32 ± 0.08	45.44	17.72 ± 0.13
34.80	17.06 ± 0.09	23.79	16.26 ± 0.08	43.78	17.74 ± 0.12
40.73	17.44 ± 0.12	24.78	16.46 ± 0.09	47.96	17.69 ± 0.17
39.92	17.39 ± 0.11	26.02	16.73 ± 0.08	46.93	17.70 ± 0.12
38.82	17.20 ± 0.10	27.01	16.78 ± 0.08	46.50	17.59 ± 0.12
43.77	17.51 ± 0.11	29.31	16.92 ± 0.10	54.46	17.92 ± 0.21
42.80	17.60 ± 0.25	31.09	17.00 ± 0.09	52.28	17.88 ± 0.11
41.71	17.45 ± 0.11	27.97	16.73 ± 0.08	49.95	17.62 ± 0.12
47.22	17.73 ± 0.09	33.49	17.17 ± 0.09	60.14	17.98 ± 0.11
45.43	17.43 ± 0.11	38.69	17.39 ± 0.09	57.71	18.02 ± 0.16
49.94	17.66 ± 0.10	36.80	17.28 ± 0.09	55.83	18.04 ± 0.13
55.42	17.89 ± 0.11	34.81	17.23 ± 0.09	⋯	⋯
55.82	17.82 ± 0.12	39.92	17.41 ± 0.10	⋯	⋯
58.84	17.95 ± 0.10	43.78	17.58 ± 0.10	⋯	⋯
⋯	⋯	41.71	17.48 ± 0.10	⋯	⋯
⋯	⋯	40.73	17.44 ± 0.10	⋯	⋯
⋯	⋯	46.76	17.69 ± 0.09	⋯	⋯
⋯	⋯	45.43	17.58 ± 0.10	⋯	⋯
⋯	⋯	49.95	17.73 ± 0.09	⋯	⋯
⋯	⋯	47.96	17.62 ± 0.13	⋯	⋯
⋯	⋯	55.82	17.86 ± 0.11	⋯	⋯

Table 12
(Continued)

Phase (w1) (days)	w1 (mag)	Phase (w2) (days)	w2 (mag)	Phase (m2) (days)	m2 (mag)
…	…	54.46	17.68 ± 0.16	…	…
…	…	52.27	17.81 ± 0.09	…	…
…	…	60.14	18.00 ± 0.10	…	…
…	…	57.71	18.11 ± 0.15	…	…

ORCID iDs

R. Margutti ⓘ https://orcid.org/0000-0003-4768-7586
B. D. Metzger ⓘ https://orcid.org/0000-0002-4670-7509
I. Vurm ⓘ https://orcid.org/0000-0003-1336-4746
B. W. Grefenstette ⓘ https://orcid.org/0000-0002-1984-2932
V. Savchenko ⓘ https://orcid.org/0000-0001-6353-0808
J. F. Steiner ⓘ https://orcid.org/0000-0002-5872-6061
G. Migliori ⓘ https://orcid.org/0000-0003-0216-8053
D. Milisavljevic ⓘ https://orcid.org/0000-0002-0763-3885
K. D. Alexander ⓘ https://orcid.org/0000-0002-8297-2473
M. Bietenholz ⓘ https://orcid.org/0000-0002-0592-4152
P. K. Blanchard ⓘ https://orcid.org/0000-0003-0526-2248
E. Bozzo ⓘ https://orcid.org/0000-0002-7504-7423
I. V. Chilingarian ⓘ https://orcid.org/0000-0002-7924-3253
C. Ferrigno ⓘ https://orcid.org/0000-0003-1429-1059
C. Guidorzi ⓘ https://orcid.org/0000-0001-6869-0835
K. Hurley ⓘ https://orcid.org/0000-0003-3315-1975
S. Mereghetti ⓘ https://orcid.org/0000-0003-3259-7801
M. Nicholl ⓘ https://orcid.org/0000-0002-2555-3192
D. Patnaude ⓘ https://orcid.org/0000-0002-7507-8115
E. Berger ⓘ https://orcid.org/0000-0002-9392-9681
E. R. Coughlin ⓘ https://orcid.org/0000-0003-3765-6401
D. D. Frederiks ⓘ https://orcid.org/0000-0002-1153-6340
T. Laskar ⓘ https://orcid.org/0000-0003-1792-2338
D. S. Svinkin ⓘ https://orcid.org/0000-0002-2208-2196
A. MacFadyen ⓘ https://orcid.org/0000-0002-0106-9013

References

Alexander, K. D., Berger, E., Guillochon, J., Zauderer, B. A., & Williams, P. K. G. 2016, ApJL, 819, L25
An, T. 2018, ATel, 12067
Andrews, J. E., & Smith, N. 2018, MNRAS, 477, 74
Andrews, J. E., Sugerman, B. E. K., Clayton, G. C., et al. 2011, ApJ, 731, 47
Arcavi, I., Gal-Yam, A., Cenko, S. B., et al. 2012, ApJL, 756, L30
Arcavi, I., Gal-Yam, A., Yaron, O., et al. 2011, ApJL, 742, L18
Arcavi, I., Wolf, W. M., Howell, D. A., et al. 2016, ApJ, 819, 35
Arnaud, K. A. 1996, in ASP Conf. Ser. 101, Astronomical Data Analysis Software and Systems V, ed. G. H. Jacoby & J. Barnes (San Francisco, CA: ASP), 17
Arnett, W. D. 1982, ApJ, 253, 785
Asplund, M., Grevesse, N., Sauval, A. J., & Scott, P. 2009, ARA&A, 47, 481
Balberg, S., & Loeb, A. 2011, MNRAS, 414, 1715
Band, D., Matteson, J., Ford, L., et al. 1993, ApJ, 413, 281
Becker, A. 2015, HOTPANTS: High Order Transform of PSF ANd Template Subtraction, Astrophysics Source Code Library, ascl:1504.004
Bellm, E. C., Barrière, N. M., Bhalerao, V., et al. 2014, ApJL, 784, L19
Berger, E., Zauderer, A., Pooley, G. G., et al. 2012, ApJ, 748, 36
Bernardini, M. G., Margutti, R., Chincarini, G., Guidorzi, C., & Mao, J. 2011, A&A, 526, A27
Bersten, M. C., Benvenuto, O. G., Nomoto, K., et al. 2012, ApJ, 757, 31
Bietenholz, M., Margutti, R., Alexander, K., et al. 2018, ATel, 11900
Blondin, J. M., & Chevalier, R. A. 2017, ApJ, 845, 139
Botticella, M. T., Pastorello, A., Smartt, S. J., et al. 2009, MNRAS, 398, 1041

Breeveld, A. A., Landsman, W., Holland, S. T., et al. 2011, in AIP Conf. Ser. 1358, GAMMA RAY BURSTS 2010, ed. J. E. McEnery, J. L. Racusin, & N. Gehrels (Melville, NY: AIP), 373
Bright, J., Horesh, A., Fender, R., et al. 2018, ATel, 11774
Brown, P. J., Holland, S. T., Immler, S., et al. 2009, AJ, 137, 4517
Burrows, D. N., Hill, J. E., Nousek, J. A., et al. 2005, SSRv, 120, 165
Campana, S., Mangano, V., Blustin, A. J., et al. 2006, Natur, 442, 1008
Cannizzo, J. K., Lee, H. M., & Goodman, J. 1989, in Theory of Accretion Disks, ed. F. Meyer et al. (Dordrecht: Springer), 397
Casali, M., Adamson, A., Alves de Oliveira, C., et al. 2007, A&A, 467, 777
Cenko, S. B., Bloom, J. S., Kulkarni, S. R., et al. 2012a, MNRAS, 420, 2684
Cenko, S. B., Krimm, H. A., Horesh, A., et al. 2012b, ApJ, 753, 77
Chandra, P., & Frail, D. A. 2012, ApJ, 746, 156
Chen, J.-H., & Shen, R.-F. 2018, arXiv:1806.08093
Chevalier, R. A. 1998, ApJ, 499, 810
Chevalier, R. A., & Fransson, C. 2006, ApJ, 651, 381
Chevalier, R. A., & Irwin, C. M. 2011, ApJL, 729, L6
Chevalier, R. A., & Li, Z.-Y. 2000, ApJ, 536, 195
Chilingarian, I., Beletsky, Y., Moran, S., et al. 2015, PASP, 127, 406
Chincarini, G., Mao, J., Margutti, R., et al. 2010, MNRAS, 406, 2113
Chomiuk, L., Chornock, R., Soderberg, A. M., et al. 2011, ApJ, 743, 114
Chomiuk, L., Soderberg, A., Margutti, R., et al. 2012, ATel, 3931
Chonis, T. S., & Gaskell, C. M. 2008, AJ, 135, 264
Chornock, R., Berger, E., Gezari, S., et al. 2014, ApJ, 780, 44
Clemens, J. C., Crain, J. A., & Anderson, R. 2004, Proc. SPIE, 5492, 331
Cobb, B. E., Bloom, J. S., Perley, D. A., et al. 2010, ApJL, 718, L150
Coughlin, E. R., Quataert, E., & Ro, S. 2018, arXiv:1805.06456
Dauser, T., García, J., Parker, M. L., Fabian, A. C., & Wilms, J. 2014, MNRAS, 444, L100
de Ugarte Postigo, A., Bremer, M., Kann, D. A., et al. 2018a, ATel, 11749
de Ugarte Postigo, A., Bremer, M., Kann, D. A., et al. 2018b, ATel, 11749
Dexter, J., & Kasen, D. 2013, ApJ, 772, 30
Dobie, D., Ravi, V., Ho, A., Kasliwal, M., & Murphy, T. 2018a, ATel, 11795
Dobie, D., Ravi, V., Ho, A., Kasliwal, M., & Murphy, T. 2018b, ATel, 11818
Dobie, D., Ravi, V., Ho, A., Kasliwal, M., & Murphy, T. 2018c, ATel, 11862
Drout, M. R., Chornock, R., Soderberg, A. M., et al. 2014, ApJ, 794, 23
Drout, M. R., Soderberg, A. M., Gal-Yam, A., et al. 2011, ApJ, 741, 97
Drout, M. R., Soderberg, A. M., Mazzali, P. A., et al. 2013, ApJ, 774, 58
Dwek, E. 1983, ApJ, 274, 175
Dye, S., Lawrence, A., Read, M. A., et al. 2018, MNRAS, 473, 5113
Eftekhari, T., Berger, E., Zauderer, B. A., Margutti, R., & Alexander, K. D. 2018, ApJ, 854, 86
Faber, S. M., Phillips, A. C., Kibrick, R. I., et al. 2003, Proc. SPIE, 4841, 1657
Fernández, R., Quataert, E., Kashiyama, K., & Coughlin, E. R. 2018, MNRAS, 476, 2366
Foley, R. J., Chornock, R., Filippenko, A. V., et al. 2009, AJ, 138, 376
Fruscione, A., McDowell, J. C., Allen, G. E., et al. 2006, Proc. SPIE, 6270, 62701V
Gal-Yam, A. 2012, Sci, 337, 927
Gehrels, N., Chincarini, G., Giommi, P., et al. 2004, ApJ, 611, 1005
Gendre, B., Stratta, G., Atteia, J. L., et al. 2013, ApJ, 766, 30
Ginzburg, S., & Balberg, S. 2014, ApJ, 780, 18
Granot, J., Panaitescu, A., Kumar, P., & Woosley, S. E. 2002, ApJL, 570, L61
Granot, J., & Sari, R. 2002, ApJ, 568, 820
Guidorzi, C. 2015, A&C, 10, 54
Hamly, N. C., Collins, R. S., Cross, N. J. G., et al. 2008, MNRAS, 384, 637
Hamuy, M. 2003, ApJ, 582, 905
Ho, A. Y. Q., Phinney, E. S., Ravi, V., et al. 2019, ApJ, 871, 73
Horesh, A., Moldon, J., Beswick, R., et al. 2018, ATel, 11819
Horne, J. H., & Baliunas, S. L. 1986, ApJ, 302, 757
Hotokezaka, K., Kashiyama, K., & Murase, K. 2017, ApJ, 850, 18
Hubeny, I., Agol, E., Blaes, O., & Krolik, J. H. 2000, ApJ, 533, 710

Inserra, C., Smartt, S. J., Jerkstrand, A., et al. 2013, ApJ, 770, 128
Ioka, K., Kobayashi, S., & Zhang, B. 2005, ApJ, 631, 429
Jiang, Y.-F., Stone, J. M., & Davis, S. W. 2014, ApJ, 796, 106
Kalberla, P. M. W., Burton, W. B., Hartmann, D., et al. 2005, A&A, 440, 775
Kasen, D., & Bildsten, L. 2010, ApJ, 717, 245
Kasen, D., Metzger, B. D., & Bildsten, L. 2016, ApJ, 821, 36
Kashiyama, K., & Quataert, E. 2015, MNRAS, 451, 2656
Kasliwal, M. M., Kulkarni, S. R., Gal-Yam, A., et al. 2010, ApJL, 723, L98
Katz, B., Sapir, N., & Waxman, E. 2011, arXiv:1106.1898
Kiewe, M., Gal-Yam, A., Arcavi, I., et al. 2012, ApJ, 744, 10
Kleiser, I. K. W., & Kasen, D. 2014, MNRAS, 438, 318
Kuin, N. P. M., Wu, K., Oates, S., et al. 2019, MNRAS, in press (doi:10.1093/mnras/stz053)
Lebrun, F., Leray, J. P., Lavocat, P., et al. 2003, A&A, 411, L141
Leonard, D. C., Filippenko, A. V., Gates, E. L., et al. 2002, PASP, 114, 35
Liu, T., Song, C.-Y., Zhang, B., Gu, W.-M., & Heger, A. 2018, ApJ, 852, 20
Lomb, N. R. 1976, Ap&SS, 39, 447
Lovegrove, E., & Woosley, S. E. 2013, ApJ, 769, 109
Lunnan, R., Chornock, R., Berger, E., et al. 2013, ApJ, 771, 97
Margalit, B., & Metzger, B. D. 2016, MNRAS, 461, 1154
Margalit, B., Metzger, B. D., Thompson, T. A., Nicholl, M., & Sukhbold, T. 2018, MNRAS, 475, 2659
Margutti, R., Guidorzi, C., Chincarini, G., et al. 2010, MNRAS, 406, 2149
Margutti, R., Metzger, B. D., Chornock, R., et al. 2017, ApJ, 836, 25
Margutti, R., Milisavljevic, D., Soderberg, A. M., et al. 2014, ApJ, 780, 21
Margutti, R., Moretti, A., Pasotti, F., et al. 2008, A&A, 480, 677
Margutti, R., Soderberg, A. M., Wieringa, M. H., et al. 2013b, ApJ, 778, 18
Margutti, R., Zaninoni, E., Bernardini, M. G., et al. 2013a, MNRAS, 428, 729
McLeod, B., Fabricant, D., Nystrom, G., et al. 2012, PASP, 124, 1318
McMullin, J. P., Waters, B., Schiebel, D., Young, W., & Golap, K. 2007, in ASP Conf. Ser. 376, Astronomical Data Analysis Software and Systems XVI, ed. R. A. Shaw, F. Hill, & D. J. Bell (San Francisco, CA: ASP), 127
Meixner, M., Smee, S., Doering, R. L., et al. 2010, PASP, 122, 451
Metzger, B. D. 2017, LRR, 20, 3
Metzger, B. D., Beniamini, P., & Giannios, D. 2018, ApJ, 857, 95
Metzger, B. D., Giannios, D., Thompson, T. A., Bucciantini, N., & Quataert, E. 2011, MNRAS, 413, 2031
Metzger, B. D., & Pejcha, O. 2017, MNRAS, 471, 3200
Metzger, B. D., & Piro, A. L. 2014, MNRAS, 439, 3916
Miyaji, S., Nomoto, K., Yokoi, K., & Sugimoto, D. 1980, PASJ, 32, 303
Mizuta, A., & Ioka, K. 2013, ApJ, 777, 162
Modjaz, M., Liu, Y. Q., Bianco, F. B., & Graur, O. 2016, ApJ, 832, 108
Moretti, A., Margutti, R., Pasotti, F., et al. 2008, A&A, 478, 409
Moriya, T. J., Mazzali, P. A., Tominaga, N., et al. 2017, MNRAS, 466, 2085
Moriya, T. J., Tominaga, N., Langer, N., et al. 2014, A&A, 569, A57
Nadezhin, D. K. 1980, Ap&SS, 69, 115
Nahar, S. N., & Pradhan, A. K. 1997, ApJS, 111, 339
Nakar, E., & Piro, A. L. 2014, ApJ, 788, 193
Nakauchi, D., Kashiyama, K., Suwa, Y., & Nakamura, T. 2013, ApJ, 778, 67
Nava, L., Salvaterra, R., Ghirlanda, G., et al. 2012, MNRAS, 421, 1256
Nayana, A. J., & Chandra, P. 2018, ATel, 11950
Nayana, A. J., Chandra, P., Ho, A., et al. 2018, ATel, 11794
Nicholl, M., Berger, E., Smartt, S. J., et al. 2016, ApJ, 826, 39
Nicholl, M., Blanchard, P. K., Berger, E., et al. 2018, ApJL, 866, L24
Nicholl, M., Guillochon, J., & Berger, E. 2017, ApJ, 850, 55
Nomoto, K., Sparks, W. M., Fesen, R. A., et al. 1982, Natur, 299, 803
Norris, J. P., Bonnell, J. T., Kazanas, D., et al. 2005, ApJ, 627, 324
Ofek, E. O., Rabinak, I., Neill, J. D., et al. 2010, ApJ, 724, 1396
Oke, J. B., Cohen, J. G., Carr, M., et al. 1995, PASP, 107, 375
Palmer, D. M. 2009, ApJ, 695, 496
Pastorello, A., Hadjiyska, E., Rabinowitz, D., et al. 2015, MNRAS, 449, 1954
Perets, H. B., Gal-Yam, A., Mazzali, P. A., et al. 2010, Natur, 465, 322
Perley, D. A., Mazzali, P. A., Yan, L., et al. 2019, MNRAS, 484, 1031
Perna, R., Lazzati, D., & Cantiello, M. 2018, ApJ, 859, 48
Phinney, E. S. 1989, in IAU Symp. 136, The Center of the Galaxy, ed. M. Morris (Dordrecht: Kluwer Academic), 543
Piro, A. L. 2013, ApJL, 768, L14
Poznanski, D., Chornock, R., Nugent, P. E., et al. 2010, Sci, 327, 58
Prentice, S. J., Maguire, K., Smartt, S. J., et al. 2018, ApJL, 865, L3
Press, W., Teukolsky, S., Vetterling, W., & Flannery, B. 1992, Numerical Recipes in C (Cambridge: Cambridge Univ. Press)
Pursiainen, M., Childress, M., Smith, M., et al. 2018, MNRAS, 481, 894
Quataert, E., & Kasen, D. 2012, MNRAS, 419, L1
Quataert, E., Lecoanet, D., & Coughlin, E. R. 2018, MNRAS, submitted (arXiv:1811.12427)

Quimby, R. M., Kulkarni, S. R., Kasliwal, M. M., et al. 2011, Natur, 474, 487
Racusin, J. L., Liang, E. W., Burrows, D. N., et al. 2009, ApJ, 698, 43
Rees, M. J. 1988, Natur, 333, 523
Reeves, J. N., Porquet, D., & Turner, T. J. 2004, ApJ, 615, 150
Rest, A., Garnavich, P. M., Khatami, D., et al. 2018, NatAs, 2, 307
Risaliti, G., Harrison, F. A., Madsen, K. K., et al. 2013, Natur, 494, 449
Rivera Sandoval, L. E., Maccarone, T. J., Corsi, A., et al. 2018, MNRAS, 480, L146
Roming, P. W. A., Kennedy, T. E., Mason, K. O., et al. 2005, SSRv, 120, 95
Ross, N., & Dwarkadas, V. V. 2017, AJ, 153, 246
Roth, N., & Kasen, D. 2018, ApJ, 855, 54
Roth, N., Kasen, D., Guillochon, J., & Ramirez-Ruiz, E. 2016, ApJ, 827, 3
Ryan, G., van Eerten, H., MacFadyen, A., & Zhang, B.-B. 2015, ApJ, 799, 3
Rybicki, G. B., & Lightman, A. P. 1979, AstQ, 3, 199
Sądowski, A., & Narayan, R. 2015, MNRAS, 453, 3213
Sądowski, A., & Narayan, R. 2016, MNRAS, 456, 3929
Scargle, J. D. 1982, ApJ, 263, 835
Schlafly, E. F., & Finkbeiner, D. P. 2011, ApJ, 737, 103
Shen, K. J., Kasen, D., Weinberg, N. N., Bildsten, L., & Scannapieco, E. 2010, ApJ, 715, 767
Shivvers, I., Zheng, W. K., Mauerhan, J., et al. 2016, MNRAS, 461, 3057
Shussman, T., Waldman, R., & Nakar, E. 2016, arXiv:1610.05323
Sironi, L., Keshet, U., & Lemoine, M. 2015, SSRv, 191, 519
Skrutskie, M. F., Cutri, R. M., Stiening, R., et al. 2006, AJ, 131, 1163
Smartt, S. J., Clark, P., Smith, K. W., et al. 2018, ATel, 11727
Smith, I. A., Tanvir, N. R., & Perley, D. A. 2018a, ATel, 11781
Smith, N. 2014, ARA&A, 52, 487
Smith, P. S., Leonard, D. C., Bilinski, C., et al. 2018b, ATel, 11789
Soderberg, A. M., Kulkarni, S. R., Berger, E., et al. 2005, ApJ, 621, 908
Soderberg, A. M., Margutti, R., Zauderer, B. A., et al. 2012, ApJ, 752, 78
Spitkovsky, A. 2006, ApJL, 648, L51
Steinberg, E., & Metzger, B. D. 2018, MNRAS, 479, 687
Steiner, J. F., Narayan, R., McClintock, J. E., & Ebisawa, K. 2009, PASP, 121, 1279
Stone, N. C., & Metzger, B. D. 2016, MNRAS, 455, 859
Stratta, G., Gendre, B., Atteia, J. L., et al. 2013, ApJ, 779, 66
Strubbe, L. E., & Quataert, E. 2009, MNRAS, 400, 2070
Suwa, Y., Yoshida, T., Shibata, M., Umeda, H., & Takahashi, K. 2015, MNRAS, 454, 3073
Suzuki, A., & Maeda, K. 2017, MNRAS, 466, 2633
Tanaka, M., Tominaga, N., Morokuma, T., et al. 2016, ApJ, 819, 5
Taubenberger, S., Pastorello, A., Mazzali, P. A., et al. 2006, MNRAS, 371, 1459
Tauris, T. M., Langer, N., Moriya, T. J., et al. 2013, ApJL, 778, L23
Tauris, T. M., Langer, N., & Podsiadlowski, P. 2015, MNRAS, 451, 2123
Tchekhovskoy, A., & Giannios, D. 2015, MNRAS, 447, 327
Tody, D. 1986, Proc. SPIE, 627, 733
Tody, D. 1993, in ASP Conf. Ser. 52, Astronomical Data Analysis Software and Systems II, ed. R. J. Hanisch, R. J. V. Brissenden, & J. Barnes (San Francisco, CA: ASP), 173
Tomsick, J. A., Nowak, M. A., Parker, M., et al. 2014, ApJ, 780, 78
Ubertini, P., Lebrun, F., Di Cocco, G., et al. 2003, A&A, 411, L131
Valenti, S., Benetti, S., Cappellaro, E., et al. 2008, MNRAS, 383, 1485
Valenti, S., Pastorello, A., Cappellaro, E., et al. 2009, Natur, 459, 674
Valenti, S., Taubenberger, S., Pastorello, A., et al. 2012, ApJL, 749, L28
van Dokkum, P. G. 2001, PASP, 113, 1420
van Eerten, H., van der Horst, A., & MacFadyen, A. 2012, ApJ, 749, 44
van Eerten, H. J., Leventis, K., Meliani, Z., Wijers, R. A. M. J., & Keppens, R. 2010, MNRAS, 403, 300
Vinkó, J., Yuan, F., Quimby, R. M., et al. 2015, ApJ, 798, 12
Walton, D. J., Fürst, F., Harrison, F. A., et al. 2018b, MNRAS, 473, 4360
Walton, D. J., Fürst, F., Heida, M., et al. 2018a, ApJ, 856, 128
Weiler, K. W., Panagia, N., Montes, M. J., & Sramek, R. A. 2002, ARA&A, 40, 387
Whitesides, L., Lunnan, R., Kasliwal, M. M., et al. 2017, ApJ, 851, 107
Williams, P. K. G., Clavel, M., Newton, E., & Ryzhkov, D. 2017, pwkit: Astronomical utilities in Python, Astrophysics Source Code Library, ascl:1704.001
Willingale, R., Starling, R. L. C., Beardmore, A. P., Tanvir, N. R., & O'Brien, P. T. 2013, MNRAS, 431, 394
Winkler, C., Courvoisier, T. J.-L., di Cocco, G., et al. 2003, A&A, 411, L1
Wright, A. E., & Barlow, M. J. 1975, MNRAS, 170, 41
Wu, X.-F., Hou, S.-J., & Lei, W.-H. 2013, ApJL, 767, L36
York, D. G., Adelman, J., Anderson, J. E., Jr., et al. 2000, AJ, 120, 1579
Yu, Y.-W., Zhang, B., & Gao, H. 2013, ApJL, 776, L40
Zauderer, B. A., Berger, E., Margutti, R., et al. 2013, ApJ, 767, 152